Designing Flexible Thin-Film Architectures

A Numerical Opto-Electrical Simulation Study

Barbara Huijskes

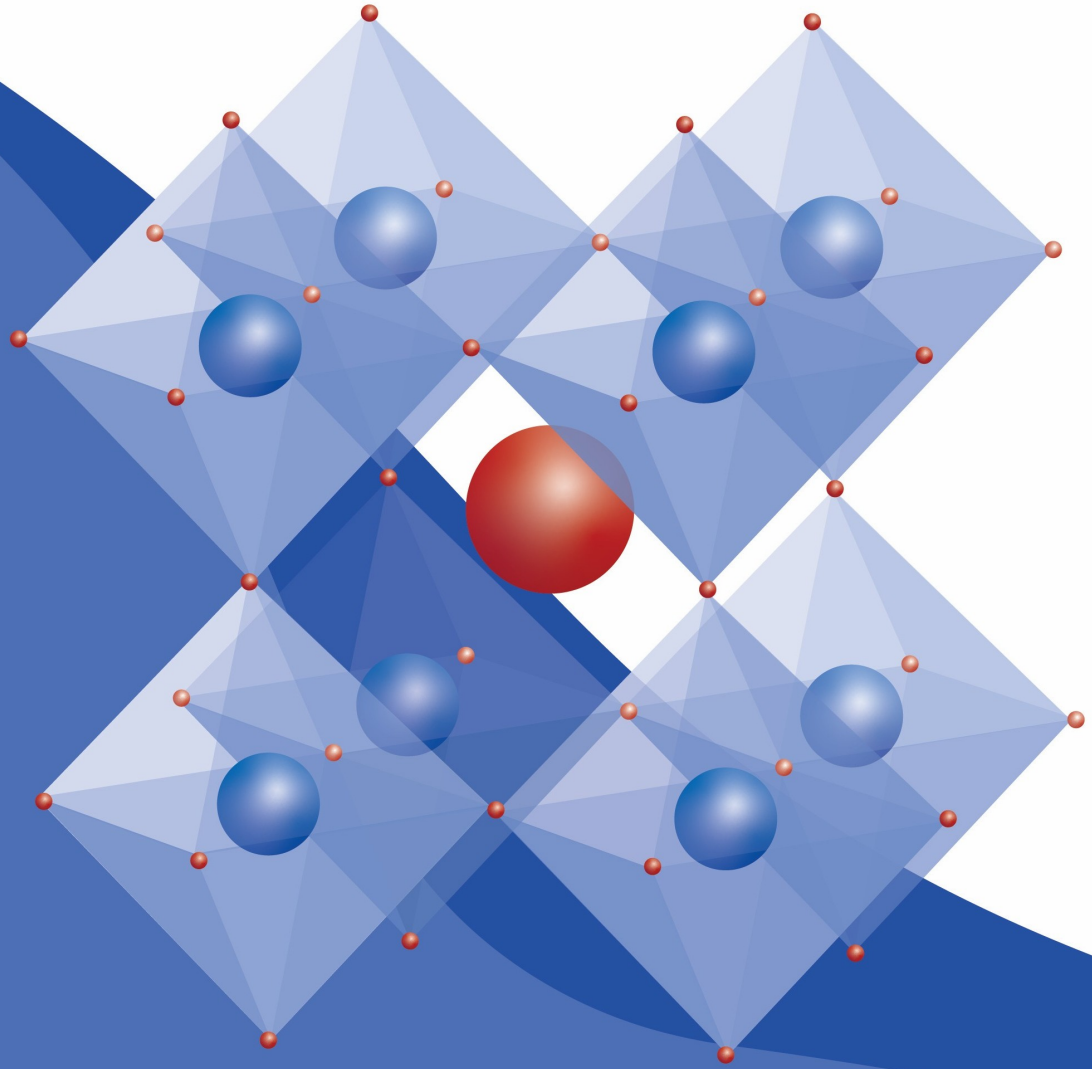

Delft University of Technology

TU Delft

Designing Flexible Thin-Film Architectures

A Numerical Opto-Electrical Simulation Study

by

Barbara Huijskes

to obtain the degree of
Master of Science
in Sustainable Energy Technology
at the Delft University of Technology, to be defended publicly on October 22, 2025 at 14:30

Student Number: 4809440

Thesis committee:
Prof. dr. Arno Smets, PVMD TU Delft, Supervisor
Dr. Paul Procel Moya, PVMD TU Delft, Daily Supervisor
Ir. Federica Saitta, PVMD TU Delft, Daily Supervisor
Dr.ir. Fabio Muñoz Muñoz, HVT group TU Delft, External Committee Member

TU Delft

Acknowledgment

Looking back on the past nine months, I realize how much I have learned and grown during this project. It has been a challenging yet deeply rewarding experience, filled with moments of exploration, problem-solving, and collaboration. I am truly grateful to everyone who supported and guided me throughout this journey.

I would like to thank Dr. Paul Procel for his enthusiasm, guidance, and the many insightful discussions we had. You always took the time to help me, no matter how busy you were, and your dedication and passion for research greatly inspired me. Your feedback and ideas played a key role in shaping this project and my understanding of the topic.

I also want to thank Federica Saitta for all your help, patience, and encouragement throughout this work. I've learned so much from you, and I really appreciated how you always made time to discuss ideas and provide guidance. You made me feel supported and never alone in this project, and I'm very thankful for that.

I'm also grateful to Prof. Dr. Arno Smets for giving me the opportunity to do this research within the PVMD group. It was a great environment to learn and develop both academically and personally.

Finally, I want to thank my family and friends for their endless support and encouragement. Your belief in me has meant the world, and I couldn't have done this without you.

Abstract

The global demand for sustainable and lightweight energy technologies continues to drive the development of advanced thin-film solar cells. Their potential for reduced material consumption, flexible integration, and scalable manufacturing makes them an essential component in the future of photovoltaics. However, despite decades of progress, thin-film silicon devices remain limited by material disorder and stability constraints, motivating the search for improved absorber and interface materials.

This research focuses on developing a predictive optical–electrical simulation framework for thin-film solar cells, capable of replicating real-world device behavior and guiding the design of next-generation architectures. The framework couples optical ray-tracing in GenPro4 with two-dimensional carrier-transport modeling in Sentaurus TCAD, allowing a realistic representation of textured interfaces, multilayer stacks, and lateral transport effects. The study begins with the calibration of single-junction amorphous silicon (a-Si:H) and nanocrystalline silicon (nc-Si:H) p–i–n cells against experimental data. These validated models are then combined into a tandem a-Si:H/nc-Si:H configuration, forming the optical and electrical foundation for further analysis.

Building on this baseline, the framework is extended to investigate flexible and hybrid device concepts. The transition from the rigid Asahi U-type glass substrate to a flexible configuration demonstrated the feasibility of lightweight devices, though efficiencies remained limited to approximately 10% due to defect-assisted recombination and weak near-infrared absorption. To overcome these limitations, perovskite absorbers were explored. Single-junction perovskite devices with various hole-transport layers (HTLs) achieved simulated efficiencies up to 22%, with NiO_x and nc-SiO_x providing superior thermal and chemical stability. A hybrid a-Si:H/perovskite tandem reached 16% efficiency, benefiting from the protective silicon top layer but constrained by its lower current. A fully perovskite–perovskite (PVK/PVK) tandem employing inorganic and nc-SiO_x HTLs achieved simulated efficiencies of 29%.

Finally, a detailed fill factor (FF) compensation study was conducted to quantify how current mismatch, recombination mechanisms, and electric-field distribution affect tandem performance. Five targeted case studies established design rules for stabilized operation through controlled mismatch, bandgap tuning, and optical optimization for a a-Si:H/nc-Si:H tandem solar cell.

Overall, this work delivers a unified simulation-based framework for the design and optimization of thin-film and hybrid tandem solar cells. The results provide fundamental insight into the performance limits of silicon and perovskite tandems and outline practical routes toward high-efficiency, lightweight, and manufacturable photovoltaic technologies.

AI Use Declaration

In the preparation of this thesis, I have made use of AI-based tools to support the writing and editing process. Specifically, tools such as ChatGPT were used for language polishing, paraphrasing suggestions, and structural feedback.

All scientific reasoning, results, and conclusions presented in this thesis are my own.

I confirm that the use of these tools complies with the guidelines of the Delft University of Technology and has not compromised the academic integrity of my work.

Nomenclature

Abbreviations

a-Si	Amorphous Silicon
AM1.5	Air Mass 1.5 (Standard Solar Spectrum)
ARC	Anti-Reflective Coating
AZO	Aluminum-doped Zinc Oxide
B2BT	Band-to-Band Tunneling
BCP	Bathocuproine
CBO	Conduction Band Offset
c-Si	Crystalline Silicon
DOS	Density of States
DT	Direct Tunneling
EFTE	Ethylene–Tetrafluoroethylene
EQE	External Quantum Efficiency
ETL	Electron Transport Layer
FF	Fill Factor
FEM	Finite Element Method
FTO	Fluorine-doped Tin Oxide
HTL	Hole Transport Layer
IQE	Internal Quantum Efficiency
IOH	Indium–Oxide–Hydrogen
ITO	Indium Tin Oxide
J–V	Current Density–Voltage Curve
J_{sc}	Short-Circuit Current Density
µc-Si	Microcrystalline Silicon
NBG	Narrow-Bandgap
nc-Si	Nanocrystalline Silicon
nc-SiO_x	Nanocrystalline Silicon Oxide
NLM	Nonlocal Mesh
PCE	Power Conversion Efficiency
PECVD	Plasma-Enhanced Chemical Vapor Deposition
PV	Photovoltaic
SAM	Self-Assembled Monolayer
SJ	Single Junction
SRH	Shockley–Read–Hall (Recombination)
SWE	Staebler–Wronski Effect
TAT	Trap-Assisted Tunneling
TCO	Transparent Conductive Oxide
TRJ	Tunnel Recombination Junction
V_{oc}	Open-Circuit Voltage
VBM	Valence Band Maximum
VBO	Valence Band Offset
WBG	Wide-Bandgap
WKB	Wentzel–Kramers–Brillouin Approximation

Symbols

Symbol	Description	Unit
A	Absorptance	%, unitless
c	Speed of light	3.00×10^8 m/s
D_n	Electron diffusion coefficient	cm^2/s
D_p	Hole diffusion coefficient	cm^2/s
Δx	Thickness of a spatial slice in the simulation grid	cm
E	Electric field	V/m
E_F	Fermi energy	eV
E_T	Trap energy level	eV
η	Power conversion efficiency	%
ε	Permittivity of material	F/m
G	Generation rate	cm^{-3}·s^{-1}
$G(x)$	Generation rate at position x	cm^{-3}·s^{-1}
$G(x, \lambda)$	Optical generation rate at x, λ	cm^{-3}·s^{-1}
h	Planck's constant	6.626×10^{-34} J·s
I	Light intensity	W/m^2
$I(\lambda)$	Spectral irradiance	W·m^{-2}·nm^{-1}
J	Current density	A/m^2, mA/cm^2
k	Boltzmann constant	1.381×10^{-23} J/K
λ	Wavelength	nm, µm
μ_n	Electron mobility	cm^2/Vs
μ_p	Hole mobility	cm^2/Vs
n	Electron concentration	cm^{-3}
n_1	Trap-related electron concentration	cm^{-3}
n_i	Intrinsic carrier concentration	cm^{-3}
N_A^-	Ionized acceptor density	cm^{-3}
N_D^+	Ionized donor density	cm^{-3}
p	Hole concentration	cm^{-3}
p_1	Trap-related hole concentration	cm^{-3}
P	Power	W
ϕ	Work function	eV
$\phi(\lambda)$	Incident photon flux	photons·cm^{-2}·s^{-1}·nm^{-1}
ϕ_n	Electron quasi-Fermi level	eV
ϕ_p	Hole quasi-Fermi level	eV
q	Elementary charge	1.602×10^{-19} C
R	Reflectance	%, unitless
R	Recombination rate	cm^{-3}·s^{-1}
R_{SRH}	Shockley–Read–Hall recombination rate	cm^{-3}·s^{-1}
ρ	Charge density	C/cm^3
s	Effective surface recombination velocity	cm/s
s_n	Surface recombination velocity (electrons)	cm/s
s_p	Surface recombination velocity (holes)	cm/s
t	Thickness of layer	nm, µm
T	Temperature	K
T	Transmittance	%, unitless
v_{th}	Thermal velocity	cm/s
V	Voltage	V
ψ	Electrostatic potential	V
σ_n	Electron capture cross-section	cm^2
σ_p	Hole capture cross-section	cm^2

Contents

1

Introduction

Over the past decades, thin-film silicon solar cells have played a pivotal role in advancing low-cost and large-area photovoltaic (PV) technologies. Their compatibility with scalable deposition techniques, mechanical flexibility, and low material consumption have made them an attractive alternative to conventional crystalline silicon (c-Si) modules. In particular, amorphous silicon (a-Si:H) and nanocrystalline silicon (nc-Si:H) thin films have been central to this development. When combined in a tandem configuration they offer extended spectral utilization through a wide-bandgap a-Si:H top cell and a narrow-bandgap nc-Si:H bottom cell, enabling efficiencies beyond the single-junction limit [14].

Despite these advantages, thin-film silicon technology has struggled to compete with emerging high-efficiency perovskite devices. The main bottlenecks are intrinsic to the disordered nature of the amorphous and nanocrystalline absorbers: a high density of localized defect states, strong light-induced degradation (LID), and limited carrier mobility [64]. These factors constrain both the open-circuit voltage and fill factor, ultimately capping stabilized efficiencies near 10–12% [28]. At the same time, the shift toward flexible and lightweight PV applications has renewed interest in thin-film platforms that can be fabricated on polymeric or metal foils through roll-to-roll processing. Such architectures demand optimized optical and electrical design to balance flexibility, stability, and efficiency.

To guide this development, predictive numerical modeling has become an essential research tool. Device simulations allow systematic exploration of material properties and interface effects that are difficult to isolate experimentally. Moreover, numerical approaches offer a clear advantage in terms of time and cost efficiency: complex parameter variations, degradation scenarios, or interface modifications can be examined without the need for labor-intensive fabrication and characterization cycles. For thin-film silicon and hybrid tandems, the combination of optical ray-tracing and electrical carrier-transport modeling provides deep insight into internal mechanisms such as field distribution, recombination, and tunneling across junctions. However, accurate modeling requires careful calibration against experimental data, particularly when describing trap-limited transport and nonlocal tunneling phenomena in disordered semiconductors.

The present work develops and validates a coupled optical–electrical simulation framework that bridges these challenges. The optical generation profiles are computed using the ray-tracing software GENPRO4, while electrical carrier dynamics are resolved in two dimensions using the Sentaurus TCAD platform. This two-dimensional capability allows the model to account for lateral transport effects, such as current spreading, partial shading, or nonuniform generation, which are critical in textured or patterned thin-film devices. The integrated framework thus enables realistic modeling of solar cells with complex geometries, multilayer stacks, and defect-mediated recombination. The goal is to reproduce experimentally observed device performance and to use the calibrated models as a predictive tool for designing next-generation flexible and hybrid tandem structures.

The study begins by calibrating single-junction a-Si:H and nc-Si:H devices and combining them into a monolithic a-Si:H/nc-Si:H tandem model that reproduces experimental current–voltage characteristics. Once validated, the framework is applied to investigate flexible thin-film tandems, highlighting

the trade-off between mechanical compatibility and performance, and motivating the transition toward perovskite-based absorbers. Subsequently, the model is extended to simulate single-junction and tandem perovskite cells with both organic and inorganic hole transport layers (HTLs), identifying NiO_x and nc-SiO_x as promising candidates for thermally stable, high-efficiency configurations. Finally, a detailed study on fill factor (FF) compensation explores how current mismatch, recombination dynamics, and internal field redistribution determine the efficiency maximum in both silicon- and perovskite-based tandems.

The objectives of this thesis are therefore threefold:

1. To establish and validate a physically accurate two-dimensional simulation framework for thin-film silicon solar cells, combining optical ray-tracing in GenPro4 with electrical carrier-transport modeling in Sentaurus TCAD.
2. To extend this framework toward flexible and perovskite-based hybrid tandem configurations, enabling evaluation of alternative absorber materials and interface designs.
3. To derive quantitative design rules for maximizing stabilized efficiency through controlled current mismatch and fill factor (FF) compensation, linking material quality and recombination dynamics to device-level performance.

The remainder of this thesis is organized as follows. Chapter 2 introduces the theoretical background of photovoltaic operation, outlining the key physical processes in semiconductor devices, with emphasis on transport, recombination, and light–matter interaction in disordered materials. Chapter 3 presents the numerical modeling methodology, describing the coupling between GenPro4 and Sentaurus TCAD, the construction of the two-dimensional device model, and the calibration strategy against experimental data. Chapter 4 details the validation of the calibrated a-Si:H and nc-Si:H single-junction models and their integration into a monolithic a-Si:H/nc-Si:H tandem configuration, demonstrating quantitative agreement with reference devices. Building upon this baseline, Chapter 5 explores the extension of the framework toward flexible thin-film tandems and perovskite-based architectures. The chapter compares the performance, stability, and interface characteristics of various absorber and HTL combinations, identifying pathways toward high-efficiency, low-weight photovoltaic modules. Subsequently, Chapter 6 investigates the phenomenon of fill factor compensation through a combination of controlled mismatch simulations and targeted parametric studies. It examines how field redistribution, recombination, and optical coupling affect the efficiency maximum in both silicon-based and perovskite-based tandems, leading to generalized design rules for stable operation. Finally, Chapter 7 summarizes the key findings of the thesis, highlighting the validated modeling framework, the insights gained from flexible and hybrid architectures, and the established FF compensation design principles. The chapter concludes with an outlook on future research directions, including extensions toward triple-junction and fully inorganic tandem devices.

2

Theoretical Background

The operation of a solar cell is governed by several fundamental processes: the generation of charge carriers, their transport through the device, recombination mechanisms, and the influence of interfaces and material properties on overall performance. This chapter provides the theoretical foundation for analyzing and modeling these processes across the material systems studied in this work.

It begins with an overview of key characterization techniques used to evaluate photovoltaic performance, namely the illuminated current–voltage (I–V) curve and the wavelength-resolved quantum efficiency (EQE and IQE). These measurements are then connected to the underlying semiconductor physics through the drift–diffusion model, which describes carrier transport, generation, and recombination in the device. Furthermore, attention is given to phenomena such as tunneling, heterojunction barriers, and defect-related recombination, which are critical for accurately modeling thin-film and tandem structures. The last part of the chapter focuses on the material systems central to this thesis: amorphous and nanocrystalline silicon (a-Si:H and nc-Si:H) as established thin-film absorbers, and metal halide perovskites as emerging high-performance alternatives. Their distinct structural, electronic, and optical characteristics are discussed, including the roles of disorder, defect states, and band alignment.

2.1. Solar Cell Characterization

This section first discusses the illuminated current–voltage (I–V) curve and its diode model, which define the main performance metrics of a solar cell. Then this section goes into the wavelength-resolved quantum efficiency, where the External and Internal Quantum Efficiency (EQE, IQE) provide insight into optical absorption, carrier collection, and recombination losses.

2.1.1. Current–Voltage Characteristics

The illuminated current–voltage curve, shown in Figure 2.1, shows the performance of a solar cell under standard test conditions. At zero voltage, the device delivers its short-circuit current I_{sc}, which corresponds to the maximum photocurrent generated by absorbed light. As the applied voltage increases, the current decreases due to the diode-like behavior of the junction, until it reaches zero at the open-circuit voltage V_{oc}, where no current is extracted [16]. The diode-like shape arises because a solar cell is essentially a p–n junction under illumination. In the dark, the junction behaves as a diode: forward bias reduces the barrier at the depletion region, allowing carriers to flow, while reverse bias increases the barrier and suppresses current. Under illumination, light generates excess carriers that are swept across the junction by the built-in electric field, adding a photocurrent to the diode response.

This diode-like behaviour comes from the dark current of the junction, described by the Shockley equation [53]:

$$I_{\mathrm{dark}}(V) = I_0 \left[\exp\left(\frac{qV}{nkT} \right) - 1 \right], \tag{2.1}$$

where I_0 is the reverse saturation current, n the ideality factor, q the elementary charge, k the Boltzmann constant, and T the absolute temperature. When the junction is illuminated, a light-generated current

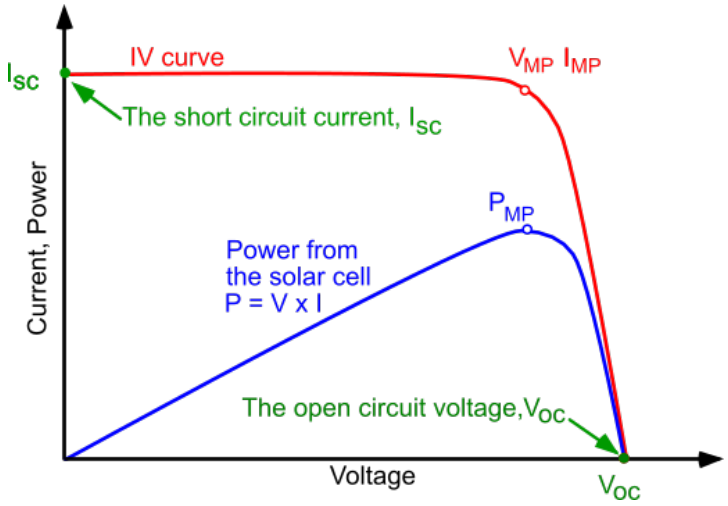

Figure 2.1: Illuminated current–voltage (I–V) and power–voltage (P–V) characteristics of a solar cell. Key points include the short-circuit current I_{sc}, open-circuit voltage V_{oc}, and the maximum power point $(V_{\text{mpp}}, I_{\text{mpp}})$ [18].

I_{ph} is added, resulting in

$$I(V) = I_{\text{ph}} - I_0 \left[\exp\left(\frac{qV}{nkT} \right) - 1 \right]. \tag{2.2}$$

For real devices, resistive losses must also be considered. The series resistance R_s accounts for contact and bulk resistance, while the shunt resistance R_{sh} models leakage currents and non-ideal shunt paths. Including these effects gives the one-diode model:

$$I(V) = I_{\text{ph}} - I_0 \left[\exp\left(\frac{q(V + IR_s)}{nkT} \right) - 1 \right] - \frac{V + IR_s}{R_{sh}}. \tag{2.3}$$

The equivalent circuit of this one diode model is shown in Figure 2.2. At short-circuit ($V = 0$), the exponential term vanishes and $I \approx I_{\text{ph}} = I_{\text{sc}}$. At open-circuit ($I = 0$), the recombination current balances the photocurrent, giving

$$V_{\text{oc}} = \frac{nkT}{q} \ln\left(\frac{I_{\text{ph}}}{I_0} + 1 \right). \tag{2.4}$$

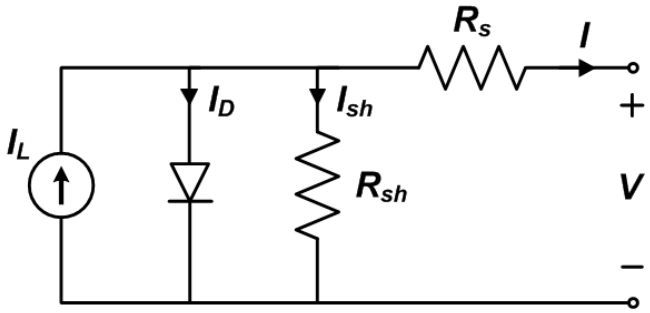

Figure 2.2: Equivalent one-diode circuit model of a solar cell, consisting of a photocurrent source in parallel with a diode, a series resistance R_s, and a shunt resistance R_{sh}[53].

Going back to Figure 2.1, the power output at any operating point is simply the product of voltage and current:

$$P = V \cdot I. \tag{2.5}$$

This is represented by the blue curve in Figure 2.1. The maximum power point (MPP) occurs at the coordinates $(V_{\text{mpp}}, I_{\text{mpp}})$, giving

$$P_{\text{max}} = V_{\text{mpp}} \cdot I_{\text{mpp}}. \tag{2.6}$$

The fill factor (FF) quantifies how sharp the corner of the I–V curve is:

$$\mathrm{FF} = \frac{V_{\mathrm{mpp}} \cdot I_{\mathrm{mpp}}}{V_{\mathrm{oc}} \cdot I_{\mathrm{sc}}}. \tag{2.7}$$

Finally, the power conversion efficiency η is given by the ratio of maximum electrical power to the incident optical power P_{in}, typically 1000 W/m^2 under AM1.5G illumination [16]:

$$\eta = \frac{V_{\mathrm{oc}} \cdot I_{\mathrm{sc}} \cdot \mathrm{FF}}{P_{\mathrm{in}}}. \tag{2.8}$$

These parameters serve as the benchmark for evaluating the simulated devices in this thesis, and form the basis for later calibration with the experimental data.

2.1.2. Quantum Efficiency: EQE and IQE

While the I–V curve gives information on the overall electrical performance, quantum efficiency measurements give wavelength-resolved information on how effective a solar cell converts incident photons into collected charge carriers. This is describes by the EQE, which is given by the following ratio [16]:

$$\mathrm{EQE}(\lambda) = \frac{\text{Number of collected carriers at } \lambda}{\text{Number of incident photons at } \lambda} \tag{2.9}$$

Experimentally, the EQE is measured by shining monochromatic light of known intensity onto the cell and getting the resulting photocurrent. The EQE is typically expressed as a function of wavelength and reflects both optical and electrical losses within the device.

To separate out optical effects such as reflection and transmission, the Internal Quantum Efficiency (IQE) is defined as:

$$\mathrm{IQE}(\lambda) = \frac{\mathrm{EQE}(\lambda)}{\mathrm{Absorptance}(\lambda)} \tag{2.10}$$

The IQE isolates the electrical response by accounting for the fraction of photons actually absorbed in the active region. It provides a measure of how efficiently the cell collects carriers generated by absorbed photons and is useful for analyzing recombination losses and material quality.

Spectral analysis using the EQE and the IQE can help identify performance-limiting features such as poor collection in certain layers, weak absorption in specific spectral regions, or losses at interfaces. In addition to spectral diagnostics, the EQE spectrum is directly related to the short-circuit current density. By integrating the EQE over the solar photon flux spectrum, the expected current density, J_{sc}, can be obtained as:

$$J_{\mathrm{sc}} = q \int_{\lambda} \mathrm{EQE}(\lambda)\, \Phi_{\mathrm{ph}}(\lambda)\, d\lambda, \tag{2.11}$$

where q is the elementary charge and $\Phi_{\mathrm{ph}}(\lambda)$ is the incident photon flux.

2.2. Drift-Diffusion Model

The operation of a solar cell is governed by the transport of charge carriers through the semiconductor layers. This transport occurs via two main mechanisms: drift, driven by the electric field, and diffusion, driven by carrier concentration gradients. Together with charge conservation, these processes are described by the drift–diffusion model, which forms the foundation of most semiconductor device simulations [36].

The model consists of three coupled components. Poisson's equation relates the electrostatic potential to the local charge distribution, thus determining the internal electric field. The continuity equations makes sure of charge conservation by linking carrier densities to generation, recombination, and current

flow. Finally, the drift–diffusion equations describe how electrons and holes move under the electric field and concentration gradients. When solved together with Poisson's and the continuity equations, they give a complete picture of carrier transport in the device.

2.2.1. Poisson's Equation

The electrostatic potential ϕ inside a semiconductor is governed by *Poisson's equation*, which relates the potential to the local charge density ρ:

$$\nabla \cdot (\varepsilon \nabla \phi) = -\rho \tag{2.12}$$

The total charge density can be expressed as:

$$\rho = q\left(p - n + N_D^+ - N_A^-\right) - \rho_{\text{trap}} \tag{2.13}$$

Here, n and p are the concentrations of electrons and holes, N_D^+ and N_A^- denote the densities of ionized donors and acceptors, and ρ_{trap} represents charge stored in traps or interface states. The parameter ε is the material's permittivity, which determines how strongly it responds to electric fields.

Physically, Poisson's equation describes how charge within the device shapes the electrostatic potential. A region with excess positive charge bends the potential downward, while negative charge bends it upward. Because the electric field is the spatial derivative of the potential,

$$\mathbf{E} = -\nabla \phi,$$

this equation directly connects the charge distribution inside the semiconductor to the internal electric fields that drive carrier transport and determine junction behavior [19].

2.2.2. Continuity Equations

The continuity equations represent the conservation of charge carriers. They describe how the local concentration of electrons and holes evolves over time due to current flow, carrier generation (G), and recombination (R):

$$\frac{\partial n}{\partial t} = \frac{1}{q}\nabla \cdot \mathbf{J_n} + G - R \tag{2.14}$$

$$\frac{\partial p}{\partial t} = -\frac{1}{q}\nabla \cdot \mathbf{J_p} + G - R \tag{2.15}$$

Here, n and p are again the electron and hole concentrations, $\mathbf{J_n}$ and $\mathbf{J_p}$ are the corresponding current density vectors, and q is the elementary charge. The terms G and R represent the generation and recombination rates of electron–hole pairs, respectively.

In semiconductors, the occupation of energy states by charge carriers is governed by Fermi–Dirac statistics, which defines the probability that an electronic state at a given energy is occupied. This distribution becomes particularly important under non-equilibrium conditions, where the separation of electron and hole quasi-Fermi levels determines the local carrier concentrations and thus directly influences generation and recombination processes.

2.2.3. Drift-Diffusion Equations

The total current densities of electrons and holes are described by the drift-diffusion equations, which combine both electric-field-driven and concentration-driven transport:

$$\mathbf{J_n} = qn\mu_n \mathbf{E} + qD_n \nabla n \tag{2.16}$$

$$\mathbf{J_p} = qp\mu_p \mathbf{E} - qD_p \nabla p \tag{2.17}$$

In these expressions, μ_n and μ_p are the mobilities of electrons and holes, D_n and D_p are the diffusion coefficients, and $\mathbf{E}$ is the electric field, which is related to the electrostatic potential by, as was already

stated in Section 2.2.1. Furthermore, the relationship between the diffusion coefficient and mobility is given by the Einstein relation:

$$\frac{D_n}{\mu_n} = \frac{D_p}{\mu_p} = \frac{kT}{q} \tag{2.18}$$

where k is the Boltzmann constant and T is the absolute temperature.

Solving the continuity equations together with Poisson's equation and the drift-diffusion relations gives a complete description of carrier behavior in the solar cell. This coupled system of partial differential equations is typically solved numerically to obtain spatial profiles of carrier densities, electric field, and potential [60, 66].

2.3. p–i–n Junction Structure

In semiconductor materials with low carrier mobilities, such as a-Si:H, the conventional p–n junction is often replaced by the p–i–n structure to ensure efficient carrier collection. A typical p–i–n junction consists of a thin p-type layer, a relatively thick intrinsic (undoped) absorber layer, and a thin n-type layer, as illustrated in the upper part of Figure 2.3 [34].

Unlike p–n junctions, which rely primarily on carrier diffusion, p–i–n devices are dominated by drift-driven transport. A strong built-in electric field develops across the entire intrinsic region, enabling photogenerated electrons and holes to be separated and collected efficiently, even in materials with short diffusion lengths.

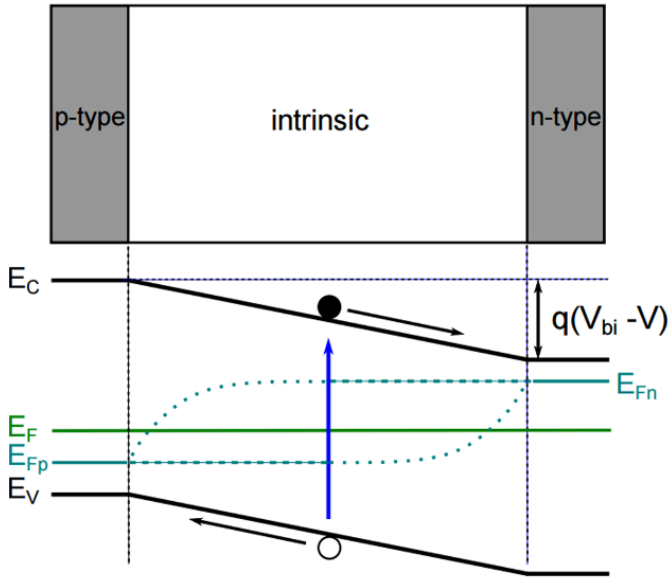

Figure 2.3: Band diagram of a p–i–n junction under forward bias, showing the electric field across the intrinsic layer and drift-based carrier separation. Adapted from [34].

The internal electric field causes electrons to drift toward the n-type side and holes toward the p-type side. This field strength can be approximated by:

$$\mathbf{E} \approx \frac{q(V_{\text{bi}} - V)}{d_i} \tag{2.19}$$

where V_{bi} is the built-in potential, V is the applied bias voltage, d_i is the thickness of the intrinsic layer, and q is the elementary charge. As the external bias increases (e.g., under illumination), the effective field is reduced, which can impact carrier collection efficiency. The sloped energy bands in Figure 2.3 reflect the presence of this field and visually indicate the drift forces acting on electrons and holes. This

field-assisted separation makes the p–i–n structure suitable for thin-film solar cells, where diffusion-based collection is limited due to low mobility and short carrier lifetimes.

2.4. Carrier Generation and Recombination

The performance of a solar cell is fundamentally determined by the balance between the generation of charge carriers through light absorption and their loss through recombination. Generation creates electron–hole pairs that contribute to the photocurrent, while recombination reduces the number of collected carriers, thereby limiting current and voltage. This section describes the dominant recombination mechanisms [1].

Figure 2.4 shows the three most relevant recombination processes in semiconductors: (A) radiative recombination, (B) Auger recombination, and (C) trap-assisted Shockley–Read–Hall (SRH) recombination.

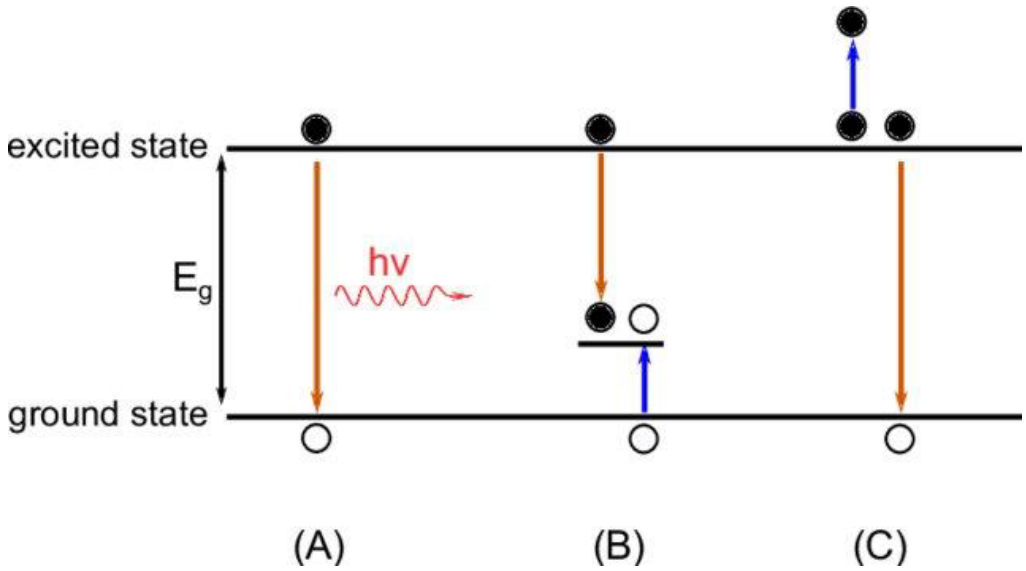

Figure 2.4: Overview of recombination mechanisms in semiconductors. (A) Radiative recombination, (B) Thermalization losses, (C) Trap-assisted (Shockley–Read–Hall) recombination. Adapted from [47].

2.4.1. Radiative Recombination

Radiative recombination occurs when an electron from the conduction band recombines with a hole in the valence band, releasing energy in the form of a photon, as illustrated in Figure 2.4A. This intrinsic process dominates in materials with direct bandgaps, where the conduction-band minimum and valence-band maximum occur at the same crystal momentum, allowing efficient photon emission. In indirect bandgap semiconductors such as crystalline silicon (c-Si), radiative recombination is relatively weak because a phonon is required to conserve momentum during the transition.

In hydrogenated amorphous silicon (a-Si:H), the lack of long-range atomic order removes the strict momentum conservation rule that distinguishes direct from indirect transitions. Optically, a-Si:H therefore behaves somewhat like a direct bandgap material, exhibiting a high absorption coefficient. However, electrically, the high density of localized defect and tail states introduces efficient non-radiative recombination pathways, making radiative recombination a minor process in practice. As a result, photon emission from a-Si:H is negligible, and radiative recombination contributes little to carrier loss compared to defect-related mechanisms.

The radiative recombination rate can be expressed as:

$$R_{\text{rad}} = B(np - n_i^2), \tag{2.20}$$

where B is the radiative recombination coefficient and n_i is the intrinsic carrier concentration.

2.4.2. Auger Recombination

The Auger recombination is a three-particle process where the energy released during recombination is transferred to a third carrier, which is excited to a higher energy state, as can be seen in Figure 2.4C. This process does not emit a photon and instead leads to additional heating. Auger recombination becomes important at high carrier concentrations, particularly in heavily doped or highly illuminated regions. The Auger recombination rate is given by:

$$R_{\text{Auger}} = C_n n(np - n_i^2) + C_p p(np - n_i^2) \tag{2.21}$$

where C_n and C_p are the Auger coefficients for electrons and holes, respectively.

2.4.3. Shockley–Read–Hall Recombination

Lastly, in disordered semiconductors such as amorphous silicon Shockley–Read–Hall recombination is most dominant. This process involves recombination through intermediate energy states located within the bandgap, as can be seen in Figure 2.4B. Within these states electrons and holes can recombine non-radiatively.

The dynamics of the trap occupations are controlled by carrier capture and emission processes, as can be seen in Figure 2.5.

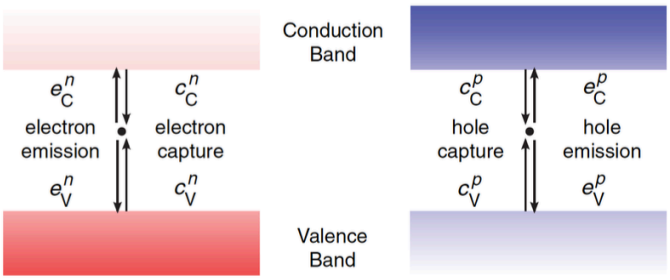

Figure 2.5: Trap occupation dynamics. Left: electron picture, Right: hole picture. Electrons and holes are captured and emitted from defect states in the bandgap. Adapted from [66].

There are four possible transitions: capture and emission of electrons from the conduction band, and capture and emission of holes from the valence band. These processes determine the electron occupation f_t of a trap, which evolves according to:

$$\frac{\partial f_t}{\partial t} = (1 - f_t)\,(c_C^n + c_V^p) - f_t\,(e_C^n + e_V^p) \tag{2.22}$$

Here c_C^n and c_V^p are the capture rates from the conduction and valence band respectively, and e_C^n and e_V^p are the emission rates. At steady state, the occupation f_t becomes constant, and the net recombination rate is given by:

$$R_{\text{net}} = \frac{N_t\, v_{\text{th}}^n\, v_{\text{th}}^p\, \sigma_n\, \sigma_p\, (np - n_{i,\text{eff}}^2)}{v_{\text{th}}^n \sigma_n (n + n_1/g_n) + v_{\text{th}}^p \sigma_p (p + p_1/g_p)} \tag{2.23}$$

Here N_t is the trap density, σ_n, σ_p are the electron and hole capture cross sections, v_{th}^n, v_{th}^p the thermal velocities. Furthermore, g_n and g_p are the degeneracy factors and lastly, n_1 and p_1 are the auxiliary concentrations defined as:

$$n_1 = n_{i,\text{eff}} \exp\left(\frac{E_T - E_F}{k_B T}\right), \quad p_1 = n_{i,\text{eff}} \exp\left(\frac{E_F - E_T}{k_B T}\right) \tag{2.24}$$

where E_T is the trap energy level, E_F is the Fermi level, k_B is the Boltzmann constant, and T is temperature. This model provides a basis for describing how trap states cause recombination, especially in disordered materials with high densities of tail and midgap states.

2.5. Tunneling and Hetero interfaces

In thin-film solar cells, adjacent semiconductor layers often possess different electronic and optical properties, leading to the formation of hetero-junctions. These interfaces introduce additional physical effects not present in homo-junction devices, such as band-edge discontinuities, enhanced interface recombination, and tunneling phenomena. Such effects are particularly significant in hetero structures where large differences in band alignment, carrier affinity, or defect density can strongly influence carrier transport and recombination dynamics at the interface. They are also crucial in tandem solar cells featuring tunnel recombination junctions, where efficient charge transfer across the hetero interface is essential to ensure current continuity and maintain high overall device efficiency.

At a hetero-junction interface, the conduction and valence bands of the two materials do not align continuously. Instead, the difference in electron affinity and bandgap leads to band offsets at the interface. The conduction band offset ΔE_c and valence band offset ΔE_v are defined as:

$$\Delta E_c = \chi_2 - \chi_1, \quad \Delta E_g = \Delta E_v + \Delta E_c \tag{2.25}$$

where χ is the electron affinity and E_g is the bandgap of each material. These offsets can act as barriers to carrier transport, particularly if one carrier type accumulates at the interface. To overcome such barriers, there are several ways, such as diffusion, thermionic emission and tunneling. These are discussed below.

2.5.1. Thermionic Emission

Thermionic emission refers to the release of electrons from a material when they have sufficient thermal energy to overcome a potential barrier. In metals, this barrier corresponds to the work function, while in semiconductors it is often described as the barrier height at a junction. At elevated temperatures, a fraction of electrons gain enough energy to escape into the vacuum or across an interface.

The resulting current density is described by the following equation [66]:

$$J = A^* T^2 \exp\left(-\frac{q\phi_0}{kT}\right), \tag{2.26}$$

where J is the emission current density, T the absolute temperature, ϕ_0 the barrier height (or work function), q the elementary charge, and k the Boltzmann constant. The effective Richardson constant A^* depends on the material properties and is given by:

$$A^* = \frac{4\pi q m_n^* k^2}{h^3}, \tag{2.27}$$

with m_n^* the effective electron mass and h Planck's constant.

In words, these relations show that the thermionic emission current increases rapidly with temperature and decreases exponentially with the barrier height, meaning that even small changes in temperature or interface potential can strongly affect carrier transport across a junction.

2.5.2. Tunneling

When a potential barrier between two regions is sufficiently thin, charge carriers can quantum mechanically tunnel through it, even if their energy is below the barrier height. Unlike thermionic emission, which relies on carriers acquiring enough thermal energy to overcome the barrier, tunneling allows transport via quantum mechanical penetration. This is not merely a theoretical effect, it plays a critical role in solar cell operation, particularly in structures with ultra-thin layers or high electric fields. Under such conditions, tunneling mechanisms such as direct tunneling (DT), band-to-band tunneling (B2BT), and trap-assisted tunneling (TAT) become especially relevant, each influencing carrier transport and recombination in different ways depending on the device design and operating conditions.

In direct tunneling, carriers pass through a narrow barrier while remaining within the same energy band. In contrast, both B2BT and TAT involve interband transitions, for instance, a hole from the valence band of a p-type region may tunnel into the conduction band of a neighboring n-type region. B2BT requires favorable band alignment, such that under strong electric fields, the valence and conduction bands overlap sufficiently to enable tunneling. TAT, however, does not depend on such alignment. Instead, it relies on defect states within the bandgap that act as intermediate energy levels, enabling carriers to tunnel in steps through these localized traps. As visualization of B2BT and TAT is given in Figure 3.7 in Section 3.3.4.

As a result, TAT tends to dominate in materials or interfaces with high defect densities, such as amorphous silicon or defective interfaces, while B2BT is more relevant in engineered tunnel junctions, where steep band bending and clean interfaces are present.

In semiconductor device modeling, tunneling is treated as an additional carrier generation mechanism, represented by a local generation rate G_{tun}. This term is included in the carrier continuity equations alongside optical generation and non-radiative recombination processes such as Shockley–Read–Hall (SRH) recombination. Physically, G_{tun} accounts for the quantum-mechanical transport of carriers through potential barriers rather than over them.

The tunneling process is associated with a current density J_{tun}, and the corresponding generation rate can be expressed as [22]:

$$G_{\text{tun}}(r) = \frac{1}{q}\nabla \cdot J_{\text{tun}} = \frac{1}{q}\frac{dJ_{\text{tun}}}{d\psi}\nabla\psi = \frac{dJ_{\text{tun}}}{dE}\cdot \mathbf{E}, \tag{2.28}$$

where ψ is the electrostatic potential, $\mathbf{E}$ the local electric field, E the carrier energy, and q the elementary charge. This formulation links the spatial divergence of the tunneling current to an equivalent local generation rate, ensuring that tunneling is self-consistently coupled to the carrier transport equations.

The local tunneling generation rate is typically written as [22]:

$$G_{\text{tun}}(r) = \frac{AT^2}{k_B}\,\mathbf{E}\cdot\Gamma(r)\ln\left(\frac{1+\exp[-q(\psi-\phi_n)/k_BT]}{1+\exp[-q(\psi-\phi_p)/k_BT]}\right), \tag{2.29}$$

where A is a material-dependent prefactor, $\Gamma(r)$ the tunneling probability, k_B the Boltzmann constant, and ϕ_n, ϕ_p the electron and hole quasi-Fermi potentials. The logarithmic term ensures that the tunneling process follows Fermi–Dirac statistics, meaning it depends on the local carrier occupation of the states involved.

The tunneling probability $\Gamma(r)$ quantifies how likely a carrier is to penetrate the potential barrier and is commonly evaluated using the Wentzel–Kramers–Brillouin (WKB) approximation:

$$\Gamma(r) = \exp\left[-\frac{2}{\hbar}\int_0^r \sqrt{2m^*\left(\frac{\phi_b}{q}+\phi_m-\psi(x)\right)}\,dx\right], \tag{2.30}$$

where $\hbar$ is the reduced Planck constant, m^* the carrier effective mass, ϕ_b the barrier potential, and $\psi(x)$ the local electrostatic potential. This exponential dependence highlights the extreme sensitivity of tunneling to both barrier height and thickness: even a small increase in either can drastically reduce the tunneling probability. Consequently, significant tunneling currents occur only under strong electric fields or in ultrathin layers.

In materials or interfaces containing defect states, carriers may tunnel via TAT. In this mechanism, electrons and holes do not tunnel directly between the conduction and valence bands but instead transition in steps through localized trap states. The nonlocal TAT recombination rate can be expressed as [66]:

$$R_n^{TAT} = C_n \int \Gamma_c(x,E)\,\Gamma_v(x,E)\,\exp\left[-\frac{2}{\hbar}\int_0^x \kappa_c(x',E)\,dx'\right] f^n(x)\,f^p(x)\,dE, \tag{2.31}$$

where Γ_c and Γ_v are the capture probabilities for electrons and holes, κ_c is the WKB decay constant, and f^n, f^p are the occupation probabilities of the trap for electrons and holes, respectively. Depending

on whether lattice vibrations participate in the process, tunneling can occur either elastically (without energy exchange) or inelastically (with phonon emission or absorption).

In simple terms, these equations describe how quantum tunneling acts as a generation or recombination pathway that depends exponentially on the barrier properties and strongly on local electric fields.

2.6. Defect states

In materials with structural disorder, such as amorphous or nanocrystalline silicon, a high density of localized energy states can form within the bandgap. These defect states arise from broken or distorted bonds and disrupt the ideal periodic lattice structure found in crystalline materials. Unlike conventional crystalline silicon, where the conduction and valence bands have well-defined edges, disordered materials exhibit additional energy states within the bandgap, typically classified as band tail states and midgap states.

The tail states result from variations in bond lengths and angles and extend exponentially from the conduction and valence band edges into the bandgap. These shallow states contribute to the exponential absorption edge and are characterized by the Urbach energy E_U, which quantifies the degree of structural disorder [64, 70]. In contrast, midgap states, referred to as dangling bonds, appear near the center of the bandgap due to unsatisfied or broken silicon bonds. Both types of states are illustrated in Figure 2.6.

Once present, these defect states can strongly affect solar cell performance. They act as non-radiative recombination centers, hinder carrier transport by trapping free carriers, and facilitate tunneling via intermediate energy levels. Their impact is particularly critical when located in the absorber (active) layer, where they directly influence photocurrent generation and carrier lifetimes. However, defects in supporting or contact layers can also affect interfacial recombination and charge extraction, depending on their energy levels and spatial distribution.

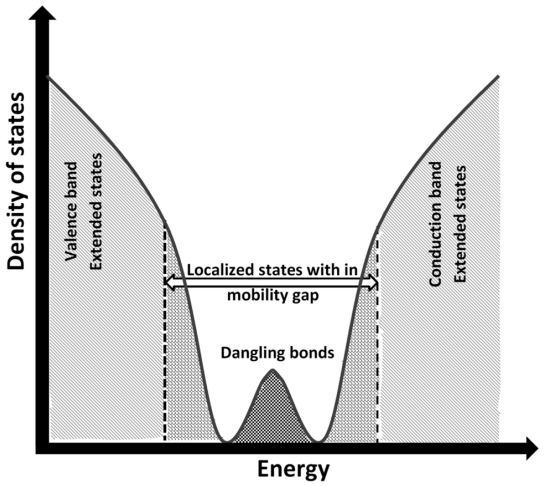

Figure 2.6: Schematic density of states (DOS) in amorphous silicon showing localized defect states. Tail states extend exponentially from the conduction and valence bands into the bandgap due to disorder, while deeper midgap states (e.g., dangling bonds) appear within the mobility gap and act as recombination or tunneling centers. Adapted from [7].

The mobility gap, also indicated in Figure 2.6, defines the energy threshold above which (in the conduction band) or below which (in the valence band) carriers can move in extended states and contribute to conduction.

In the Sentaurus simulation the form for describing band-tail states is the exponential distribution, where the density of states decays exponentially away from the band edge:

$$g(E) = N_0 \exp\left(-\frac{|E - E_0|}{E_U}\right). \tag{2.32}$$

Here, again, E_U represents a characteristic decay energy, the Urbach energy, that quantifies the degree

of structural disorder.

For the dangling bonds near midgap, a Gaussian distribution is used:

$$g(E) = N_0 \exp\left(-\frac{(E - E_0)^2}{2E_S^2}\right). \tag{2.33}$$

In this case, E_0 is the central energy level (often the midgap), while E_S is the energetic width of the distribution.

2.7. Thin Film silicon devices

Thin-film silicon solar cells use materials with high absorption coefficients, which allow the use of absorber layers only a few hundred nanometers to a few micrometers thick. This significantly reduces material consumption compared to crystalline silicon solar cells, which typically require absorber thicknesses exceeding 100 μm due to their indirect bandgap and relatively low absorption coefficient. The reduced thickness, however, also modifies the electrical behavior of the device, which must be carefully understood and modeled, as will be discussed in the following sections for a-Si:H, nc-Si:H and the a-Si:H/nc-Si:H tandem.

2.7.1. Amorphous Silicon

Amorphous materials differ fundamentally from crystalline ones in that they lack a well-defined, repeating atomic structure. While crystals are built from a periodic lattice with uniform bond lengths and angles, amorphous structures exhibit irregularities that lack long-range order. Despite this disorder, the short-range atomic arrangement in amorphous materials often closely resembles that of the corresponding crystalline phase. However, the disruption in periodicity means that not all atoms can form the ideal number of bonds, resulting in the presence of dangling bonds as discussed in the previous section, Section 2.6 [57]. Figure 2.7 shows the crystal structure of different materials. Here the leftmost structure, the monocrystalline structure, represents the structure that is present in c-Si. In c-Si there is a well ordered structure. When looking at a-Si:H however, the structure is in line with the right most structure. Here there is no long-range atomic order.

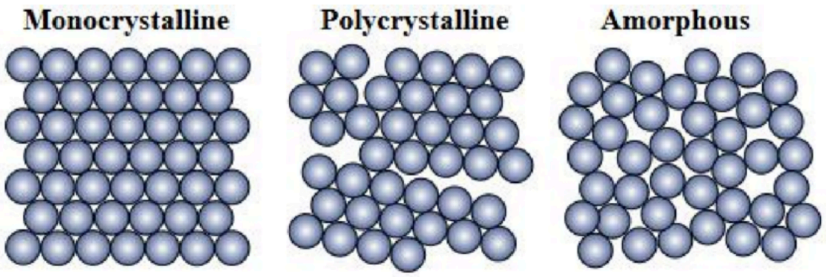

Figure 2.7: Schematic representation of atomic arrangements in monocrystalline, polycrystalline, and amorphous silicon. Adapted from [2].

Besides influencing the structure, the lack of long-range order in a-Si:H also affects how charges move through the material. In crystalline semiconductors, the periodic lattice enables efficient transport [33]. In contrast, the disorder in a-Si:H disrupts this periodicity, so carriers near the band edges cannot form such delocalized states (see Section 2.6). Instead, their wavefunctions become localized and decay exponentially away from their center [4]. This localization lowers carrier mobility and, if the disorder is strong enough, can even lead to insulating behavior [32].

In addition to band tails, structural defects, such as dangling bonds, introduce localized states within the bandgap. Unlike in crystalline silicon, these defect-induced states do not all lie at a single energy but instead form an energy distribution, further shaping the disordered density of states. Carriers trapped in such states cannot participate in long-range conduction and are instead transported via thermally activated hopping, particularly at room temperature.

Beyond its inherent structural and electronic disorder, hydrogenated amorphous silicon (a-Si:H) also exhibits light-induced metastability, commonly known as the Staebler–Wronski Effect (SWE). Upon illumination, the material forms additional dangling bonds, which introduce defect states into the bandgap and degrade device performance by acting as non-radiative recombination centers. This degradation is typically linked to two microscopic mechanisms. First, weak bond breaking, where photogenerated carriers provide enough energy to disrupt already strained Si–Si bonds. Second, hydrogen motion, in which mobile hydrogen atoms move away from previously passivated sites, reactivating dangling bonds. Although thermal annealing can partially reverse these effects, the SWE remains a significant limitation in a-Si:H-based solar cells [62].

2.7.2. Nanocrystalline Silicon

Compared to a-Si:H, hydrogenated nanocrystalline silicon (nc-Si:H) is more stable under light exposure and has a lower bandgap, which makes it an attractive material for thin-film tandem solar cells. Structurally, it is a mixed-phase material: small crystalline grains are embedded in an amorphous matrix, and voids or low-density regions can also be present. The crystalline grains can vary widely in size, from a few nanometers up to several microns [64, 43].

The transition from amorphous to nanocrystalline silicon growth during plasma-enhanced chemical vapor deposition (PECVD) is primarily governed by the hydrogen dilution ratio. This is illustrated in Figure 2.8. At low dilution levels, the deposited film is predominantly amorphous. As the dilution increases, the material enters an incubation regime where crystallite nucleation begins. Once the hydrogen dilution ratio exceeds a critical threshold (typically $d_H > 50$, where d_H is the ratio of hydrogen to silane gas flow), nanocrystalline growth becomes dominant. At very high dilution, the entire film can become nanocrystalline [12].

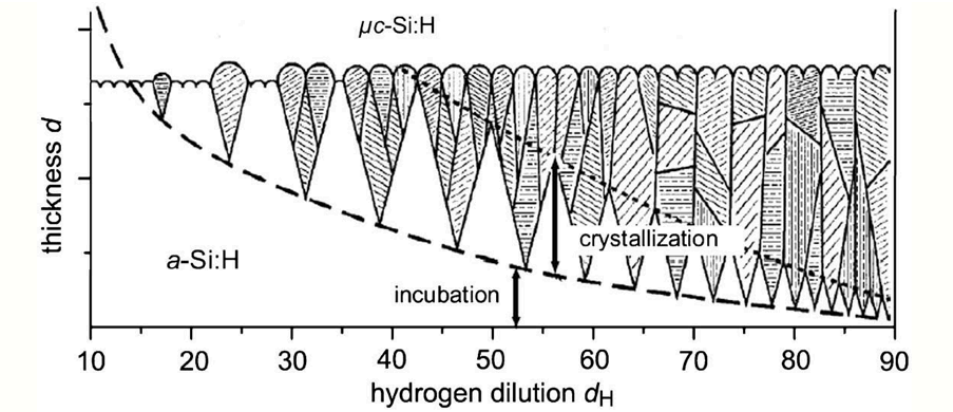

Figure 2.8: Crystallization of nc-Si:H as a function of hydrogen dilution ratio, showing the transition from amorphous to nanocrystalline material. Adapted from [12].

The density of states (DOS) in nc-Si:H reflects this mixed-phase nature. The crystalline grains contribute a DOS similar to crystalline silicon, with sharp band edges and few midgap states. In contrast, the amorphous regions add exponential band-tail states and defect-related states such as dangling bonds. The combination of these two components gives nc-Si:H higher carrier mobilities and longer diffusion lengths than a-Si:H, while still keeping the high absorption coefficient of an amorphous material [64, 59].

Optical spectroscopy studies of nc-Si:H films embedded in p–i–n solar cell structures have confirmed this strong link between structure and electronic properties. Sancho-Parramon et al. [50] showed that nc-Si:H layers contain both ”small” (2–3 nm) and ”large” (8–20 nm) crystallites, and that the bandgap increases with the fraction of small crystallites due to quantum confinement effects. At the same time, the sub-gap absorption exhibits an Urbach tail whose width and defect density both rise with increasing crystallinity, reflecting the influence of grain boundaries. These boundaries, which form between misoriented crystallites, act as barriers to carrier transport and sites for carrier scattering. They can also

localize defect states, further enhancing recombination and optical absorption losses. These results highlight that the optical and electrical properties of nc-Si:H can vary widely throughout the material.

2.7.3. a-Si/nc-Si tandem solar cell

To overcome the efficiency limitations of single-junction thin-film silicon devices, tandem structures combining materials with different bandgaps have been developed. A widely used design is the a-Si/nc-Si tandem solar cell, which stacks a hydrogenated amorphous silicon top cell with a hydrogenated nanocrystalline silicon bottom cell. This configuration takes advantage of the high optical bandgap of a-Si:H (around 1.7–1.8 eV) together with the lower bandgap of nc-Si:H (around 1.1–1.2 eV), forming a near-optimal pair for harvesting the solar spectrum under AM1.5 illumination [43, 56].

In this structure, the a-Si:H top cell absorbs the high-energy (short-wavelength) part of the spectrum, while the nc-Si:H bottom cell captures the longer-wavelength photons transmitted through the top junction. Because nc-Si:H has an indirect bandgap and a relatively low absorption coefficient near its band edge, the bottom cell must be significantly thicker (typically 1–3 μm) to generate sufficient photocurrent. Conversely, the a-Si:H absorber is intentionally kept thin (200–300 nm) to reduce the impact of light-induced degradation. Together, the two junctions combine the stability and spectral complementarity required for higher overall efficiencies than either single-junction device.

The electrical output of the tandem device is governed by the way the subcells are connected in series. The open-circuit voltage is the sum of the voltages of the two junctions,

$$V_{oc,\text{tandem}} = V_{oc,\text{top}} + V_{oc,\text{bottom}},$$

since each subcell contributes its own quasi-Fermi level splitting under illumination. This additive voltage is a key advantage of tandem designs, enabling higher V_{oc} than possible with a single absorber material.

In contrast, the short-circuit current is not additive but constrained by the weaker subcell. Because the same current must pass through both junctions in series, the total photocurrent is determined by the limiting junction:

$$J_{sc,\text{tandem}} = \min(J_{sc,\text{top}}, J_{sc,\text{bottom}}).$$

If one subcell generates less current, it acts as a bottleneck, restricting the overall device output. For this reason current matching is a critical design requirement: the optical absorption and layer thicknesses must be carefully optimized so that both subcells deliver nearly equal photocurrents under AM1.5 illumination, which will be further discussed in the Section 6.

2.8. Metal Halide Perovskites for Tandem Integration

While a-Si/nc-Si tandem solar cells offer a practical route to surpass the efficiency limits of single-junction thin-film silicon devices, their performance remains constrained by inherent material limitations. To address these bottlenecks, recent research has explored integrating metal halide perovskites as a pathway to overcome these effiency limitations. Perovskites combine excellent optoelectronic properties with low-cost, scalable fabrication, making them highly attractive for high-efficiency tandem configurations. The following sections introduce the structural, electronic, and interfacial properties of metal halide perovskites, with a focus on their compatibility with tandem architectures and the role of the hole transport layer (HTL) in enabling efficient and stable device operation.

2.8.1. Material and Structural Properties

Metal halide perovskites are defined by their characteristic crystal structure, expressed by the general formula ABX_3, where each letter represents a different type of ion:

- A is a large, positively charged ion (cation), which can be organic (e.g., methylammonium MA^+ or formamidinium FA^+) or inorganic (e.g., cesium Cs^+).
- B is a smaller divalent metal cation, typically lead (Pb^{2+}) or tin (Sn^{2+}).
- X is a negatively charged halide ion (Cl^-, Br^-, or I^-).

These ions form a three-dimensional lattice in which each B atom sits at the center of an octahedron made of six halide ions (BX_6), and the larger A-site cations occupy the spaces between them, as shown in Figure 2.9. This simple yet highly flexible framework is what gives perovskites their name and many of their exceptional electronic and optical properties [23].

The geometric "fit" between these ions determines how stable the crystal is. This is often described by the Goldschmidt tolerance factor, a dimensionless quantity that depends on the relative ionic radii of A, B, and X. When the ions fit well, typically when the tolerance factor is close to one, the lattice remains symmetric and stable; when they do not, the structure distorts or becomes unstable. In essence, the tolerance factor provides a quick way to assess whether a given combination of ions can form a stable perovskite phase [23].

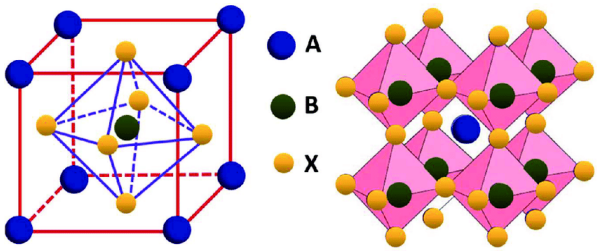

Figure 2.9: Schematic crystal structure of the perovskite lattice (ABX_3), consisting of corner-sharing BX_6 octahedra with the A-site cation in the central void. Adapted from [23].

This structural versatility allows perovskites to combine a set of properties that are highly advantageous for photovoltaic operation. Their high absorption coefficient (typically exceeding 10^5 cm^{-1}) enables efficient absorption of visible light within just a few hundred nanometers. Charge transport remains efficient due to long carrier diffusion lengths, often several micrometers, and balanced electron and hole mobilities in the range of 10–50 $cm^2V^{-1}s^{-1}$. Furthermore, perovskites exhibit an exceptional degree of defect tolerance: their intrinsic defects tend to be shallow and therefore cause minimal non-radiative recombination losses. As a result, the loss in open-circuit voltage is considerably lower than in most solution-processed semiconductors, allowing perovskite solar cells to operate close to their radiative (Shockley–Queisser) limit [20]. Their bandgap can also be tuned between 1.2 and 2.3 eV by adjusting the halide and cation composition, making them suitable for both single-junction and tandem architectures [3].

Despite these favorable properties, perovskite solar cells still face challenges related to long-term stability. The soft ionic lattice is prone to degradation when exposed to moisture, oxygen, heat, or ultraviolet light, leading to phase segregation and ion migration. In mixed-halide compositions, halide redistribution under illumination or bias can cause local bandgap variations and hysteresis effects. Moreover, the interfaces between the perovskite and charge transport layers are often chemically unstable: reactions, dopant diffusion, and defect formation at these boundaries can accelerate degradation and reduce device lifetime [26].

2.8.2. Device Structure

A typical perovskite solar cell consists of a perovskite absorber layer sandwiched between an ETL and a hole transport layer HTL, which selectively extract electrons and holes while blocking the opposite carrier type. Two main configurations are commonly employed: the conventional n–i–p and the inverted p–i–n architecture. In the former, the light enters through the ETL side, while in the latter, it enters through the HTL side. The inverted architecture offers improved interface stability, reduced hysteresis, and compatibility with flexible, low-temperature processing, making it particularly suitable for tandem and scalable device fabrication [23, 3]. Among these, the interfaces, particularly the perovskite/HTL boundary, strongly influence both efficiency and stability, emphasizing the importance of interfacial engineering discussed below. Different HTL materials will be introduced below.

2.8.3. The Role of the Hole Transport Layer

The HTL serves as an energy-selective, defect-tolerant contact that defines the boundary conditions of the device. Its main functions are: (i) to align energetically with the perovskite valence band for efficient

hole extraction, (ii) to block electrons and suppress interfacial recombination, (iii) to provide sufficient lateral conductivity with minimal series resistance, and (iv) to act as a chemical and physical barrier against metal diffusion and environmental degradation [5, 39, 72].

An effective HTL must therefore combine favorable energy-level alignment (valence-band offset $\lesssim$0.2 eV), a large conduction-band offset ($\gtrsim$0.3–0.5 eV), high hole mobility, optical transparency, and compatibility with low-temperature deposition. Depending on these requirements, three material classes are typically used: organic polymers (e.g., PEDOT:PSS, PTAA), inorganic oxides or chalcogenides (e.g., NiO_x, CuI, CuSCN), and self-assembled monolayers (SAMs, e.g., MeO-2PACz), each offering specific trade-offs between efficiency, processability, and stability [39, 72].

Organic HTLs such as PEDOT:PSS and PTAA are popular due to their simple, solution-based processing and good interface formation with the perovskite. However, PEDOT:PSS is hygroscopic and acidic, which can lead to interface degradation. PTAA requires dopants (e.g., LiTFSI, tBP) to enhance conductivity, dopants that can migrate into the perovskite and cause instability [39].

Inorganic HTLs, notably NiO_x, offer greater chemical and thermal robustness. NiO_x combines a wide bandgap (3.6–3.8 eV) with a deep valence band (-5.2 to -5.4 eV) and moderate hole mobility ($\sim$0.1 cm^2/Vs). Doping with Li, Cu, or Mg can improve its conductivity and interface energetics, though high defect densities at the interface may enhance recombination. Other inorganic HTLs such as CuI, CuSCN, and Cu_2O are being explored for their high mobility and stability but remain limited by processing constraints [72].

A more recent class of HTLs relies on self-assembled monolayers (SAMs), which form ultrathin dipole layers at the TCO/perovskite interface. SAMs consist of an anchoring group, a linker chain, and a terminal group that tunes interfacial energetics and perovskite crystallization. As shown in Figure 2.10, these molecular layers modify the TCO work function, suppress interface recombination, and promote uniform perovskite growth through hydrophobic surface termination [72]. Such interlayers have boosted device efficiencies from below 12% to over 26%, underscoring their importance for high-performance inverted architectures [27].

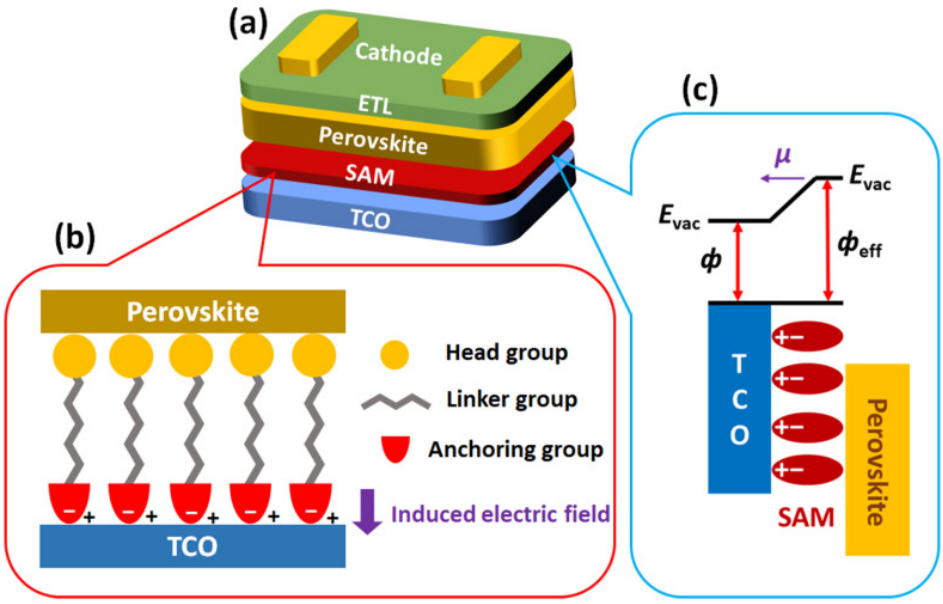

Figure 2.10: Schematic illustration of self-assembled monolayer (SAM) hole-transporting materials in perovskite solar cells. (a) Device architecture including a SAM between the TCO and perovskite. (b) Molecular structure of SAMs, consisting of anchoring, linker, and head groups. (c) Dipole-induced vacuum level shift at the TCO/SAM interface, resulting in an effective work function ϕ_{eff} that improves energy-level alignment with the perovskite. Adapted from [72].

In this work, the suitability of nanocrystalline silicon oxide (nc-SiO_x) as an alternative hole transport layer (HTL) is examined. The nc-SiO_x(p) layer, analogous to the p^+ contacts used in a-Si:H and nc-Si:H

solar cells, offers tunable band alignment and high optical transparency owing to its mixed amorphous–nanocrystalline microstructure. Its oxygen content and doping level can be tailored to adjust both the work function and electrical conductivity, enabling favorable interface alignment with perovskite absorbers. Although its conductivity is lower than that of conventional transparent conductors, it is comparable to or slightly higher than that of typical wide-bandgap oxide HTLs such as Ni_x, depending on deposition conditions. The main challenges instead arise from its higher defect density and potential for increased interface recombination. Despite these limitations, nc-SiO_x(p) provides a valuable test case for hybrid silicon–perovskite integration and interface engineering in tandem architectures.

3

Methodology

This chapter presents the optical and electrical simulation methodologies used to design and analyze a series of thin-film photovoltaic devices. Three main device families were modeled: (i) single-junction a-Si:H and nc-Si:H solar cells, (ii) monolithic a-Si:H/nc-Si:H tandem structures, and (iii) perovskite-based devices, including single-junction, hybrid a-Si:H/perovskite, and all-perovskite tandems. The silicon-based tandems were simulated on both rigid Asahi U-type textured glass and flexible foil substrates, while all perovskite-based configurations were modeled exclusively on flexible thin-film platforms.

For each device architecture, the optical response was simulated using GenPro4, and the resulting spectrally and spatially resolved generation profiles were coupled to the electrical drift–diffusion solver in TCAD Sentaurus. This consistent optical–electrical coupling enables a quantitative assessment of how material properties, interfaces, and device geometry influence carrier transport and overall photovoltaic performance.

The chapter is structured as follows. Section 3.1 introduces the device architectures, including the single-junction, tandem, and flexible configurations, and explains how the validated silicon tandem model was extended to flexible thin-film architectures. Section 3.2 then details the optical modeling workflow and the derivation of wavelength- and depth-dependent generation profiles in GenPro4. Finally, Section 3.3 outlines the electrical simulation procedure in Sentaurus, in which Section 3.3 summarizes the physical models for recombination, defects, and tunneling as well as the numerical settings.

3.1. Device Structure

This section summarizes the simulated device stacks and the material configurations implemented in the electrical simulations. Three silicon baseline structures were modeled: a single-junction a-Si:H cell, a single-junction nc-Si:H cell, and a monolithic a-Si:H/nc-Si:H tandem. The framework was subsequently extended to flexible thin-film and perovskite-based configurations. An overview of all simulated device families, their substrate types, and the evaluated HTLs is provided in Table 3.1.

The calibration procedure and the numerical values of the key material and defect parameters for the silicon-based models are presented in Chapter 4. In contrast, the perovskite-based configurations were not explicitly calibrated; their material parameters were taken directly from experimental and literature sources, as detailed in this section. For any layers originating from the silicon-based tandem architecture, reference is made to the corresponding calibrated parameters in Section 4.

Table 3.1: Overview of simulated device families by substrate type and HTLs compared. A dash (–) indicates a fixed nc-SiO_x(p) contact. For the all-perovskite tandem: *Inorganic* = NiO_x/NiO_x, *Organic* = PTAA/PEDOT:PSS, *Hybrid* = nc-SiO_x(p)/nc-SiO_x(p).

Device family	Substrate type	HTL(s) evaluated
a-Si:H (single-junction)	Rigid (Asahi glass)	–
nc-Si:H (single-junction)	Rigid (Honeycomb glass)	–
a-Si:H/nc-Si:H (tandem)	Rigid (Honeycomb glass)	–
a-Si:H/nc-Si:H (tandem)	Flexible foil	–
Perovskite (single-junction)	Flexible foil	PEDOT:PSS, PTAA, NiO_x, 2PACz, nc-SiO_x(p)
Hybrid a-Si:H/perovskite (tandem)	Flexible foil	NiO_x
All-perovskite (tandem)	Flexible foil	Inorganic, Organic, Hybrid

The following subsections describe the silicon-based device architectures, followed by how these models are transformed from a rigid substrate to a flexible one. In Section 3.1.3 the perovskite-based configurations, which build directly upon the silicon model foundations are shown.

3.1.1. Silicon-Based Models

Figure 3.1 illustrates the representative stack used for the a-Si:H single-junction solar cell, with analogous configurations for the nc-Si:H and tandem devices.

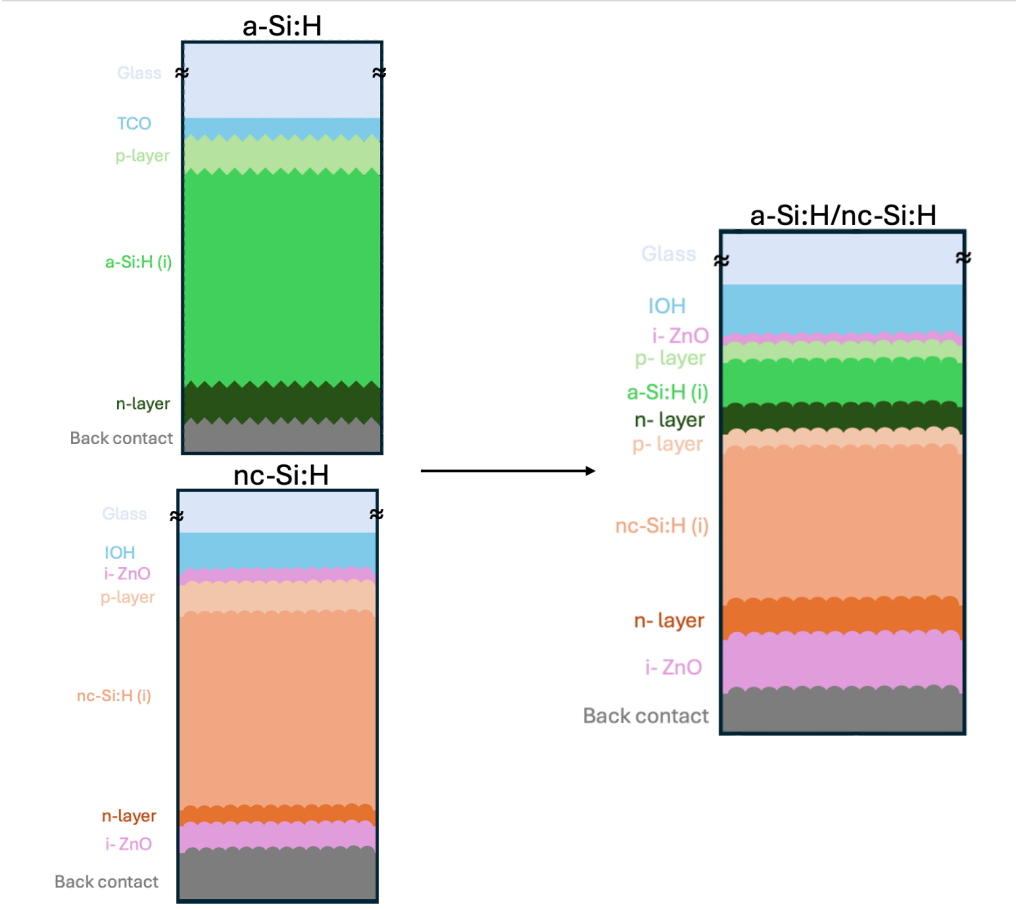

Figure 3.1: Schematic cross-section of the simulated single-junction a-Si:H solar cell structure. Analogous stacks are used for the nc-Si:H and a-Si:H/nc-Si:H tandem devices.

Top Subcell: a-Si:H Junction

The a-Si:H single-junction device is designed to exploit the high absorption coefficient of amorphous silicon in the visible range. To enhance light trapping, it is deposited on an Asahi-type textured glass

substrate with a random nanoscale texture morphology. This texture scatters incident photons, increasing their optical path length and thereby improving absorption in the thin intrinsic layer, while remaining compatible with fabrication [67].

In addition to the optical constants of the individual layers, the measured surface morphologies of the textured substrates and deposited films were included in the optical simulations. Atomic force microscopy (AFM) data of the Asahi texture were used to represent the real nanoscale surface roughness in the optical model, ensuring that scattering, absorption, and interference effects were realistically captured rather than idealized.

On top of the substrate, a transparent conductive oxide (TCO) of aluminum-doped zinc oxide (AZO) serves as the front electrode, combining optical transparency with good lateral conductivity. Beneath the TCO lies a bilayer p-type nc-SiO_x contact (heavily doped p^{++} followed by moderately doped p^{+}), which in the optical model is treated as an effective single p-layer. The intrinsic a-Si:H absorber is approximately 300 nm thick, a thickness chosen to absorb most visible photons while minimizing light-induced degradation. Finally, a thin n-type nc-SiO_x contact is included to extract electrons while remaining optically transparent to longer-wavelength photons.

Bottom Subcell: nc-Si:H Junction

The nc-Si:H device targets absorption in the red and near-infrared parts of the spectrum, where amorphous silicon becomes transparent. To enhance long-wavelength light trapping, it is deposited on a honeycomb-textured glass substrate. Unlike the random Asahi texture, this honeycomb pattern provides controlled periodic scattering, which significantly improves absorption at longer wavelengths [73].

The device follows a p–i–n layout. The front contact stack consists of an indium–oxide–hydrogen (IOH) layer for lateral conductivity, combined with a thin intrinsic ZnO buffer to improve interface quality and band alignment [49]. This is followed by a thin nc-SiO_x(p) hole-selective contact. The intrinsic absorber is 3.2 µm thick and subdivided into multiple sublayers in the simulation to represent depth-dependent crystallinity (see Section 4.3). This captures the experimentally observed increase in crystalline fraction with thickness. Carrier extraction is facilitated by a rear nc-SiO_x(n) contact and an i-ZnO buffer, while a silver (Ag) reflector ensures strong back reflection to boost long-wavelength absorption.

a-Si:H/nc-Si:H Tandem Device Structure

The tandem device combines the complementary absorption characteristics of a-Si:H and nc-Si:H in a monolithic, series-connected configuration. The front side again employs the honeycomb-textured glass superstrate and IOH/ZnO TCO stack to provide optimal light management for both subcells.

The a-Si:H top cell follows a standard p–i–n layout, consisting of an nc-SiO_x(p) contact, a thin a-SiO_x window layer, a $\sim$300 nm intrinsic a-Si:H absorber, and an nc-SiO_x(n) electron contact. Directly beneath it, the p-layer of the nc-Si:H bottom cell contacts the n-layer of the top cell, forming a TRJ. The TRJ enables efficient recombination of electrons from the top cell with holes from the bottom cell, thereby maintaining current continuity through both subcells. More about the modeling of the TRJ follows in Section 3.3.4.

The nc-Si:H bottom subcell consists of a $\sim$3.0 µm thick intrinsic absorber, again divided into sublayers to reflect its depth-dependent crystallinity. This is followed by a rear nc-SiO_x(n) contact and a ZnO buffer, with a silver (Ag) back electrode acting as a reflector to maximize infrared absorption. Together, the two junctions form a tandem structure with a combined spectral response spanning both visible and near-infrared wavelengths.

All silicon-based models described in this section were individually calibrated in Section 4 before extending the framework to the perovskite-based configurations. The final parameter values can also be seen in Section C.1 of Appendix C.

3.1.2. Flexible solar cells

The validated Asahi-based tandem model obtained with the methodolgy described in the previous sections was extended to investigate flexible thin-film architectures. In these configurations, the rigid glass superstrate was replaced by lightweight metallic foils to enable mechanical flexibility and compatibility with roll-to-roll manufacturing. The objective of this modeling step was to quantify the optical impact of

replacing the glass/IOH/ZnO front stack with flexible alternatives and to assess the resulting changes in device photocurrent.

The flexible architecture was implemented by substituting the rigid Asahi substrate with an aluminum foil that serves as a mechanically flexible support and reflective back electrode. The optical and electrical stacks were then adapted accordingly, maintaining identical absorber and contact layer definitions to isolate front-stack effects. The simulations focused on two main front-stack variants derived from experimental developments in flexible thin-film silicon photovoltaics:

1. Factory baseline configuration: an FTO front electrode stack deposited on a flexible foil, without additional encapsulation.
2. Encapsulated configuration: the same FTO front electrode combined with a multilayer encapsulant composed of alternating layers of EFTE (ethylene–tetrafluoroethylene) and optical glue.

In the encapsulated configuration, the multilayer stack produces a graded refractive index transition at the air–substrate interface [29]. This optical grading minimizes Fresnel reflections and enhances light incoupling while simultaneously providing mechanical protection during bending and roll-to-roll processing. Both configurations were implemented in GenPro4 using the same optical modeling workflow as described in Section 3.2, ensuring a consistent comparison with the reference Asahi case.

Additionally, surface texturing was introduced to reproduce the light-scattering properties of Asahi glass. Modulated texturing on temporary aluminum foils, as demonstrated by Limodio et al. [29], was reproduced in the optical model. This approach enables the evaluation of photon incoupling improvements without modifying the absorber or electrical transport parameters.

A schematic overview of the three front-stack configurations considered: (i) reference Asahi glass, (ii) factory baseline foil, and (iii) factory foil with encapsulant. This is shown in Figure 3.2. The layer thicknesses are not drawn to scale. Each configuration was simulated under AM1.5G illumination, and the resulting spectrally resolved optical generation profiles were exported for subsequent electrical simulation in Sentaurus.

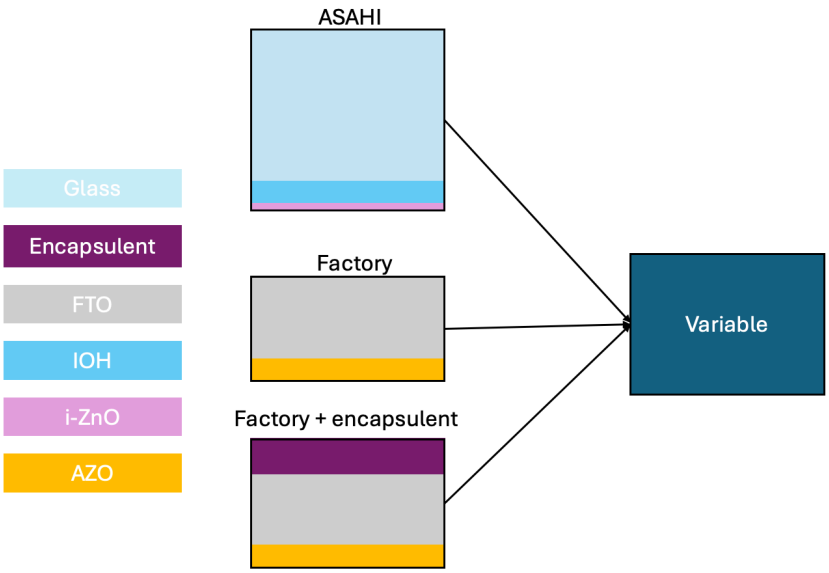

Figure 3.2: Schematic overview of the simulated front-stack configurations: (top) reference Asahi U-type textured glass with IOH and i-ZnO; (middle) factory baseline foil with FTO/AZO; (bottom) factory foil combined with an encapsulant. The flexible variants reuse the electrical baseline of the Asahi reference and differ only in optical stack and substrate.

3.1.3. Perovskite-based Devices

This section extends the modeling framework describes in the previous sections to perovskite solar cells. First, a SJ perovskite cell is constructed to benchmark different HTL materials. Next, a hybrid a-Si:H/perovskite tandem configuration is defined by integrating the calibrated a-Si:H top junction with

a narrow-bandgap perovskite bottom cell. Finally, an all-perovskite tandem architecture is specified, enabling direct comparison between inorganic, organic, and silicon-based HTLs across both subcells. Recombination and interface kinetics are not treated here; they follow the global framework of Section 3.3. Furthermore, schematic device structures of each model can be found in Appendix C.

Single-junction perovskite device

A single-junction narrow-bandgap (1.23 eV) Sn–Pb perovskite device serves as the baseline for the hybrid and all-perovskite tandem configurations. The electron transport stack consists of a C_{60} ETL and a thin bathocuproine (BCP) buffer layer. The inclusion of BCP introduces a conduction-band offset that suppresses electron backflow from the perovskite into C_{60}. The material parameters for these layers are summarized in Table 3.2.

Table 3.2: Material parameters of the narrow-bandgap Sn–Pb perovskite absorber, C_{60} ETL, and BCP buffer layer used in the simulations.

Parameter	Perovskite	C_{60}	BCP
Thickness (nm)	900	25	8
Bandgap E_g (eV)	1.23	2.1	3.5
Electron affinity χ (eV)	3.9	3.9	2.5
Permittivity ε_r	20	10	10
Doping (cm^{-3})	—	1.0×10^{19}	1.0×10^{2}
CB DOS N_C (cm^{-3})	1.0×10^{18}	2.0×10^{18}	2.0×10^{18}
VB DOS N_V (cm^{-3})	1.0×10^{18}	2.0×10^{19}	1.8×10^{19}
Mobility μ_n ($cm^2V^{-1}s^{-1}$)	20	8.9×10^{-4}	1.0×10^{-3}
Mobility μ_p ($cm^2V^{-1}s^{-1}$)	10	8.9×10^{-4}	5.0×10^{-2}

Hole transport layers (HTLs): material parameters

Table 3.3 lists the bulk parameters used for PEDOT:PSS, PTAA, NiO_x, and the 2PACz self-assembled monolayer (SAM). For nc-SiO_x(p), the parameters of the a-Si:H p-layer from Table 4.8 in Section C are reused. Additionally, while 2PACz is intrinsically undoped, an effective acceptor density is included to reproduce the interfacial dipole-induced band alignment at the perovskite contact.

Table 3.3: Bulk material parameters used for the HTLs.

Parameter	PEDOT:PSS	PTAA	NiO_x	2PACz
Thickness (nm)	20	20	20	$\sim$2
E_g (eV)	1.60	3.30	3.80	3.40
χ (eV)	3.50	1.8	1.46	1.7
ε_r	3.0	3.0	10.7	10
N_C (cm^{-3})	2.2×10^{18}	2.2×10^{18}	2.2×10^{18}	2.0×10^{18}
N_V (cm^{-3})	1.8×10^{19}	1.8×10^{19}	1.8×10^{19}	2.0×10^{19}
μ_n ($cm^2V^{-1}s^{-1}$)	1.8×10^{-3}	4×10^{-5}	1×10^{-3}	1×10^{-3}
μ_p ($cm^2V^{-1}s^{-1}$)	1.9×10^{-2}	4×10^{-5}	1×10^{-3}	1×10^{-3}
N_A (cm^{-3})	1.0×10^{19}	1.0×10^{19}	1.0×10^{19}	1.0×10^{20}

Hybrid a-Si:H/perovskite tandem

To bridge silicon and perovskite technologies, a two-terminal hybrid a-Si:H/perovskite tandem was simulated. The top a-Si:H junction from the validated a-Si:H/nc-Si:H tandem (Section 4.4) was retained, while the bottom nc-Si:H subcell was replaced by a narrow-bandgap perovskite absorber ($E_g = 1.23$ eV) modeled as described in Section 3.1.3.

The perovskite subcell employed the same C_{60}/BCP ETL stack as the single-junction configuration and NiO_x as the HTL, forming a p–i–n structure. The two subcells were monolithically connected through a thin indium tin oxide (ITO) TRJ that links the n-type a-Si:H to the p-type NiO_x layer, where B2BT was activated.

All optical and electrical parameters from the calibrated silicon tandem were retained, ensuring that any performance differences arise solely from replacing the bottom junction.

All-perovskite tandem architecture

An all-perovskite two-terminal tandem was then modeled, consisting of a wide-bandgap (WBG, $E_{\mathrm{g}} = 1.67$ eV) top subcell and a narrow-bandgap (NBG, $E_{\mathrm{g}} = 1.23$ eV) bottom subcell. The influence of the HTL composition in the top and bottom cells ($HTL_{\mathrm{ToC}}/HTL_{\mathrm{BoC}}$) was examined through three configurations:

1. Inorganic: NiO_x/NiO_x
2. Organic: PTAA/PEDOT:PSS
3. Hybrid: nc-SiO_x(p)/nc-SiO_x(p)

All non-HTL layers, optical constants, and electrical parameters were kept identical across configurations to ensure a controlled comparison. The absorber thicknesses were fixed at 280 nm for the WBG perovskite and 900 nm for the NBG perovskite to maintain the optical current-matching condition for the NiO_x reference configuration.

The material parameters of the WBG perovskite absorber were adopted from [44]: electron affinity $\chi = 4.0$ eV, relative permittivity $\varepsilon_r = 6.5$, effective density of states $N_{\mathrm{C}} = 1 \times 10^{20}$ cm^{-3} and $N_{\mathrm{V}} = 1 \times 10^{19}$ cm^{-3}, and carrier mobilities $\mu_n = \mu_p = 35$ cm^{2}V^{-1}s^{-1}. These values were consistently applied to all three tandem variants to isolate the effect of HTL composition.

For the inorganic and organic configurations, both HTLs were p-doped to an acceptor concentration of $N_{\mathrm{A}} = 2 \times 10^{19}$ cm^{-3} to maintain comparable built-in electric fields. In the hybrid nc-SiO_x(p)/nc-SiO_x(p) case, the HTL doping parameters were taken directly from the calibrated a-Si:H/nc-Si:H tandem (Table 4.8), ensuring physical consistency with the silicon-based device architecture.

For the top nc-SiO_x(p) layer, the thickness of the single-junction perovskite configuration (13 nm) was retained. The PEDOT:PSS, NiO_x, and bottom nc-SiO_x(p) layers were kept at 20 nm thickness in all other configurations. The complete layer sequences for the inorganic and organic configurations are listed in Appendix C.

3.2. Optical Modeling

Following the definition of the device structures in Section 3.1, the next step is to determine how light is absorbed and distributed within each layer of the stack. Accurate optical modeling is essential, as it defines the spatially resolved carrier generation rates that serve as input for the subsequent electrical simulations. This section describes the simulation approach used to model the optical response of all device types—ranging from single-junction silicon cells to flexible and perovskite-based tandems—using GenPro4, and explains how the resulting generation profiles were coupled to Sentaurus Device.

The contrast in optical thickness requirements between amorphous and nanocrystalline silicon is illustrated in Figure 3.3. Amorphous silicon (a-Si:H) exhibits very high absorption in the visible spectrum ($\sim 10^5$–10^6 cm^{-1}), allowing most above-bandgap photons to be absorbed within a $\sim$300 nm layer. In contrast, nanocrystalline silicon (nc-Si:H), with its smaller bandgap ($\sim$1.2 eV) and much lower absorption coefficient in the near-infrared (10^2–10^3 cm^{-1}), requires micrometer-scale absorbers to capture long-wavelength light efficiently. These complementary absorption characteristics form the physical basis for tandem architectures that combine both materials to extend the spectral response from the visible to the near-infrared.

In addition to silicon absorbers, a low-bandgap perovskite (NBG PVK) with a bandgap of approximately 1.23 eV is included for comparison. This perovskite exhibits strong and broadband absorption ($\alpha \sim 10^5$ cm^{-1}) that extends well into the near-infrared, making it suitable for use as a bottom cell material in all-perovskite or hybrid tandem configurations. Compared to a-Si:H and nc-Si:H, the NBG perovskite combines the strong absorption of amorphous silicon in the visible with enhanced long-wavelength response, thereby providing an effective reference for next-generation thin-film tandem architectures.

The optical response of each complete multilayer stack was simulated using GenPro4, a MATLAB-based one-dimensional optical solver developed for photovoltaic applications [54]. The tool computes

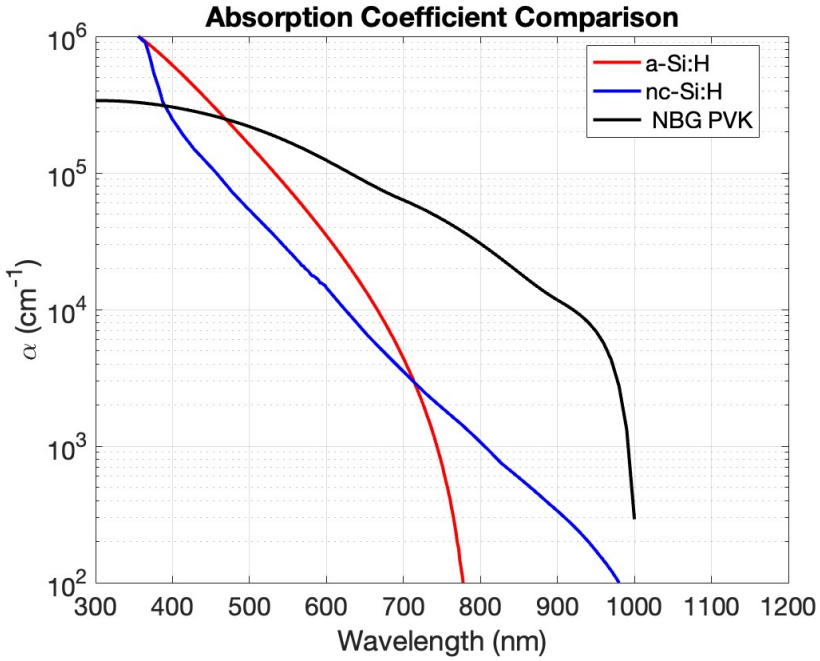

Figure 3.3: Absorption coefficients of a-Si:H, nc-Si:H, and narrow-bandgap (NBG) perovskite. a-Si:H and perovskite exhibit very high absorption coefficients ($\sim 10^5$–10^6 cm^{-1}), while nc-Si:H requires micrometer-scale thickness to absorb near-infrared light. The NBG perovskite (1.23 eV) extends absorption further into the infrared, illustrating its suitability for bottom-cell applications.

light propagation through the stack by accounting for reflection, transmission, and absorption at every interface, and outputs spectrally and spatially resolved absorption profiles. These data were subsequently converted into wavelength- and depth-dependent optical generation rates, which were then used as input for the electrical device simulations in Sentaurus Device.Sentaurus Device.

3.2.1. Layer-by-Layer Absorptance and Photocurrent

The absorption of light is not uniform across the device stack but depends strongly on both wavelength and depth. Using GenPro4, the depth- and wavelength-resolved absorption $A(x, \lambda)$ was obtained for each structure (a-Si:H, nc-Si:H, tandem, and flexible/perovskite configurations). By integrating $A(x, \lambda)$ over the thickness of each layer, the spectral absorptance $A_i(\lambda)$ is determined, directly linking individual layers to their photocurrent contribution.

Figure 3.4 illustrates this for the a-Si:H single-junction cell. The absorptance spectra for the nc-Si:H SJ, a-Si:H/nc-Si:H tandem, hybrid a-Si:H/PVK tandem and full perovkskite tandem can be found in Appendix D. For the aborptance spectrum shown here the intrinsic a-Si:H absorber (shown in green) dominates the photocurrent, while the thin doped and contact layers mainly act as transparent transport windows. In the nc-Si:H device, by contrast, the much lower absorption coefficient at long wavelengths requires a thicker ($\sim$3 µm) intrinsic layer, so that the photocurrent contribution is distributed more gradually through the absorber. In the tandem device, these complementary thicknesses combine: the a-Si:H top cell absorbs high-energy photons in the visible range, while the nc-Si:H bottom cell captures the transmitted red and near-infrared photons.

To use this information in the electrical device simulations, the local optical generation rate is calculated as:

$$G(x, \lambda) = \frac{A(x, \lambda)}{\Delta x} \phi(\lambda), \tag{3.1}$$

where Δx is the slice thickness which is the numerical thickness of each depth element in the simulation grid and $\phi(\lambda)$ the incident photon flux [eh/cm^2/s] derived from the AM1.5G spectrum [35]:

$$\phi(\lambda) = \frac{I(\lambda)\,\lambda}{hc}. \tag{3.2}$$

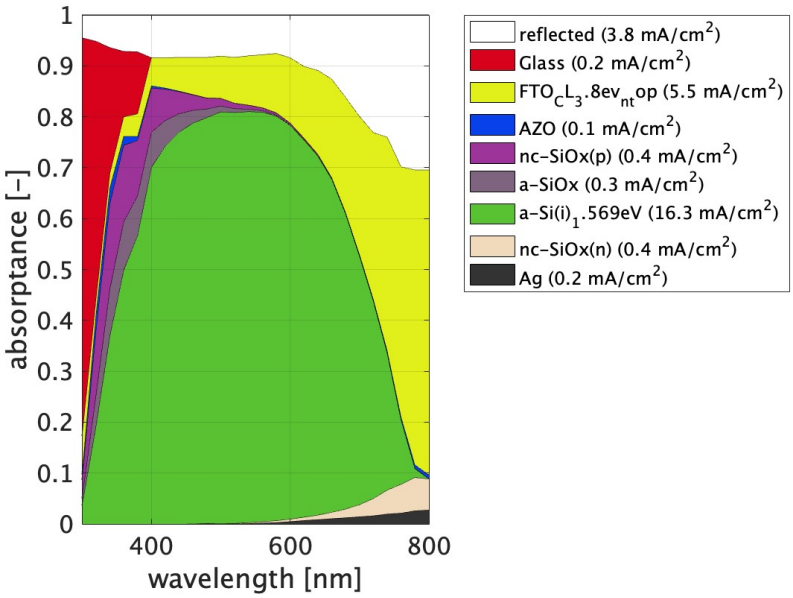

Figure 3.4: Layer-resolved absorptance and photocurrent contribution for the a-Si:H single-junction solar cell model. Similar analyses were carried out for the nc-Si:H single junction and the a-Si:H/nc-Si:H tandem device.

Here $I(\lambda)$ is the spectral irradiance, h Planck's constant, and c the speed of light. This formulation guarantees photon conservation: each absorbed photon contributes one electron–hole pair to the carrier generation profile $G(x, \lambda)$.

Figure 3.5 shows $G(x, \lambda)$ for representative wavelengths, which come from these calculations. In the a-Si:H device, short-wavelength photons (e.g. 400 nm) are absorbed almost entirely within the front region, while longer wavelengths penetrate deeper. In the nc-Si:H device, absorption is weaker and extends much further into the thick intrinsic layer, consistent with its lower bandgap. A special correction procedure was applied to remove an unphysical spike in the optical generation profile at 320 nm while conserving total absorbed charge; this method is described in Appendix D.6.

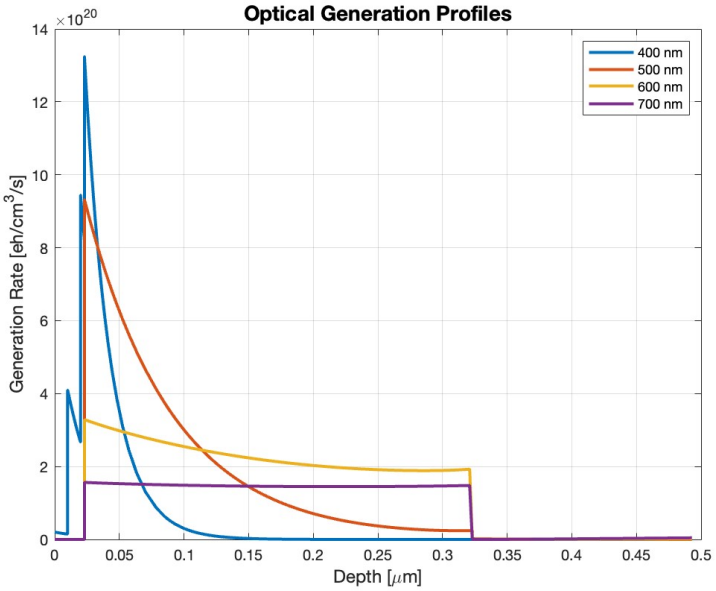

Figure 3.5: Wavelength- and depth-resolved generation rate $G(x, \lambda)$ obtained from GenPro4 of the a-Si:H single junction solar cell. Short-wavelength photons are absorbed near the surface of the a-Si:H top cell, while long-wavelength photons penetrate into the nc-Si:H absorber in the single junction and tandem devices.

3.3. Electrical Modeling

The electrical simulations were performed using the Sentaurus TCAD suite, which self-consistently solves charge transport and recombination processes within the device. Figure 3.6 outlines the complete workflow. First, the optical generation profile—computed in MATLAB using GenPro4—was imported into Sentaurus Device as a wavelength- and depth-resolved source term. Subsequently, the semiconductor transport equations were solved to obtain current–voltage (IV) characteristics, carrier distributions, and recombination rates.

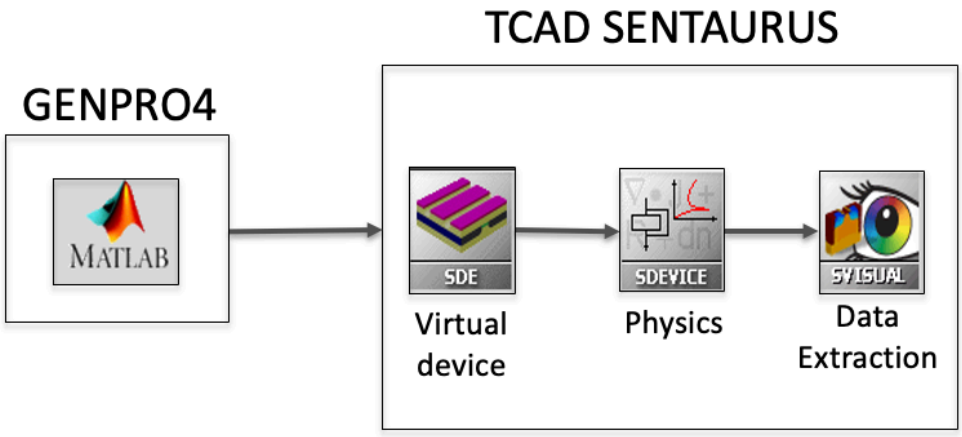

Figure 3.6: Simulation workflow. Optical generation is computed with GenPro4 and imported into Sentaurus, where transport, recombination, and tunneling models are solved self-consistently.

All devices were modeled using the drift–diffusion formalism, which couples Poisson's equation with the electron and hole continuity equations. This approach captures how internal electric fields and carrier concentration gradients drive charge motion in each layer. A two-dimensional simulation domain was used to account for lateral transport, which cannot be represented in one dimension [66].

Because thin-film silicon often exhibit high defect densities and strong internal fields, the numerical

system is highly nonlinear.To ensure stable convergence, voltage ramping, adaptive mesh refinement, and quasistationary stepping were employed throughout the simulations.

The electrical modeling framework combines global transport models with region-specific descriptions of recombination and tunneling. The methodology can be divided into three components: (i) coupling to the optical generation profiles, (ii) carrier transport and recombination modeling, and (iii) numerical stabilization and convergence strategies.

3.3.1. Optical Excitation and Coupling

The optical field was provided externally by GenPro4, which calculates the spatial and spectral distribution of photon absorption. For standard IV simulations, the full AM1.5G solar spectrum was used. For EQE calculations, the device was illuminated with a monochromatic probe, and the resulting photocurrent was normalized by the incident photon flux.

In tandem devices, bias illumination was introduced to isolate each subcell: long-wavelength light (≈900 nm) saturates the bottom nc-Si:H cell when probing the top a-Si:H or perovskite junction, while short-wavelength light (≈350 nm) saturates the top subcell when probing the bottom one. This method ensures that each EQE curve represents the active junction only.

3.3.2. Global Transport Models

Carrier transport in all layers was modeled using the drift–diffusion formalism, the standard framework for simulating charge motion in thin-film photovoltaic devices [66]. In this approach, the total current density is given by the sum of two components: drift, driven by the internal electric field, and diffusion, driven by carrier concentration gradients. Fermi–Dirac statistics were applied to ensure accurate carrier occupation under high doping levels and in the presence of localized defect states, which can shift the quasi-Fermi levels.

Charge transfer across heterointerfaces was modeled using thermionic emission, accounting for carrier transport over potential energy barriers [17]. Under high electric fields, velocity saturation effects were included through a field-dependent mobility model [48]. Bandgap narrowing was neglected, since in amorphous and nanocrystalline silicon the dominant electronic broadening arises from band tails and disorder-induced localized states rather than heavy doping.

3.3.3. Defect States and Recombination

Accurate modeling of defect-related recombination is critical for thin-film materials such as a-Si:H, nc-Si:H, and perovskites, where localized states strongly influence carrier lifetime and transport. The recombination framework used in this work combines both bulk and interfacial effects, with material-specific descriptions for silicon and perovskite layers.

Amorphous and nanocrystalline silicon.

In a-Si:H and nc-Si:H, nonradiative recombination was modeled using a combination of exponential band-tail states and Gaussian midgap defect distributions. These states represent localized traps arising from disorder and dangling bonds, respectively. Distinct electron and hole capture cross sections were assigned to reproduce the experimentally observed asymmetry in carrier trapping.

To reflect the gradual change in microstructure within nc-Si:H, the defect representation was made depth-dependent. Experimental studies show that the crystalline fraction increases with film thickness, leading to fewer localized states near the back interface. Accordingly, the 3.2 µm intrinsic nc-Si:H absorber was subdivided into three sublayers (ncSi1–ncSi3), each with progressively increasing tail-state densities and wider Gaussian defect widths [51]. This spatially resolved approach reproduces the variation in recombination and carrier transport across the film thickness. The specific defect parameters used for these sublayers are listed in Table 4.8 (Section 4.4.5).

Perovskite-based devices.

In the perovskite layers, bulk recombination was described using the Shockley–Read–Hall (SRH) formalism, while interfacial losses were represented by surface recombination velocities (SRVs). This

approach avoids explicit trap density definitions while maintaining physically realistic carrier lifetimes. The SRH bulk recombination rate is given by

$$R_{\mathrm{SRH}} = \frac{np - n_i^2}{\tau_p(n + n_1) + \tau_n(p + p_1)}, \tag{3.3}$$

where τ_n and τ_p are the electron and hole lifetimes, and n_1, p_1 denote carrier densities corresponding to the trap level.

To account for the experimentally observed decrease in lifetime with higher doping, the doping-dependent SRH model was activated:

$$\tau_{\mathrm{dop}}(N_A + N_D) = \tau_{\min} + \frac{\tau_{\max} - \tau_{\min}}{1 + \left(\frac{N_A + N_D}{N_{\mathrm{ref}}}\right)^{\gamma}}, \tag{3.4}$$

where $\tau_{\min}$ and $\tau_{\max}$ define the limiting lifetimes, and N_{ref} and γ determine the doping sensitivity.

At material interfaces, recombination was modeled using the surface SRH expression:

$$R_{\mathrm{surf}}^{\mathrm{SRH}} = \frac{np - n_{i,\mathrm{eff}}^2}{(n + n_1)/s_p + (p + p_1)/s_n}, \tag{3.5}$$

where s_n and s_p are the electron and hole SRVs. The SRV itself was defined as doping-dependent:

$$s = s_0 \left[1 + s_{\mathrm{ref}} \left(\frac{N_i}{N_{\mathrm{ref}}}\right)^{\gamma}\right], \tag{3.6}$$

where s_0 is the base recombination velocity and s_{ref} a scaling factor describing its variation with doping.

Finally, material-specific lifetime and SRV values were assigned to each hole-transport layer (HTL), summarized in Table 3.4. These parameters are based on experimental and computational literature [41, 69, 30].

Table 3.4: Assigned bulk carrier lifetimes and surface recombination velocities (SRV) for the different HTLs used in perovskite-based devices.

HTL	Bulk Lifetime τ (s)	SRV (cm/s)
NiO_x	1×10^{-7}	100
PEDOT:PSS	5×10^{-6}	100
PTAA	1×10^{-5}	20

3.3.4. Tunneling and Field Emission

Tunneling was modeled in direct correspondence with the theoretical framework described in Section 2.5.2. It was included in all devices to account for charge transfer across thin layers and high-field interfaces, where classical drift–diffusion transport alone is insufficient. Both trap-assisted tunneling (TAT) and band-to-band tunneling (B2BT) were explicitly activated and solved using the nonlocal WKB-based models implemented in Sentaurus Device. In both cases, tunneling currents are computed through nonlocal meshes (NLMs), which define the spatial extent of the tunneling region and link the local potential profile to the WKB transmission probability.

TAT and B2BT differ in the physical pathway through which carriers traverse the barrier. TAT proceeds via localized defect states inside the bandgap and is typically dominant in disordered or defect-rich regions (e.g., the p/i and i/n interfaces of amorphous and nanocrystalline silicon). Where specified, field-enhanced emission from charged traps (Poole–Frenkel effect) was included to account for barrier lowering under high electric fields. It dominates in disordered or defect-rich regions, such as the p/i and i/n interfaces of amorphous and nanocrystalline silicon layers. B2BT, in contrast, corresponds to direct interband tunneling between the valence and conduction bands when the junction field is sufficiently strong to thin the potential barrier. Both tunneling mechanisms are visualized in Figure 3.7.

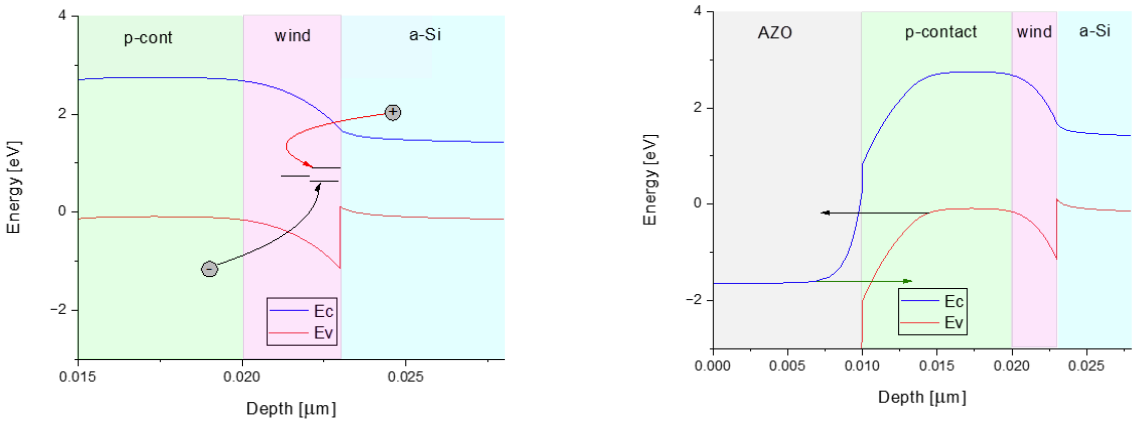

(a) Trap-assisted tunneling (TAT).

(b) Band-to-band tunneling (B2BT).

Figure 3.7: Illustration of tunneling mechanisms in thin-film photovoltaics. (a) TAT proceeds via defect-mediated tunneling through intermediate states in the bandgap. (b) B2BT represents direct tunneling across a high-field junction. Both processes are implemented through nonlocal WKB-based models (`NonLocalModel`) in Sentaurus.

In practice, tunneling was enabled at all regions where high electric fields or narrow barriers are expected to occur:

- the TCO/p-contact interface,
- the p/i absorber interfaces in a-Si:H and nc-Si:H single-junction devices,
- the TRJ in the a-Si:H/nc-Si:H tandem,
- and the perovskite/HTL and perovskite/ETL interfaces in hybrid and all-perovskite structures.

For each of these locations, a dedicated nonlocal tunneling mesh (`NonLocalModel`) was defined. This ensures that tunneling probabilities are evaluated consistently across both TAT and B2BT regimes, accounting for local variations in barrier thickness and electric field. The NLM parameters (length and permeation) were optimized per device to maintain stable convergence and physical current densities. The specific NLM definitions for each model are listed in Appendix B.

During simulation, the tunneling currents are solved self-consistently alongside drift, diffusion, and thermionic emission, allowing accurate modeling of high-field transport and recombination. This approach reproduces experimentally observed behaviors such as field-assisted recombination in the TRJ and efficient charge transfer through ultrathin perovskite transport layers.

3.3.5. Numerical Strategy

To ensure stable convergence, simulations were initialized using a short transient illumination step to establish quasi-equilibrium carrier distributions. Current–voltage sweeps were then performed quasi-stationarily in two stages: an initial coarse voltage ramp up to near the maximum power point, followed by a finer ramp toward open-circuit conditions. This two-step method prevented divergence and accurately resolved both low- and high-bias regimes.

For EQE simulations, an external wavelength sweep file was used to control the probe illumination. At each wavelength, the device response was solved under fixed bias, ensuring stable and reproducible convergence across the full spectral range.

4

Calibration

To make the simulations realistic, the models have to be calibrated against experimental measurements. The parameters taken from literature or default material models are only approximate, since properties such as defect density, Urbach energy, or mobility can vary strongly depending on deposition conditions. As a result, models may capture the overall device trends but will generally fail to reproduce the exact device performance.

The chapter is structured as followed. Section 4.1 presents the sensitivity analysis results done on the a-Si:H single junction solar cell, highlighting the dominant parameters for both transport and defect-related mechanisms. Section 4.2 describes the calibration of the single-junction a-Si:H reference cell, in which six iterative steps are required to reproduce the experimental performance. Section 4.3 then addresses the case for nc-Si:H, where the heterogeneous microstructure is modeled using a leveled approach and calibrated through five steps. Finally, the calibrated subcells provide the foundation for the a-Si:H/nc-Si:H tandem device, discussed in the last part of the chapter, Section 4.4.

4.1. Sensitivity analysis

A systematic sensitivity analysis was conducted to evaluate the effect of individual physical and material parameters on the simulated performance of the baseline a-Si:H solar cell model. Each parameter was varied independently over a defined range, while keeping all other conditions constant. The goal is to have a clear understanding of which properties influence the electrical performance of the cell.

The resulting variations were categorized using symbolic notations to indicate the magnitude of change:

- $\sim$ represents neglible effect (within ±1%),
- + or − represent moderate effects (±1% to ±5%),
- ++ or − − indicate strong effects (±5% to ±10%),
- +++ or − − − reflect very strong sensitivity (greater than ±10%).

The p-layer in particular was found to be highly sensitive to parameter changes, often resulting in solver convergence issues. If a parameter is marked with a single asterisk (*), the sweep range had to be reduced compared to the i- or n-layer range to achieve a converged solution. If marked with a double asterisk (**), even minor deviations caused simulation failure, as indicated by X in the results table.

Overall, the analysis shows that the intrinsic layer dominates the electrical response through its bandgap, carrier mobility, and trap parameters, while the p-layer is particularly critical for convergence stability and fill factor. In contrast, the n-layer and TCO properties have only minor influence on device performance, but can help in FF calibration. These observation gave a guideline into which parameters could be adjusted in the next sections.

Table 4.1: Sensitivity analysis: Bandgap, mobility, and extended DOS parameters.

Parameter	**Variation**	V_{oc}	J_{sc}	FF	η
Bandgap [eV]					
a-Si:H(p)	2.64→2.84	$\sim$	$\sim$	+++	+++
a-Si:H(i)	1.59→1.79	+++	$\sim$	+++	+++
a-Si:H(n)	2.42→2.62	$\sim$	$\sim$	$\sim$	$\sim$
Mobility [$cm^2V^{-1}s^{-1}$]					
Electron					
a-Si:H(p)	1→10	$\sim$	$\sim$	$\sim$	$\sim$
a-Si:H(i)	1→10	+	+++	+++	+++
a-Si:H(n)	1→10	$\sim$	$\sim$	$\sim$	$\sim$
Hole					
a-Si:H(p)	2→4	$\sim$	$\sim$	+	+
a-Si:H(i)	2→4	$\sim$	+	+	+
a-Si:H(n)	2→4	$\sim$	$\sim$	$\sim$	$\sim$
DOS extended states [cm^3]					
N_c					
a-Si:H(p)	2e20→2e21	$\sim$	$\sim$	$\sim$	$\sim$
a-Si:H(i)	2e20→2e21	- -	$\sim$	-	- -
a-Si:H(n)	2e20→2e21	$\sim$	$\sim$	$\sim$	$\sim$
N_v					
a-Si:H(p)	2e20→2e21	$\sim$	$\sim$	++	++
a-Si:H(i)	2e20→2e21	- -	-	- - -	- - -
a-Si:H(n)	2e20→2e21	$\sim$	$\sim$	$\sim$	$\sim$
AZO layer					
Bandgap	3.1→3.3	$\sim$	$\sim$	$\sim$	$\sim$
Electron mobility	7→17	$\sim$	$\sim$	+	+
Hole mobility	7→17	$\sim$	$\sim$	$\sim$	$\sim$
N_c	1e17→1e18	$\sim$	$\sim$	-	-
N_v	1e18→1e19	$\sim$	$\sim$	$\sim$	$\sim$

Table 4.2: Sensitivity analysis for trapped states.

Parameter	Variation	V_{oc}	J_{sc}	FF	η	Parameter	Variation	V_{oc}	J_{sc}	FF	η
Band Tail States						**Dangling Bonds**					
Donor: Urbach energy [eV]						*Donor: width [eV]*					
a-Si:H(p)*	1e-2→1.5e-2	∼	∼	- -	- -	a-Si:H(p)*	2e-1→2.5e-1	∼	∼	- - -	- - -
a-Si:H(i)	1e-3→1e-2	-	-	- -	- - -	a-Si:H(i)	1e-2→1e-1	-	-	- -	- - -
a-Si:H(n)	1e-3→1e-2	∼	∼	∼	∼	a-Si:H(n)	1e-1→1e-2	∼	∼	∼	∼
Acceptor: Urbach energy [eV]						*Acceptor: width [eV]*					
a-Si:H(p)	1e-3→1e-2	∼	∼	∼	∼	a-Si:H(p)*	2e-1→2.5e-1	∼	∼	+	+
a-Si:H(i)	1e-3→1e-2	-	-	- -	- - -	a-Si:H(i)	1e-2→1e-1	-	-	- -	- - -
a-Si:H(n)	1e-3→1e-2	∼	∼	∼	∼	a-Si:H(n)	1e-1→1e-2	∼	∼	∼	∼
Donor: N_t [eV^{-1}cm^{-3}]						*Donor: N_t [eV^{-1}cm^{-3}]*					
a-Si:H(p)	1e20→1e21	∼	∼	- -	- -	a-Si:H(p)**	1e16→1e17	X	X	X	X
a-Si:H(i)	1e20→1e21	∼	∼	∼	∼	a-Si:H(i)	1e20→1e21	- - -	- - -	- - -	- - -
a-Si:H(n)	1e20→1e21	∼	∼	∼	∼	a-Si:H(n)	1e20→1e21	∼	∼	∼	∼
Acceptor: N_t [eV^{-1}cm^{-3}]						*Acceptor: N_t [eV^{-1}cm^{-3}]*					
a-Si:H(p)	1e20→1e21	∼	∼	∼	∼	a-Si:H(p)	1e16→1e17	∼	∼	∼	∼
a-Si:H(i)	1e20→1e21	∼	∼	∼	∼	a-Si:H(i)	1e20→1e21	∼	∼	-	-
a-Si:H(n)	1e20→1e21	∼	∼	∼	∼	a-Si:H(n)	1e20→1e21	∼	∼	∼	∼
Donor: electron capture cross section [cm^2]						*Donor: electron capture cross section [cm^2]*					
a-Si:H(p)	7e-16→7e-14	∼	∼	∼	∼	a-Si:H(p)	7e-15→7e-14	∼	∼	+++	+++
a-Si:H(i)	7e-16→7e-14	∼	-	∼	-	a-Si:H(i)	7e-15→7e-14	-	-	-	- - -
a-Si:H(n)	7e-16→7e-14	∼	∼	∼	∼	a-Si:H(n)	7e-15→7e-14	∼	∼	∼	∼
Donor: hole capture cross section [cm^2]						*Donor: hole capture cross section [cm^2]*					
a-Si:H(p)	7e-16→7e-14	∼	∼	∼	∼	a-Si:H(p)**	7e-15→7e-14	X	X	X	X
a-Si:H(i)	7e-16→7e-14	∼	∼	∼	∼	a-Si:H(i)	7e-15→7e-14	-	-	-	- -
a-Si:H(n)	7e-16→7e-14	∼	∼	∼	∼	a-Si:H(n)	7e-15→7e-14	∼	∼	∼	∼
Acceptor: electron capture cross section [cm^2]						*Acceptor: electron capture cross section [cm^2]*					
a-Si:H(p)	7e-16→7e-14	∼	∼	∼	∼	a-Si:H(p)	7e-15→7e-14	∼	∼	+++	+++
a-Si:H(i)	7e-16→7e-14	∼	∼	∼	∼	a-Si:H(i)	7e-15→7e-14	+	+	+	+++
a-Si:H(n)	7e-16→7e-14	∼	∼	∼	∼	a-Si:H(n)	7e-15→7e-14	∼	∼	∼	∼
Acceptor: hole capture cross section [cm^2]						*Acceptor: hole capture cross section [cm^2]*					
a-Si:H(p)	7e-16→7e-14	∼	∼	∼	∼	a-Si:H(p)	7e-15→7e-14	∼	∼	∼	∼
a-Si:H(i)	7e-16→7e-14	∼	-	∼	-	a-Si:H(i)	7e-15→7e-14	∼	-	∼	-
a-Si:H(n)	7e-16→7e-14	∼	∼	∼	∼	a-Si:H(n)	7e-15→7e-14	∼	∼	∼	∼

4.2. a-Si:H solar cell calibration

The starting point of the calibration model of the a-Si:H solar cell was by a baseline model obtained in Sentaurus, for which the device parameters can be found in appendix A. For the calibration of the a-Si single junction solar cell six main iterations of the baseline model where needed, which are all discussed below.

4.2.1. Starting Point

The baseline electrical model provided the first set of simulated J–V and EQE characteristics. Figure 4.1 compares these results with the experimental measurements of the solar cell, while Table 4.3 summarizes the corresponding performance metrics. As can be seen, the simulated $J_{\mathrm{sc,EQE}}$ shows quite good agreement with experiment, whereas the V_{oc} and FF are underestimated. This results in a simulated efficiency almost 30% lower than the measured value as starting point.

Table 4.3: Performance comparison between baseline simulation and experimental measurement

Metric	Experimental	Baseline Simulation
V_{oc} [V]	0.855	0.754
$J_{\mathrm{sc,EQE}}$ [mA/cm^2]	16.01	15.48
Fill Factor [%]	71.67	59.13
Efficiency η_{EQE} [%]	9.81	6.90

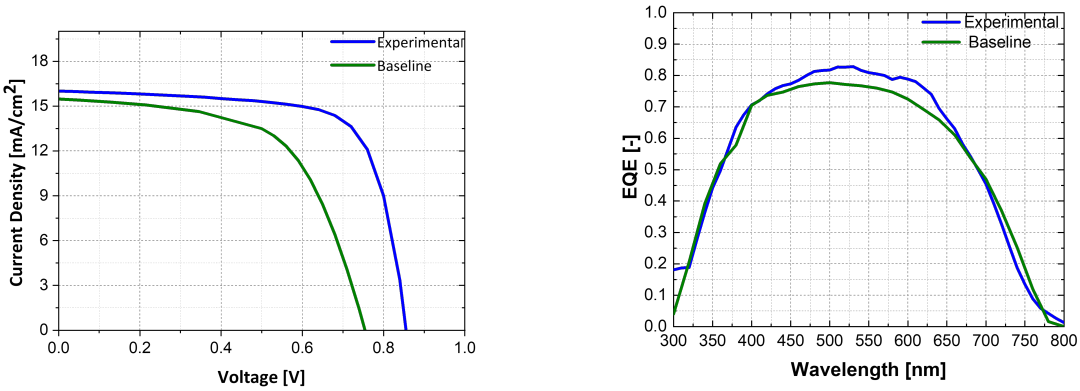

(a) Current density–voltage (J–V) characteristics

(b) External quantum efficiency (EQE) comparison

Figure 4.1: Baseline simulation (green) vs. experiment (blue): (a) current density–voltage (J–V) curve; (b) external quantum efficiency (EQE).

4.2.2. First Calibration Step: Electron Affinity and Doping Adjustment

Initially, in the baseline model, the *p*++ and *p*+ layers used were both assigned high doping concentrations of 1×10^{20} cm^{-3} and 2×10^{20} cm^{-3}, respectively. However, by reducing the total Gaussian trap density, it was possible to achieve effective doping levels of 1×10^{20} cm^{-3} and 5×10^{19} cm^{-3}, respectively, while maintaining simulation stability and convergence. While explicit doping concentrations for both p-type and n-type nc-SiO$_x$:H are rarely reported in experimental studies, simulation work on related a-Si:H thin-film solar cells typically employs doping levels in a similar range [10, 38]. This adjustment was not to achieve better agreement with the experimental curves, but to resemble doping densities according to the experimental cell.

Furthermore, since the p and n-type layers in the device consist of nanocrystalline silicon oxide (nc-SiO$_x$), the electron affinity χ of these layers was not set to a fixed value but instead interpolated between the known values of nc-Si and silicon dioxide (SiO$_2$). This approach reflects the mixed-phase nature of nc-SiO$_x$:H, whose optoelectronic properties vary continuously with oxygen content [45]. Assuming a linear dependence on the effective bandgap, we used $\chi_{\mathrm{nc-Si}} = 4.05$ eV and $\chi_{\mathrm{SiO_2}} = 0.90$ eV as reference points. For an nc-SiO$_x$ p-type layer with a bandgap of 2.84 eV, the interpolated electron

affinity was $\chi \approx 3.36$–3.39 eV depending on the assumed bandgap of nc-Si (1.12 or 1.20 eV). Similarly, for the n-type nc-SiO$_x$ layer with a bandgap of 2.42 eV, χ was calculated to be in the range of 3.53–3.56 eV.

As shown in Fig. 4.4, the transition from the baseline simulation (green) to the first calibration step (orange) leaves the open-circuit voltage V_{oc} essentially unchanged, while the short-circuit current J_{sc} only shifts up slightly. However, the knee of the J–V curve improves, reflecting a clear increase in the fill factor. The EQE comparison in Figure 4.1(b) shows only a slight upward shift from the baseline, indicating a modest enhancement in carrier collection across the spectrum.

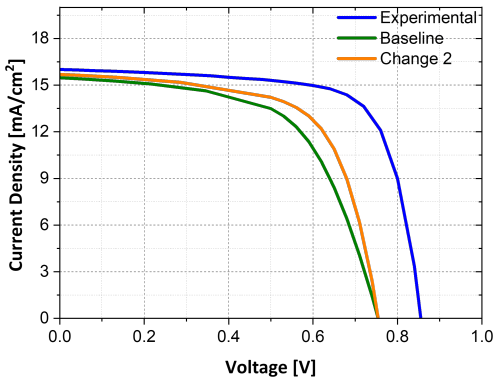

(a) Current density–voltage (J–V) characteristics

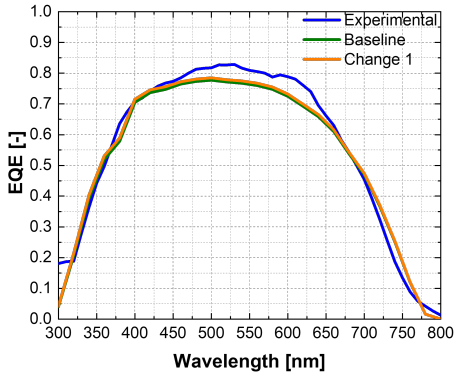

(b) External quantum efficiency (EQE) comparison

Figure 4.2: Comparison of experimental data (blue) with simulation results for the baseline and Change 1: (a) current density–voltage (J–V) curve; (b) external quantum efficiency (EQE).

4.2.3. Second Calibration Step: Urbach Energy Fitting

The absorption coefficient α near the band edge follows the empirical Urbach rule [46]:

$$\alpha(E) = \alpha_0 \exp\left(\frac{E - E_g}{E_U}\right), \tag{4.1}$$

where E is the photon energy, E_g is the optical bandgap, α_0 is a material-dependent prefactor, and E_U is the Urbach energy. By plotting $\ln(\alpha)$ versus E, the Urbach energy can be extracted from the inverse slope of the exponential tail region.

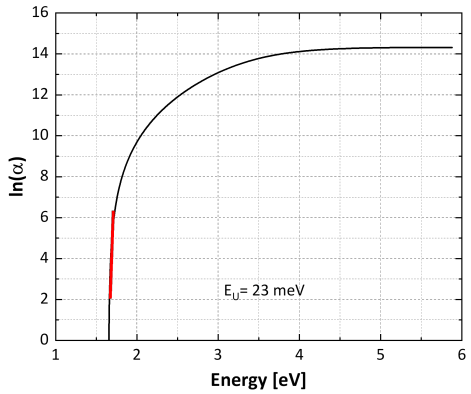

Figure 4.3: Urbach energy fitting from the experimental absorption spectrum.

Fitting the experimental absorption spectrum of the intrinsic a-Si:H absorber yielded an Urbach energy

of approximately $E_U \approx 23$ meV as can be seen in Figure 4.3. To account for the asymmetry between conduction and valence band tails, different Urbach energies were assigned to donor- and acceptor-type tail states: $E_U = 30$ meV for donor-like states and $E_U = 22$ meV for acceptor-like states, similar to [13].

The original baseline simulation assumed an unrealistically sharp band edge with $E_U = 4$ meV, leading to significantly narrower tail states. Updating to more realistic Urbach energies increased the spatial and energetic extent of the tail states, which in turn caused excessive carrier trapping and non-converging solutions in the numerical solver.

To stabilize the simulation and avoid solver failure, the density of tail states had to be reduced. Specifically, the donor and acceptor trap state concentrations were lowered from 1.88×10^{21} and 1.82×10^{21} cm^{-3}eV^{-1}, respectively, to 0.2×10^{21} cm^{-3}eV^{-1} [11, 55]. This reduction limits the recombination rate and charge localization associated with the extended tails, helping to maintain charge transport and convergence during DC and transient sweeps.

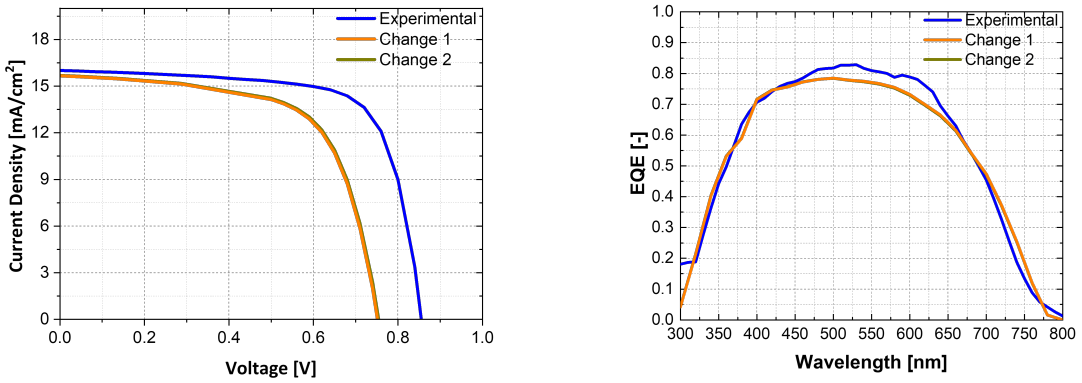

(a) Current density–voltage (J–V) characteristics

(b) External quantum efficiency (EQE) comparison

Figure 4.4: Comparison of experimental data (blue) with simulation results after the first (Change 1) and second (Change 2) calibration steps: (a) current density–voltage (J–V) curve; (b) external quantum efficiency (EQE).

4.2.4. Third Calibration Step: Dangling Bond Concentration Fitting

After adjusting the Urbach energy parameters, the third calibration step involved tuning the dangling bond defect density in the intrinsic layer to improve agreement in J_{sc} between simulation and experiment.

In the previous configuration (Change 2), a high DB concentration of 1.38×10^{16} cm^{-3} led to excessive recombination losses and an underestimated J_{sc}. Reducing the DB density to 0.78×10^{16} cm^{-3} (Change 3) significantly improved carrier collection, resulting in better alignment of the simulated and experimental photocurrents.

This adjustment also led to an improved EQE response, particularly in the wavelength range of 400–650 nm, where bulk recombination plays a dominant role. The updated simulation, shown in Figure 4.5 shows both mathching current output with the experimental data and closer EQE matching to the experimental device.

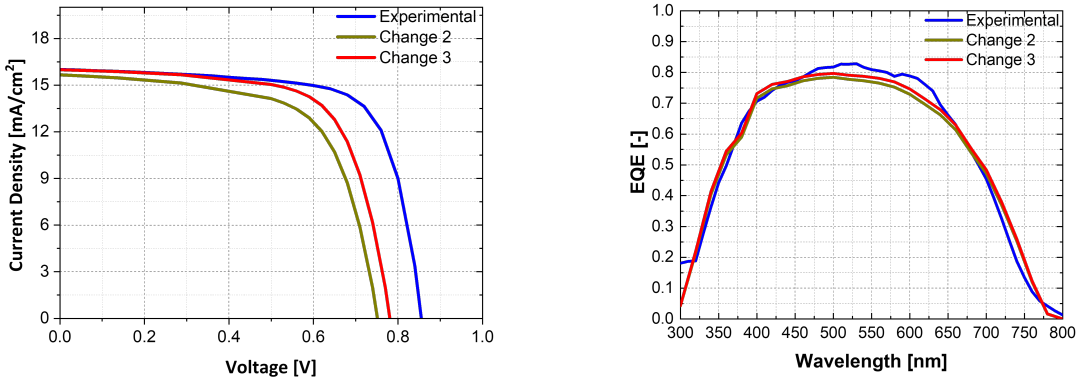

(a) Current density–voltage (J–V) characteristics

(b) External quantum efficiency (EQE) comparison

Figure 4.5: Effect of reducing the dangling bond concentration in the intrinsic layer. (a) Current density–voltage (J–V) curve; (b) external quantum efficiency (EQE). Experimental data are shown in blue; Change 2 and Change 3 simulations are shown in olive and red, respectively.

4.2.5. Fourth Calibration Step: Intrinsic Layer DOS Adjustment

The fourth calibration step focused on increasing the simulated open-circuit voltage V_{oc} by reducing the effective density of states in the intrinsic absorber. The conduction and valence band densities, N_c and N_v, were each decreased from 2×10^{20} to 1×10^{20} cm^{-3}, similar to values shown in [68].

This reduction lowers the intrinsic carrier concentration, which decreases the SRH recombination rate in the intrinsic layer. Since the SRH recombination rate directly influences the dark saturation current, a lower recombination rate leads to a smaller saturation current and, consequently, a higher V_{oc}.

The simulated JV curve shows a clear increase in V_{oc} compared to the previous configuration (Change 3), while maintaining the calibrated J_{sc} and overall EQE shape. The result are shown in Figure 4.6.

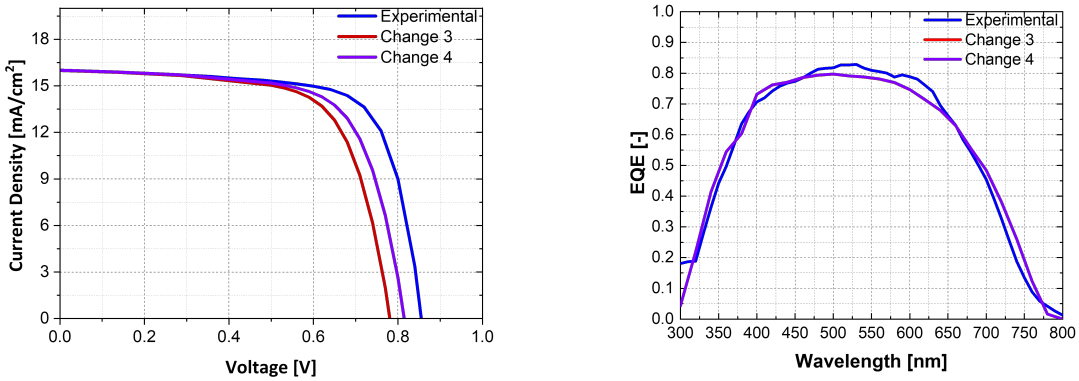

(a) Current density–voltage (J–V) characteristics

(b) External quantum efficiency (EQE)

Figure 4.6: Effect of reducing the effective density of states N_c and N_v in the intrinsic layer from 2×10^{20} to 1×10^{20} cm^{-3}. (a) Current density–voltage (J–V) curve; (b) external quantum efficiency (EQE). Experimental data are shown in blue; Change 3 and Change 4 simulations are shown in red and magenta, respectively.

4.2.6. Fifth Calibration Step: Bandgap Increase to Match V_{oc}

After adjusting the density of states in the intrinsic layer, the simulated V_{oc} was still lower than the experimental value. In the fifth calibration step, the optical bandgap E_g of the intrinsic absorber was increased from 1.59 eV to 1.63 eV to further improve V_{oc}.

An increase in bandgap widens the energy separation between the conduction and valence bands,

which reduces the intrinsic carrier concentration and further suppresses recombination. This leads to a higher quasi-Fermi level splitting under illumination and thus a higher open-circuit voltage.

The result of this adjustment (Change 5) is a match with the experimental V_{oc}, without a significant change to the EQE spectrum. As expected, increasing the bandgap slightly reduces absorption at longer wavelengths, which can lead to a drop in EQE beyond 650 nm. However, in this case the change was minimal and hardly visible in the EQE spectrum, indicating that the loss in photogenerated current was negligible.

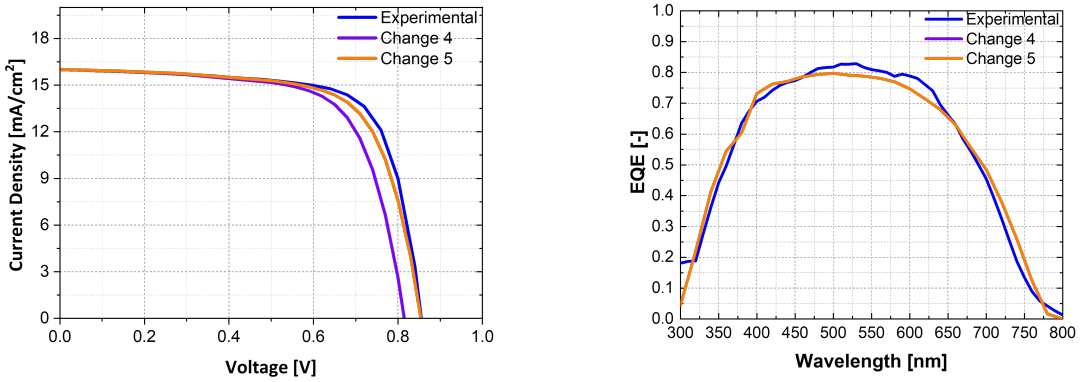

(a) Current density–voltage (J–V) characteristics

(b) External quantum efficiency (EQE)

Figure 4.7: Effect of increasing the intrinsic layer bandgap from 1.59 eV to 1.63 eV. (a) Current density–voltage (J–V) curve; (b) external quantum efficiency (EQE). Experimental data are shown in blue; Change 4 and Change 5 simulations are shown in violet and orange, respectively.

4.2.7. Sixth Calibration Step: AZO Electron Mobility and Fill Factor Optimization

The sixth and final calibration step targeted the improvement of FF and overall device efficiency. In the previous configuration (Change 5), both quantities remained below experimental values despite successful fitting of V_{oc} and J_{sc}.

To resolve this, the electron mobility μ_n in the AZO front contact was increased from 7.73 to 20 cm^2/Vs [74]. This change reduced the series resistance and improved charge collection near the maximum power point.

As a result, shown in Figure 4.8, the simulated JV curve shows a steeper slope near the knee and better agreement with the experimental curve. The EQE response remained unchanged, confirming that the modification had no effect on optical generation. The corresponding improvement over all the calibrations is summarized in Table 4.4.

Table 4.4: Performance comparison between experimental measurement and final simulation (Change 6)

Metric	Experimental	Final Simulation
V_{oc} [V]	0.86	0.85
$J_{sc,EQE}$ [mA/cm^2]	16.01	16.02
Fill Factor [%]	71.67	71.67
Efficiency η_{EQE} [%]	9.81	9.81

The six calibration steps above define the final a-Si:H single-junction model used throughout this chapter. For completeness, Fig. 4.9 shows the equilibrium band diagram of the calibrated stack. The band alignment illustrates the built-in electric field across the intrinsic absorber that drives carrier collection and the band offsets at the nc-SiO$_x$:H/*i*-a-Si:H interfaces that influence injection barriers.

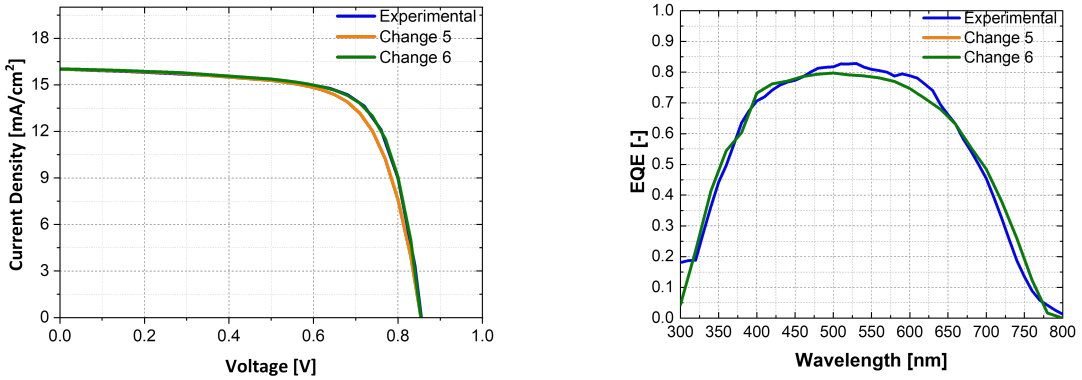

(a) Current density–voltage (J–V) characteristics.

(b) External quantum efficiency (EQE).

Figure 4.8: Effect of increasing AZO electron mobility from 7.73 to 20 cm^2/Vs. Experimental data shown in blue; simulated curves for Change 5 and Change 6 shown in orange and green, respectively.

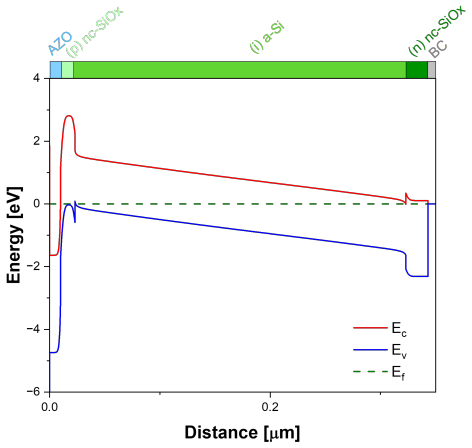

Figure 4.9: Equilibrium band diagram of the calibrated a-Si:H single-junction device (AZO / *p*-nc-SiO$_x$:H / *i*-a-Si:H / *n*-nc-SiO$_x$:H / back contact). Red: E_c; blue: E_v; green dashed: E_f.

4.2.8. Post-Calibration Sensitivity Analysis: Effect of E_U and Dangling Bonds

To evaluate the sensitivity of the final simulation, a two-dimensional parameter sweep was conducted by varying the Urbach energy of the tail states and the total dangling bond concentration. All other parameters were fixed to the calibrated values. The results are shown in Figure 4.13, with the red contour lines highlighting the combinations that reproduce the experimental values of $J_{\text{sc}} = 16.01$ mA/cm^2 and $V_{\text{oc}} = 0.855$ V. In the sweep shown in Figure 4.13, the x-axis represents paired values of the Urbach energies for the acceptor-like and donor-like tail states, denoted as $E_{U,\text{acc}}$ and $E_{U,\text{donor}}$, respectively. Rather than varying these parameters independently, a series of representative pairings was used to reflect realistic asymmetries in the defect distributions. Specifically, $E_{U,\text{acc}}$ was varied from 0.010 to 0.070 eV, and $E_{U,\text{donor}}$ from 0.018 to 0.078 eV. Each tick on the x-axis corresponds to a unique pair of values—for example, the first tick represents $E_{U,\text{acc}} = 0.010$ eV and $E_{U,\text{donor}} = 0.018$ eV, while the last corresponds to $0.070/0.078$ eV. This approach captures the coupled effect of both distributions on recombination and carrier transport.

The sweep reveals that J_{sc} remains relatively stable across a broad parameter space, indicating that moderate changes in defect-related parameters do not significantly impact carrier collection. This is because tail states near the band edges are less effective recombination centers and photogenerated carriers are still efficiently extracted unless recombination becomes too dominant.

In contrast, V_{oc} is far more sensitive to both $E_{U,\text{acc}}$ and dangling bond concentration. Increasing ei-

ther parameter enhances Shockley-Read-Hall recombination, particularly due to midgap states, which strongly impact quasi-Fermi level splitting and raise the dark saturation current. Even small deviations from the optimal region lead to a noticeable drop in V_{oc}.

Eventhough the tail state density used in the simulation ($\sim 10^{20}\,\text{cm}^{-3}\text{eV}^{-1}$) is several orders of magnitude higher than the dangling bond concentration ($\sim 10^{16}\,\text{cm}^{-3}\text{eV}^{-1}$), the midgap position of the DBs makes them significantly more recombination-active. This explains why V_{oc} is highly sensitive to relatively small changes in DB density, while J_{sc} is not.

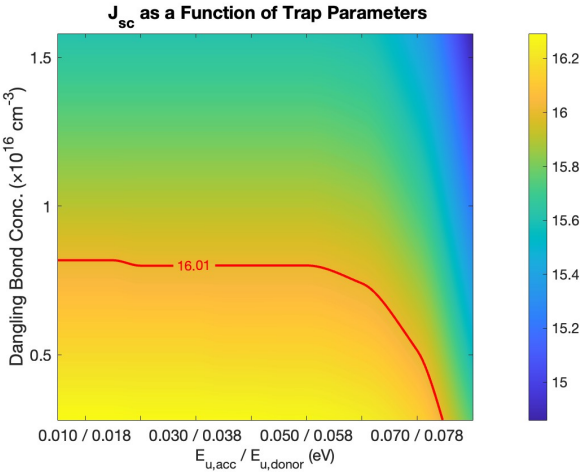

(a) J_{sc} as a function of $E_{U,\text{acc}}$ / $E_{U,\text{donor}}$ and DB concentration.

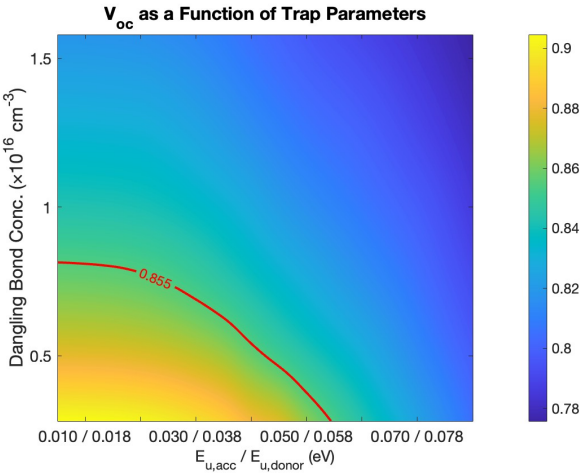

(b) V_{oc} as a function of $E_{U,\text{acc}}$ / $E_{U,\text{donor}}$ and DB concentration.

Figure 4.10: Contour plots showing the sensitivity of J_{sc} and V_{oc} to changes in the Urbach energy of the tail states and total dangling bond concentration. The red lines highlight parameter combinations that yield the experimentally calibrated values.

4.3. nc-Si modelling calibration

The numerical modeling of nc-Si:H is complicated by its heterogeneous microstructure. The material consists of silicon nanocrystals embedded in an amorphous matrix, along with grain boundaries and a gradual variation in structure along the growth direction. These inhomogeneities lead to spatial variations in optical and electronic properties, making it difficult to assign consistent material parameters based solely on experimental measurements [42].

Two general approaches are used to model nc-Si:H in device simulations. One approach explicitly defines separate phases—crystalline, amorphous, and grain boundaries—each with distinct physical properties. The other approach treats the absorber as a single, homogeneous layer with effective averaged properties. As [42] points out, separating the phases does not necessarily improve accuracy, particularly when the nanocrystals are small and conventional transport models become less valid.

In this work, a layered approach is used. The intrinsic nc-Si:H absorber is divided into three layers (ncSi1, ncSi2, ncSi3), with crystallinity increasing from the substrate toward the surface. This reflects the structural gradient observed in experimentally grown films, such as those studied by Sancho-Parramon et al. [50]. Using Raman spectroscopy and optical techniques, they demonstrated that the crystalline volume fraction increases with depth, with a mixture of small (2–3 nm) and large (8–20 nm) grains forming a vertically inhomogeneous profile. Their results also showed that both the Urbach energy and the defect density tend to increase with crystallinity, due to grain-boundary disorder, which becomes more present as large crystallites form. Based on these observations, the simulation assigns higher Urbach energy and defect density to the deeper layers (which are more crystalline), while the top layers (with lower crystalline content) are modeled with lower disorder. This captures the vertical variation in optoelectronic quality without requiring full microscopic resolution.

4.3.1. Starting point

The initial material parameters for the intrinsic nc-Si:H absorber are based on values from [13, 42], which provides band structure, mobility, and density-of-states parameters for nanocrystalline silicon. Together, these references served as a physically consistent starting point for the nc-Si:H device simulation, which can be seen in Table 4.5. For the p and n layer, which were similar to the a-Si:H solar cell, the values were kept the same as in the final calubration of the a-Si:H solar cell.

It was further found that increasing the doping concentration of the n-layer from 2×10^{19} to 4×10^{19} cm^{-3} was necessary to achieve an sharper JV curve knee instead of an S-curve.

In contrast to the a-Si:H reference cell, which uses a single-layer AZO front contact, the nc-Si:H cell is modeled with a bilayer TCO stack consisting of hydrogenated indium oxide and intrinsic ZnO, as mentioned in section 3.1.1. This IOH/ZnO configuration allows decoupling of the optical and electrical roles of the front contact: the ZnO layer ensures high optical transparency, while the IOH layer provides high lateral conductivity [49]. Experimental measurements report that IOH exhibits significantly higher electron mobility (up to 122 cm^2/Vs) compared to ZnO (approximately 5.4 cm^2/Vs), supporting its function as the primary charge transport layer [49]. For the back i-ZnO layer in the micromorph tandem structure, the electrical parameters reported by Frisk et al. [15] were adopted, as this layer primarily serves as an electron transport and contact layer. These parameters include a donor doping concentration of 1×10^{17} cm^{-3} and an electron mobility of 100 cm^2/Vs.

The effective density of states at the band edges (N_c and N_v) for IOH and ZnO were not explicitly reported in the experimental literature. Therefore, values were assumed based on theoretical estimates and data for comparable wide-bandgap n-type semiconductors such as In_2O_3 and ZnO. Using typical effective masses ($m^* \approx 0.3\,m_0$) and standard expressions for density of states at room temperature, N_c and N_v were estimated to be in the range of 10^{18}–10^{19} cm^{-3} [25, 31]. The values used for both the top and bottom supporting layers can be found at the end of this chapter, in Table 4.9

The above mentioned value were implemented in the Sentaurus model giving the characteristics as shown in Figure 4.11. The simulated cell reproduces the overall trend of the experimental data but underestimates both the current density and EQE. This indicates incomplete carrier collection and suggests that further calibration of defect and transport parameters is needed.

Table 4.5: Simulation parameters for the intrinsic nc-Si:H i-layer, using Sentaurus notation. Values are directly applied in the three effective sublayers (ncSi1, ncSi2, ncSi3).

Parameter	Simulation values (ncSi1 / ncSi2 / ncSi3)
Band structure	
Band gap E_g (eV)	$1.12/1.15/1.20$
Electron affinity (eV)	4.05
Dielectric constant ε_r	11.9
Electron mobility μ_n (cm^2/Vs)	$10/15/20$
Hole mobility μ_p (cm^2/Vs)	$4/5/6$
DOS N_c (cm^{-3}eV^{-1})	4.8×10^{19}
DOS N_v (cm^{-3}eV^{-1})	2.4×10^{20}
Valence band tail states	
Tail width E_U (eV)	$0.027/0.031/0.035$
Trap density N_t (cm^{-3}eV^{-1})	$2.8/4.8/7.8 \times 10^{19}$
Capture cross section σ_p^0 (cm^2)	5.0×10^{-16}
Capture cross section σ_n^+ (cm^2)	5.0×10^{-15}
Conduction band tail states	
Tail width E_U (eV)	$0.027/0.031/0.035$
Trap density N_t (cm^{-3}eV^{-1})	$7.6/9.6/11.6 \times 10^{19}$
Capture cross section σ_n^0 (cm^2)	5.0×10^{-16}
Capture cross section σ_p^- (cm^2)	5.0×10^{-15}
Dangling bond states	
Gaussian width U (eV)	0.144
Trap density N_t (cm^{-3})	$4/6/8 \times 10^{15}$
Capture cross section σ_p^0 (cm^2)	3.0×10^{-16}
Capture cross section σ_n^0 (cm^2)	3.0×10^{-16}
Capture cross section σ_n^- (cm^2)	3.0×10^{-15}
Capture cross section σ_p^+ (cm^2)	3.0×10^{-15}

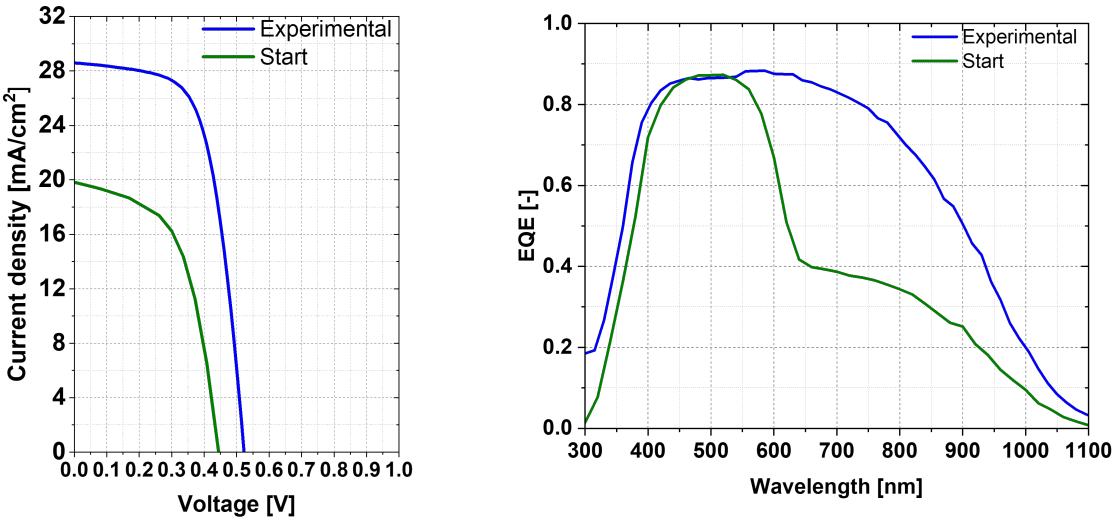

(a) Current density–voltage (J–V) characteristics.

(b) External quantum efficiency (EQE).

Figure 4.11: Simulated electrical and optical performance of the baseline nc-Si:H solar cell, based on parameters from Tables 4.5 and 4.9.

4.3.2. First calibration step: capture cross sections

As a first step in the electrical calibration of the nc-Si:H absorber, the capture cross sections of all three intrinsic sublayers (ncSi1, ncSi2, and ncSi3) were adjusted uniformly. The initial simulation results of the previous section show that the model significantly underestimated all performance metrices, particularly J_{sc} and FF. This pointed to too high recombination rates across the i-layer.

To address this, the capture cross sections for all trap types were reduced by approximately one order of magnitude (from for example 5×10^{-15} to 5×10^{-16}) , while keeping the DOS fixed. This directly decreased recombination activity. The resulting changes improved the EQE spectral shape and the curvature of the JV curve. The change is shown by the orange curves in Fig. 4.12.

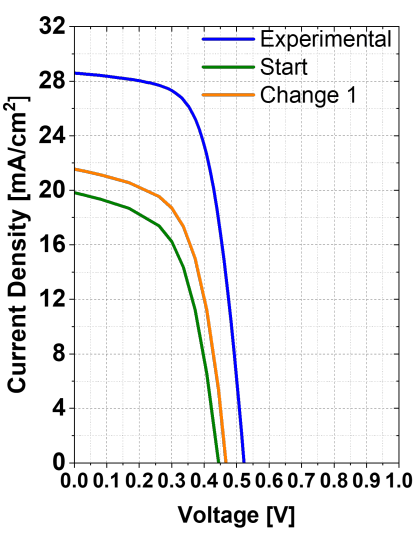

(a) Current density–voltage (J–V) characteristics.

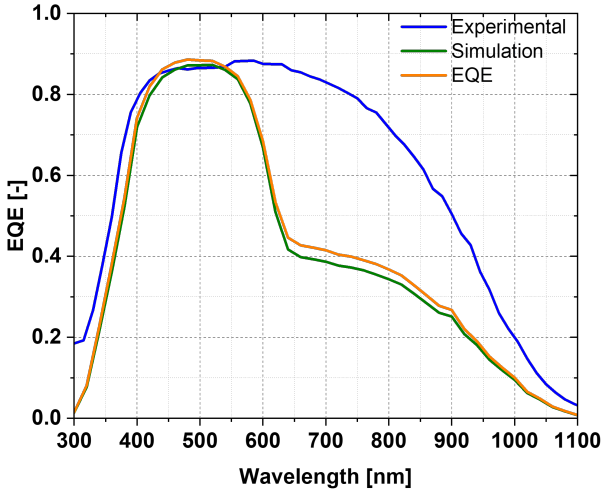

(b) EQE spectra. Reduced cross sections lead to stronger recombination, particularly at long wavelengths.

Figure 4.12: Effect of tuning capture cross sections in the nc-Si:H absorber. Blue: initial uncalibrated model; green: doping-adjusted model; orange: capture cross section calibrated.

4.3.3. Second Calibration Step: Urbach Energy vs Dangling Bond Trade-off

To further refine the electrical behavior of the nc-Si:H absorber, a 2D parameter sweep was performed varying the Urbach energy E_u and the dangling bond concentration N_{DB}, similar to the sweep done in Section 4.2.8. Here the acceptor and donor Urbach energy are kept equal. As shown in Fig. **??**, both J_{sc} and V_{oc} exhibit strong sensitivity to these defect-related parameters. The red line in the figure indicates the experimental value that is the goal. In general, increasing either E_u or N_{DB} enhances recombination, reducing both current collection and open-circuit voltage.

A region was identified where moderate values of both parameters yielded satisfactory device performance. Based on this, three depth-dependent combinations were selected for the sublayers ncSi1, ncSi2, and ncSi3:

$$N_{\text{DB}} = (1.0,\ 1.25,\ 1.5) \times 10^{14}\ \text{cm}^{-3}, \quad E_u = (0.031,\ 0.034,\ 0.039)\ \text{eV}$$

The chosen values were then implemented by modifying the density of states in all three regions of the intrinsic absorber. Figure 4.14 shows the changes made in the middle sublayer (ncSi2) as an example. The tail state widths (E_u) were increased symmetrically in the valence and conduction bands, while the peak density of the Gaussian midgap defect distribution (N_{DB}) was reduced. Equivalent modifications were applied in ncSi1 and ncSi3 according to the parameter sweep results.

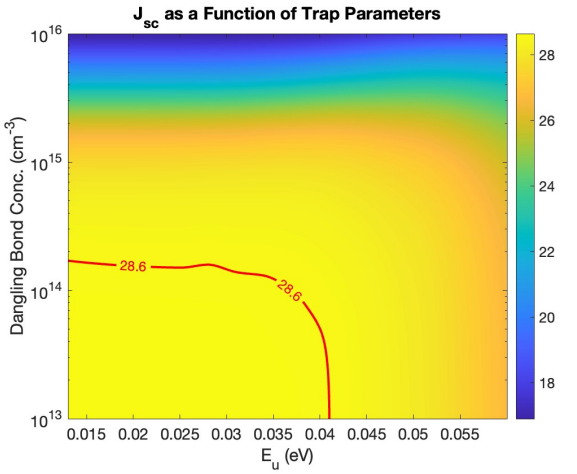

(a) J_{sc} as a function of $E_{U,\text{acc}}$ / $E_{U,\text{donor}}$ and DB concentration.

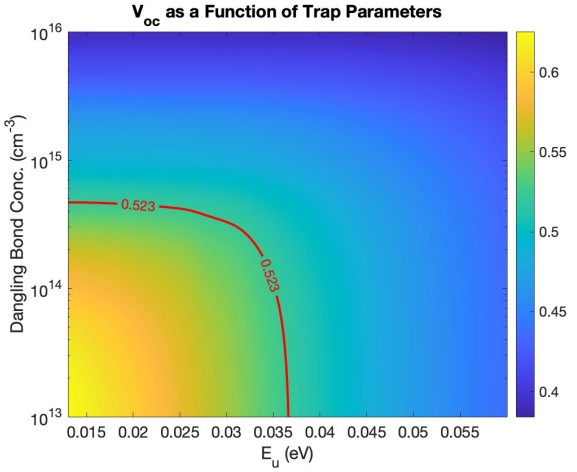

(b) V_{oc} as a function of $E_{U,\text{acc}}$ / $E_{U,\text{donor}}$ and DB concentration.

Figure 4.13: Contour plots showing the sensitivity of J_{sc} and V_{oc} to changes in the Urbach energy of the tail states and total dangling bond concentration. The red lines highlight parameter combinations that yield the experimentally calibrated values.

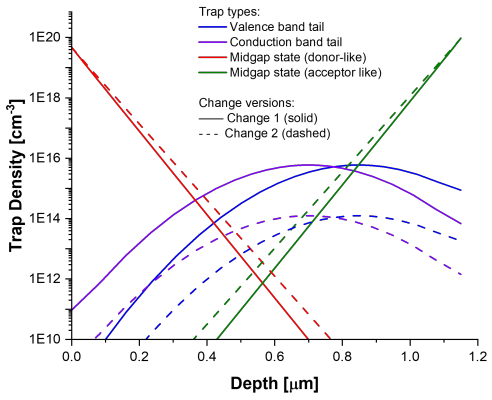

Figure 4.14: Trap density distributions in the middle sublayer ncSi2 before (solid) and after (dashed) calibration. Tail state broadening and dangling bond reduction were applied to all three intrinsic regions based on the sweep.

The impact of these trap modifications is shown in Fig. 4.15. The updated configuration (red) success-

fully restores the long-wavelength EQE that had been suppressed in earlier steps, due to the presence of too many recombination centres. The JV curve shows improvement in both V_{oc} and FF, leading to better agreement with the experimental shape and performance metrics.

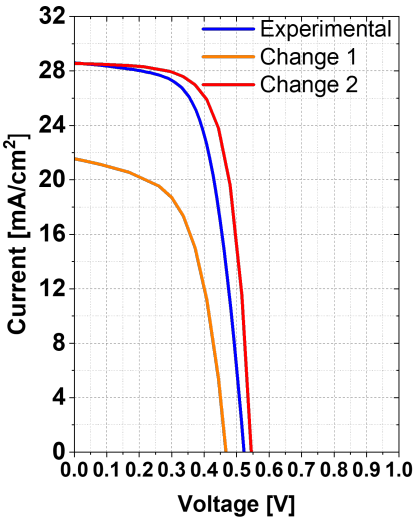

(a) Current density–voltage (J–V) characteristics.

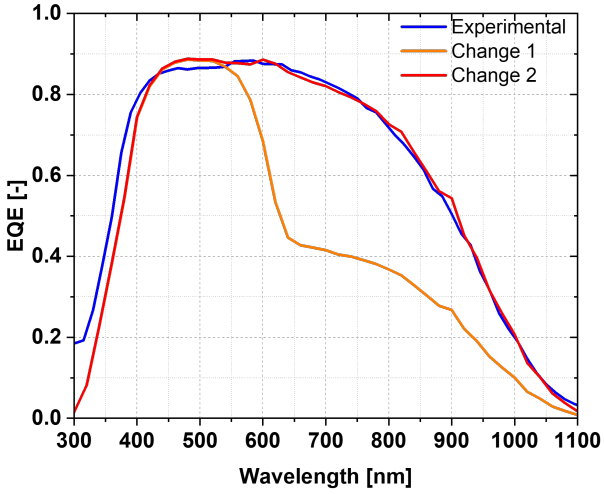

(b) External quantum efficiency (EQE) spectra. The red curve shows enhanced long-wavelength response and more realistic recombination behavior after defect calibration.

Figure 4.15: Effect of tuning the Urbach energy and dangling bond concentration in the nc-Si:H absorber layer. Blue: initial uncalibrated model; orange: capture cross section tuning; red: defect-calibrated model.

4.3.4. Third Calibration Step: Effective Density of States Adjustment

In an attempt align the simulated JV curve more closely with the experimental shape at the Voc, the effective density of states (N_c, N_v) in the intrinsic nc-Si:H absorber was increased. The original values of $N_c = 4.8 \times 10^{19}$ cm^{-3} and $N_v = 2.4 \times 10^{20}$ cm^{-3} were raised to 8.0×10^{19} cm^{-3} and 6.0×10^{20} cm^{-3}, respectively.

This change affects the carrier occupation statistics and recombination dynamics. Specifically, the increased DOS shifts the position of the intrinsic Fermi level and raises the equilibrium carrier concentration, which in turn increases recombination under illumination. As a result, the separation of the quasi-Fermi levels is reduced, leading to a slight drop in V_{oc}, visible in the purple curve of Fig. 4.16. The EQE spectrum is largely unaffected, indicating that the change primarily impacts the electrical characteristics, not the optical collection.

4.3.5. Fourth Calibration Step: Carrier Mobility Tuning

In the next calibration step, the focus was on recovering the slight reduction in J_{sc} caused by the previous increase in density of states. To improve carrier collection, the electron and hole mobilities in the intrinsic nc-Si:H sublayers were increased across all three depth regions.

The mobility values were updated as follows:

$$\mu_n = (20,\ 25,\ 30)\ \text{cm}^2/\text{Vs}, \quad \mu_p = (3,\ 5,\ 6)\ \text{cm}^2/\text{Vs}$$

for ncSi1, ncSi2, and ncSi3 respectively. This change with the earlier values of $(10, 15, 20)$ and $(4, 5, 6)$ for μ_n and μ_p, which were sufficient in the initial calibration but proved slightly limiting after DOS tuning.

As shown in Figure 4.17, the adjusted mobility improves charge transport and carrier extraction, leading to a higher J_{sc} and a slight increase in FF. The EQE curve confirms this improvement, with the green curve showing a slight rise in the spectral response near the peak, indicating more efficient carrier collection across the absorber depth.

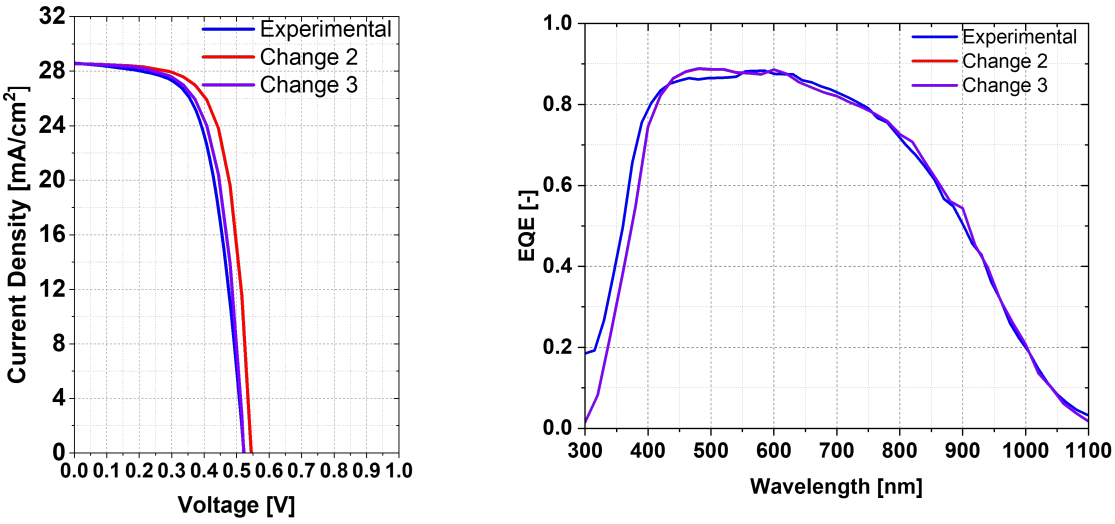

(a) Current density–voltage (J–V) characteristics.

(b) External quantum efficiency (EQE).

Figure 4.16: Effect of increasing the effective density of states in the intrinsic nc-Si:H absorber layer. Blue: initial uncalibrated model; red: defect-calibrated model; purple: final DOS-adjusted model.

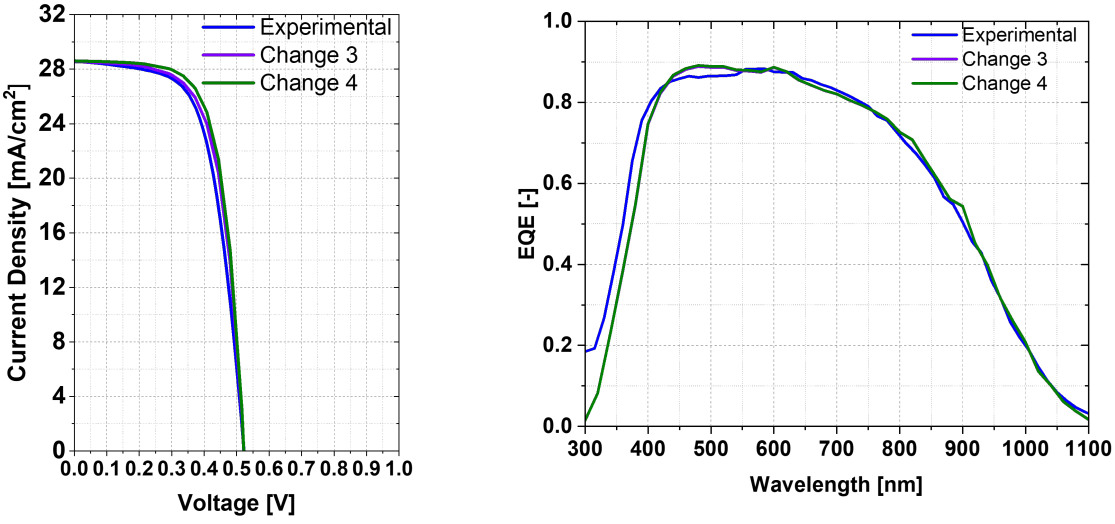

(a) Current density–voltage (J–V) characteristics.

(b) External quantum efficiency (EQE).

Figure 4.17: Effect of increasing carrier mobility in the intrinsic nc-Si:H absorber layer. Blue: initial model; purple: defect- and DOS-adjusted model; green: final model with mobility enhancement.

4.3.6. Fifth Calibration Step: Tuning of n-Layer Electron Affinity

The final calibration step focused on adjusting the FF to match the experimentally observed value. The simulated FF had remained slightly too high in previous steps, reaching up to 67.9%. To reduce it to the desired value of approximately 62.2%, the electron affinity of the *n*-layer was tuned from 3.55 eV to 3.48 eV.

As can be seen in Figure 4.18, this reduction in electron affinity raises the conduction band edge at the i/n interface, introducing a slightly higher barrier to electron transport than before. While this slightly

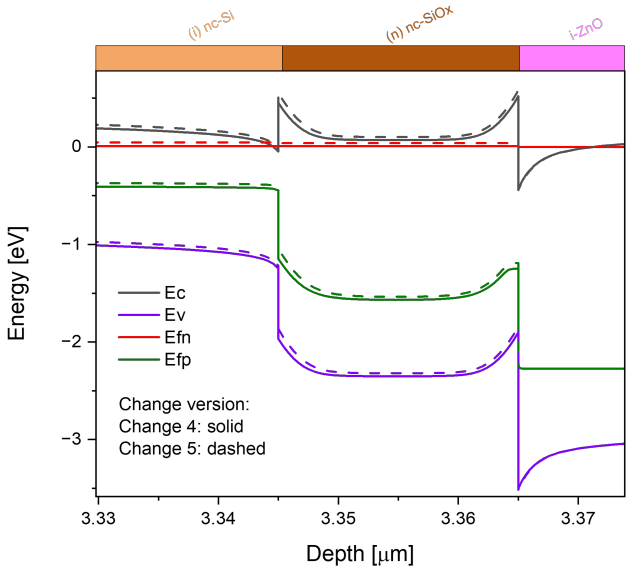

Figure 4.18: Band diagram near the i/n interface comparing baseline (solid) and reduced χ (dashed) cases. The lower electron affinity raises the conduction band edge and bends E_{fn}, indicating hindered electron extraction.

impedes carrier extraction, it lowers the FF, improving the agreement with experimental performance. As shown in Fig. 4.19, this adjustment has minimal impact on J_{sc} and EQE, confirming that the optical response remains intact.

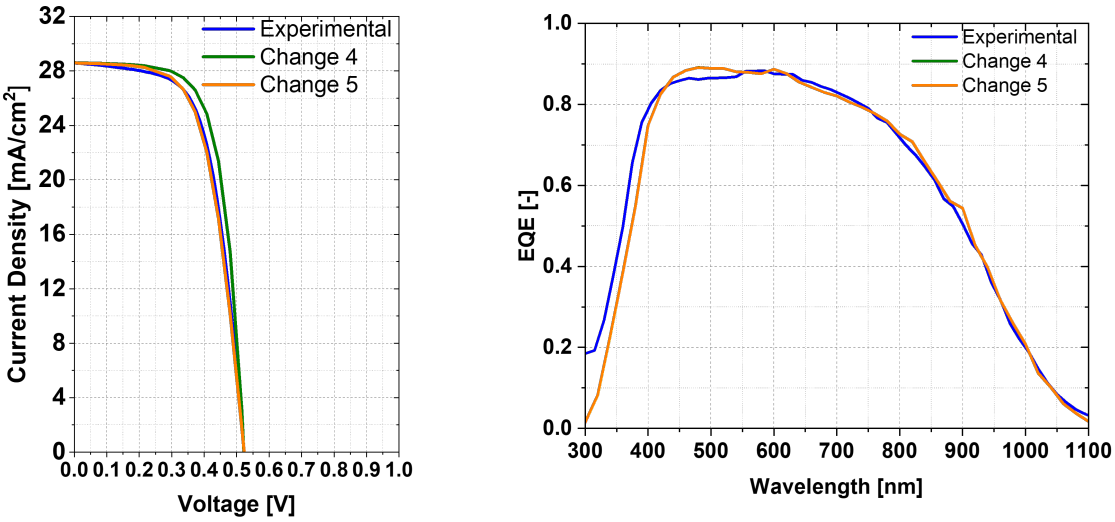

(a) Current density–voltage (J–V) characteristics.

(b) External quantum efficiency (EQE).

Figure 4.19: Final calibration step: the electron affinity of the *n*-layer was reduced from 3.55 eV to 3.48 eV to better match the experimental fill factor. Blue: initial model; green: post-mobility tuning; orange: final tuned model.

The impact of this change is illustrated in the final band diagram in Fig. 4.20, which shows the equilibrium energy profile across the device after all calibration steps.

With this adjustment, the nc-Si:H single-junction calibration was finalized, providing a consistent baseline for the subsequent tandem cell simulations. The calibrated output values are given in Table 4.6

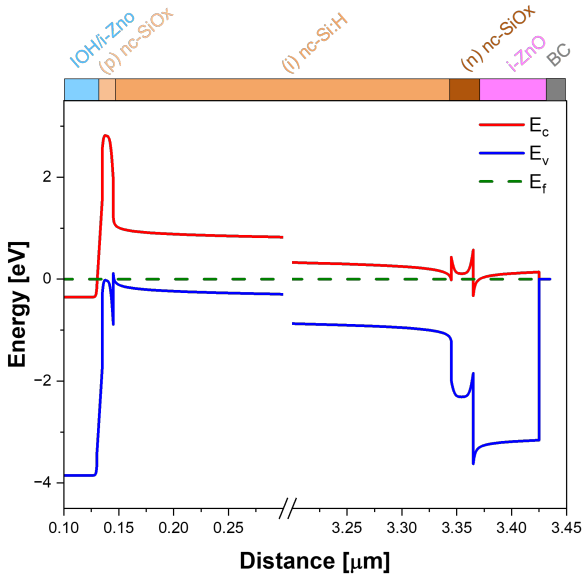

Figure 4.20: Final calibrated band diagram of the nc-Si:H single-junction solar cell after DB density adjustment.

Table 4.6: Performance comparison between experimental measurement and final simulation (Change 5)

Metric	Experimental	Final Simulation
V_{oc} [V]	0.52	0.52
$J_{\mathrm{sc,EQE}}$ [mA/cm^2]	28.60	28.59
Fill Factor [%]	62.20	62.18
Efficiency η_{EQE} [%]	9.30	9.32

4.4. a-Si:H/nc-Si:H Tandem Device

With the single-junction a-Si:H and nc-Si:H devices calibrated individually, they are combined to form the monolithic tandem configuration shown in Figure 3.1. As a starting point, the material and defect parameters established for the single-junction cells were used to ensure consistency. However, in a stacked tandem structure, the growth conditions, film properties, and defect profiles can differ significantly from those of isolated subcells. For this reason, selected material parameters were later refined to reflect tandem-specific effects such as deposition sequence, plasma exposure, and interfacial disorder. A summary of all material and defect properties used in the final tandem simulation is presented at the end of this section.

4.4.1. TRJ design

To ensure efficient operation of a monolithic tandem solar cell, the TRJ must facilitate both low-resistance carrier transport and strong recombination between the subcells. In essence, the TRJ should behave like an ohmic contact for electrons and holes from the respective subcells, while also enabling efficient recombination of photogenerated carriers. This requires appropriate band alignment, sufficient doping levels, and potentially tunneling mechanisms to allow carriers to cross the interface without significant energy barriers or recombination losses elsewhere.

In the baseline structure, the conduction and valence bands of the two layers did not align sufficiently to enable direct tunneling. To overcome this limitation, the bottom p-contact of the nc-Si:H subcell was redesigned as a bilayer: a thin, highly doped region of 4 nm adjacent to the TRJ, followed by a 16 nm region with moderate doping. This sharper doping profile increases band bending near the interface while preserving the overall quality of the contact. At the same time, the n-layer doping concentration of the a-Si:H top cell was raised from 2×10^{19} to 8×10^{19} cm^{-3}, further steepening the junction and enhancing tunneling probability.

To describe tunneling across the junction, nonlocal tunneling models (NLMs) were introduced in Sentaurus. In this formulation, tunneling is not confined to a single spatial point, but instead is represented by a length parameter extending into one side of the junction and a permeation parameter coupling into the other. This allows carriers to tunnel across a finite region where band overlap exists, which more realistically reflects band-to-band and trap-assisted tunneling mechanisms in disordered thin films.

Two configurations were investigated. The first was a B2BT model, where a nonlocal mesh extended 20 nm into the n-layer of the a-Si:H subcell and permeated 5 nm into the highly doped p-layer of the nc-Si:H subcell (Fig. 4.21a). This setup provided efficient tunneling channels across the junction and allowed strong recombination, yielding a low-resistance connection between the subcells. The second configuration was a trap-assisted tunneling (TAT) model (also with B2BT still activated), implemented by placing NLM regions on both sides of the junction (at the a-Si:H/n-layer interface and across the entire p-layer of the nc-Si:H cell). In this case, tunneling was mediated by localized defect states distributed within the bandgap, which allowed carriers to recombine gradually across the p-layer rather than through direct band overlap (Fig. 4.21b).

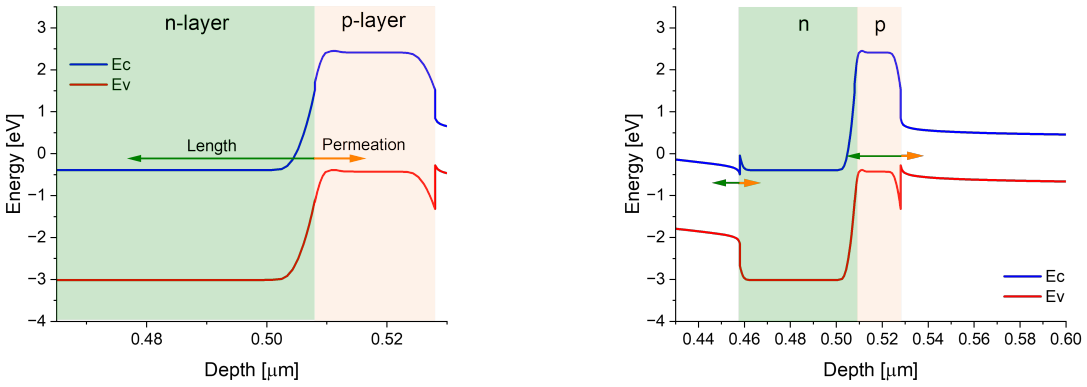

(a) B2BT TRJ.

(b) TAT TRJ.

Figure 4.21: Nonlocal tunneling mesh setups for the a-Si:H/nc-Si:H tandem device. (a) Band-to-band tunneling configuration, where the tunneling region overlaps the conduction and valence bands directly. (b) Trap-assisted tunneling configuration, where tunneling proceeds via localized defect states across the p-layer.

The two approaches led to distinct challenges in simulation. Both JV curves can be seen in Figure 4.22. The B2BT model was able to reproduce strong recombination across the TRJ and delivered high J_{sc} and V_{oc}. However, the FF in this case was significantly overestimated compared to experiment. The reason is that band-to-band tunneling represented an idealized limit, where carriers recombine efficiently with minimal resistance and no losses associated with localized defects. As a result, the simulated B2BT TRJ reflected an upper bound on device performance, lacking the resistive losses and non-ideal recombination dynamics present experimentally.

The TAT model partially corrected this by introducing recombination via mid-gap states, which more closely mirrors the behavior of disordered junctions. In this case, the simulated FF decreased and the JV curve developed a slight S-shape at low bias, consistent with the increased series resistance and recombination bottlenecks expected for trap-mediated transport. While this moved the simulation closer to the experimental behavior, the model still overestimated FF and delivered excess current at low bias, suggesting that the implemented trap distributions and tunneling parameters could not fully capture the microscopic disorder at the junction.

Overall, the comparison between B2BT and TAT modeling highlighted the sensitivity of tandem performance to TRJ assumptions. The B2BT case demonstrated the best-case scenario for tunneling, while the TAT case showed how incorporating trap-mediated recombination degrades performance and introduces non-ideal JV characteristics. Based on the above analysis, the B2BT configuration was selected as the final TRJ model for the tandem device. Although it represents an idealized scenario, the absence of S-shaped distortion at low bias and the resulting high fill factor enabled more accurate modeling of carrier extraction and overall tandem performance under ideal operating conditions. This approach

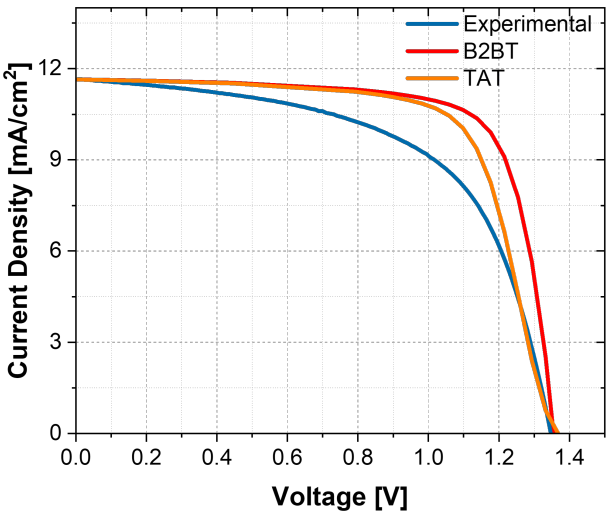

Figure 4.22: Current density–voltage (J–V) comparison between experiment (blue) and tandem simulations using two tunnel recombination junction (TRJ) models. The band-to-band tunneling (B2BT, orange) case shows ideal recombination with high J_{sc}, V_{oc}, and an overestimated fill factor (FF). The trap-assisted tunneling (TAT, red) model introduces realistic non-idealities such as increased resistance and S-shaped behavior at low bias, resulting in improved FF agreement with experiment.

provides a clearer picture of the device's upper performance limits and isolates TRJ-related transport mechanisms without the additional complexity of modeling poorly understood trap distributions. Future work may incorporate refined TAT models to better capture non-idealities observed in experimental devices.

4.4.2. Optical scaling

The GENPRO4 optical model underestimated the photocurrent in the a-Si:H top cell, making it impossible to reproduce the experimental J_{sc} even when assuming trap-free bulk material. To resolve this, the entire tandem device was illuminated with a uniformly scaled generation rate, $G'(x, \lambda) = \alpha\, G(x, \lambda)$, where α was chosen such that the simulated photocurrent matched the experimental reference. This adjustment preserved relative spectral and spatial trends in the generation profile, while ensuring proper current matching between the subcells. For EQE simulations, the unscaled AM1.5 spectrum was applied.

4.4.3. Tandem JV and EQE characteristics

The simulated tandem reproduced the experimental J_{sc} and V_{oc} values after optical scaling, as shown in Figure 4.22. However, the FF remained substantially higher in simulation than in experiment. It is important to note that the electrical properties of the a-Si:H and nc-Si:H subcells in the tandem stack may differ from those of their single-junction counterparts.

Apart from possible inaccuracies in the TRJ model, such deviations can also arise from differences in the material quality due to the deposition sequence. Thin-film silicon layers such as a-Si:H are typically deposited by plasma-enhanced chemical vapor deposition (PECVD) using silane (SiH_4) gas with hydrogen dilution, which strongly influences the dangling bond density through hydrogen passivation [52]. Small variations in gas flow or dilution ratio affect the relative abundance of SiH_3, SiH_2, SiH, and H radicals in the plasma, thereby modifying the microstructure and defect density of the resulting film [24, 40]. Moreover, in a tandem configuration the deposition order matters: the nc-Si:H bottom cell, deposited after the a-Si:H top cell, tends to develop a higher crystalline fraction, which improves doping efficiency but introduces additional grain boundaries that can act as recombination centers. These considerations justify the adjustment of defect densities and bandgap values in the tandem simulation, as the material properties cannot be assumed identical to those of the individually calibrated single-junction cells.

To better match the experimental JV curve, further adjustments were applied to the bulk material properties of the subcells. The dangling bond concentration in the a-Si:H top cell was increased from 7.8×10^{15} to 1.7×10^{16} cm^{-3}, while in the nc-Si:H bottom cell it was raised from 1.0×10^{14} to 5.0×10^{14} cm^{-3}. These changes reduced the excess current observed at low bias. To compensate for the resulting loss in V_{oc}, the bandgap of the nc-Si:H absorber was increased by approximately 0.05 eV. With these corrections, the simulated JV and EQE spectra aligned closely with the experimental data, as illustrated in Figure 4.23.

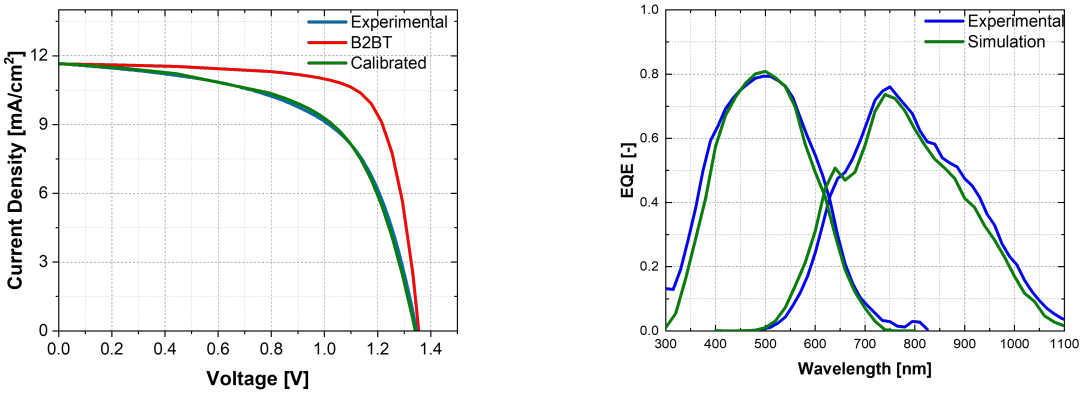

(a) JV characteristics.

(b) EQE spectra.

Figure 4.23: Final calibrated simulation results for the a-Si:H/nc-Si:H tandem solar cell. (a) Current density-voltage (JV) characteristics showing agreement between experiment (blue), idealized B2BT case (red), and final calibrated model (green). (b) External quantum efficiency (EQE) spectra for the top and bottom cells, confirming successful current matching and improved recombination modeling.

The tandem device before calibration achieved a short-circuit current density of $J_{\mathrm{sc}} = 11.65\ \mathrm{mA\,cm^{-2}}$, an open-circuit voltage of $V_{\mathrm{oc}} = 1.355\ \mathrm{V}$, and a fill factor of 74.8%, resulting in an overall power conversion efficiency of $\eta = 11.8\%$. The final calibrated tandem model achieved a short-circuit current density of 11.69 mA/cm², an open-circuit voltage of 1.34 V, a fill factor of 58.46%, and a power conversion efficiency of 9.17%, in close agreement with measured device performance, as shown in Figure 4.22 and in Table 4.7

Table 4.7: Performance comparison between experimental measurement and final simulation (Change 6)

Metric	Experimental	Final Simulation
V_{oc} [V]	1.35	1.34
$J_{\mathrm{sc,EQE}}$ [mA/cm^2]	11.65	11.69
Fill Factor [%]	58.22	58.46
Efficiency η_{EQE} [%]	9.16	9.17

4.4.4. Band diagram of the tandem device

The equilibrium band diagram of the a-Si:H/nc-Si:H tandem is shown in Fig. 4.24. It highlights the staggered band alignment between the two subcells and the role of the TRJ in connecting the n-layer of the top cell with the p-layer of the bottom cell. The offset at the interface illustrates why tunneling is required for efficient carrier recombination across the junction.

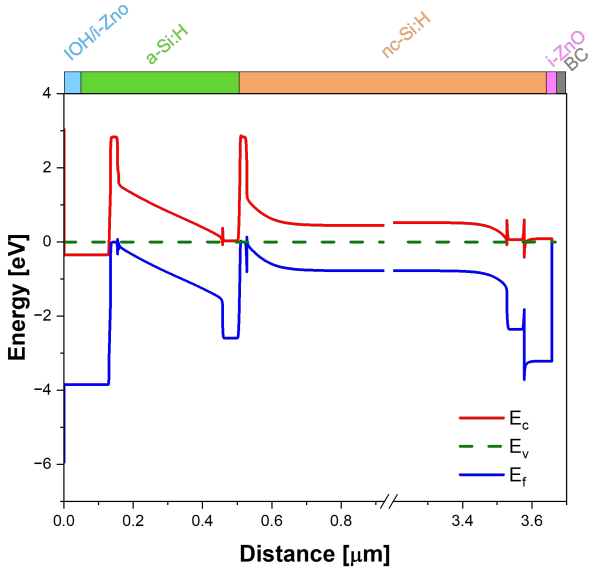

Figure 4.24: Equilibrium band diagram of the a-Si:H/nc-Si:H tandem device including the tunnel recombination junction.

4.4.5. Material and defect parameters

The final performance of the tandem a-Si:H / nc-Si:H solar cell was simulated using layer-specific material and defect parameters, as summarized in Tables 4.8 and 4.9. These include extended state properties (bandgap, electron affinity, effective density of states, dielectric constant, and carrier mobilities), exponential band-tail distributions, and Gaussian mid-gap defect states.

The parameter values were initially derived from single-junction calibrations and subsequently adapted to the tandem configuration, where necessary. For example, defect densities were increased in the top a-Si:H subcell to reflect enhanced plasma damage, while the bandgap of the nc-Si:H layer was slightly widened to recover V_{oc} lost due to recombination.

Where single-junction and tandem values differ, the tandem entries are annotated with superscripts and the deviations are detailed in the footnotes. These calibrated parameters form the electrical baseline for the final simulations presented in this chapter.

In addition to the absorber layers, the supporting front and back contact stacks were defined. AZO was used in the a-Si:H single-junction cell, while IOH, i-ZnO (front), and back i-ZnO were used in the nc-Si:H single-junction and in the tandem configuration. Their parameters, limited to extended state and transport properties, are listed in Table 4.9.

Table 4.8: Material, defect, and doping parameters for the P, I, and N layers of the tandem a-Si:H / nc-Si:H solar cell. The doping concentrations correspond to the calibrated tandem configuration. Where applicable, values differing from the single-junction (SJ) cells are annotated with superscripts.

	Top cell (a-Si:H)			Bottom cell (nc-Si:H)		
	P	**I**	**N**	**P**	**I**	**N**
Extended states						
Bandgap [eV]	2.84	1.65[(a)]	2.42	2.84	1.25[(nc)]	2.42
N_V [cm^{-3}]	1×10^{20}	1×10^{20}	1×10^{20}	1×10^{20}	6×10^{19}	1×10^{20}
N_C [cm^{-3}]	1×10^{20}	1×10^{20}	1×10^{20}	1×10^{20}	8×10^{19}	1×10^{20}
χ [eV]	3.37	4.00	3.55	3.33[(nc)]	4.05	3.39[(nc)]
ε_r [-]	11.9	11.9	11.9	11.9	11.9	11.9
μ_n [cm^2/Vs]	10	10	10	10	30	10
μ_p [cm^2/Vs]	2	2	2	2	6	2
Doping and composition						
Layer composition	nc-SiO$_x$(p) / a-SiO$_x$ (20/3 nm)[‡]	a-Si:H (300 nm)	nc-Si:H (50 nm)	nc-Si:H (20 nm)[†]	nc-Si:H (3000 nm)	nc-Si:H (20 nm)
N_A or N_D [cm^{-3}]	1.0×10^{20}/1.0×10^{18}	intrinsic	8.0×10^{19}	2.0×10^{20}/(6.5×10^{19})	intrinsic	4.0×10^{19}
Valence band tails						
Urbach energy [eV]	0.05	0.03	0.094	0.05	0.036[(nc)]	0.094
N_{Emob} [cm^{-3}/eV]	1×10^{21}	2×10^{20}	1×10^{21}	1×10^{20}	4.8×10^{19}[(nc)]	1×10^{21}
Electron σ_e [cm^2]	1×10^{-16}	1×10^{-16}	1×10^{-16}	1×10^{-16}	1×10^{-16}	1×10^{-16}
Hole σ_h [cm^2]	1×10^{-16}	1×10^{-16}	1×10^{-16}	1×10^{-16}	1×10^{-17}	1×10^{-16}
Conduction band tails						
Urbach energy [eV]	0.08	0.022	0.068	0.08	0.036[(nc)]	0.068
N_{Emob} [cm^{-3}/eV]	1×10^{21}	2×10^{20}	1×10^{21}	1×10^{20}	9.6×10^{19}[(nc)]	1×10^{21}
Electron σ_e [cm^2]	1×10^{-16}	1×10^{-16}	1×10^{-16}	1×10^{-16}	1×10^{-17}	1×10^{-16}
Hole σ_h [cm^2]	1×10^{-16}	1×10^{-16}	1×10^{-16}	1×10^{-16}	1×10^{-16}	1×10^{-16}
Dangling bonds						
Defect Concentration [cm^{-3}eV^{-1}]	1.3×10^{18}	1.74×10^{16}[(a)]	1.3×10^{18}	1.3×10^{18}	3×10^{15}[(nc)]	1.3×10^{18}
Peak Width [eV]	0.21	0.144	0.21	0.21	0.144	0.21
Donor peak position [eV]	1.1	0.92	1.1	1.1[(nc)]	0.70	1.1
Acceptor peak position [eV]	1.2	1.02	1.2	1.4[(nc)]	0.85	1.2
Donor σ_e [cm^2]	3×10^{-14}	3×10^{-14}	1×10^{-14}[(a)]	1×10^{-14}[(nc)]	3×10^{-15}	1×10^{-14}
Donor σ_h [cm^2]	3×10^{-15}	3×10^{-15}	1×10^{-15}[(a)]	1×10^{-15}[(nc)]	3×10^{-16}	1×10^{-15}
Acceptor σ_e [cm^2]	3×10^{-15}	3×10^{-15}	1×10^{-15}[(a)]	1×10^{-15}[(nc)]	3×10^{-16}	1×10^{-15}
Acceptor σ_h [cm^2]	3×10^{-14}	3×10^{-14}	1×10^{-14}[(a)]	1×10^{-14}[(nc)]	3×10^{-15}	1×10^{-14}

(a) a-Si:H SJ: intrinsic $E_g = 1.63$ eV; DB density 7.8×10^{15} cm^{-3}.
(nc) nc-Si:H SJ: intrinsic $E_g = 1.15$ eV; $E_U = 0.036$ eV with $N_{Emob} \sim 5 \times 10^{19}$ cm^{-3}/eV; DB density 1.5×10^{14} cm^{-3}.
(†) Bottom p-layer: first 4 nm doped at 2×10^{20} cm^{-3}, remaining 16 nm at 6.5×10^{19} cm^{-3}.
(‡) Top p-layer consists of 20 nm nc-SiO$_x$(p) and 3 nm a-SiO$_x$ window layer.

Table 4.9: Material parameters for AZO (a-Si:H SJ) and IOH/i-ZnO layers (nc-Si:H SJ and tandem).

	AZO	**IOH**	**Top i-ZnO**	**Back i-ZnO**
Extended states				
Bandgap E_g [eV]	3.1	3.5	3.07	3.3
Electron affinity χ [eV]	4.4	4.3	4.3	4.4
N_C [cm^{-3}]	1×10^{18}	1×10^{19}	2.2×10^{18}	2.2×10^{18}
N_V [cm^{-3}]	1.7×10^{19}	1×10^{19}	1.8×10^{19}	1.8×10^{19}
ε [-]	4.0	9.0	9.0	9.0
μ_e [cm^2/Vs]	20.3	100	5	100
μ_h [cm^2/Vs]	7.7	5	0.1	31

5

Toward Flexible and Efficient Tandem Solar Cells

The previous chapters established and validated a comprehensive simulation framework for an a-Si:H/nc-Si:H tandem solar cell on Asahi U-type textured glass. The Asahi substrate, with its optimized light-scattering properties, serves as the benchmark for optical and electrical modeling of thin-film silicon devices. While this configuration confirms the accuracy of the modeling approach, glass-based tandems are inherently rigid and relatively heavy, limiting their applicability in contexts that demand lightweight and flexible photovoltaic technologies.

Flexible solar modules, by contrast, offer clear advantages for emerging applications such as wearable and portable electronics, aerospace systems, and conformable power sources on curved or lightweight structures [27]. Several studies have demonstrated that high-quality a-Si:H/nc-Si:H tandems can indeed be fabricated on flexible substrates. Limodio et al., for example, reproduced Asahi-like light-scattering behavior on temporary aluminum substrates via modulated texturing techniques, effectively extending a-Si:H/nc-Si:H technology to flexible platforms [63, 29].

Despite these advances, thin-film silicon tandems on flexible substrates remain fundamentally limited. The weak near-infrared absorption of nanocrystalline silicon, coupled with carrier-transport bottlenecks and light-induced degradation, constrains their efficiency potential. As a result, flexible a-Si:H/nc-Si:H tandems, while manufacturable and robust, do not meet the performance targets of next-generation flexible photovoltaics.

To surpass these limitations, alternative absorber materials must be explored. Metal halide perovskites represent a particularly promising candidate due to their high absorption coefficients, tunable bandgaps, and compatibility with low-temperature, solution-based processing. Recent developments have demonstrated flexible perovskite solar cells exceeding the efficiency of thin-film silicon tandems, even when fabricated using scalable deposition and encapsulation methods [27]. These advances point toward perovskite-based architectures as a compelling pathway to combine flexibility, efficiency, and manufacturability.

This chapter builds on the validated thin-film silicon framework to explore such pathways. The transition onto a flexible substrate explained in Section 3.1.2 is used. First, the established a-Si:H/nc-Si:H tandem model is translated onto a flexible substrate to quantify the performance trade-offs relative to the Asahi glass baseline, establishing a realistic reference for flexible thin-film tandems. Subsequently, attention shifts to perovskite-based architectures. A single-junction perovskite device is developed and analyzed, with emphasis on the influence of different HTLs, specifically NiO_x, PEDOT:PSS, PTAA, SAMs and nc-SiOx. These will be discussed regarding energy alignment, carrier extraction, and device performance. Building upon these insights, a hybrid a-Si:H/perovskite tandem is designed to assess the potential of integrating perovskite absorbers within the flexible silicon framework. Finally, the chapter concludes with the simulation of an all-perovskite tandem architecture, demonstrating the pathway toward fully

flexible, high-efficiency tandem solar cells.

5.1. Flexible a-Si:H/nc-Si:H Tandem

To evaluate flexible thin-film silicon tandems, the validated Asahi-based a-Si:H/nc-Si:H model was transferred to a flexible platform by replacing the Asahi glass/IOH/ZnO front stack with an encapsulant/FTO front contact on an aluminum-foil substrate, as shown in Section 3.1.2. In this configuration, the polymer encapsulant replaces the textured Asahi glass as the mechanical support and optical entry layer.

5.1.1. Device architecture

The flexible stack mirrors experimentally pursued designs: (i) aluminum-foil substrate, (ii) encapsulant/FTO front contact, and (iii) the same a-Si:H/nc-Si:H photovoltaic layers as in the rigid reference. Apart from the front stack, all electrical layers and parameters were retained from the validated model to isolate front-stack effects. The absorber thicknesses were adjusted to reflect the flexible experimental cell: the a-Si:H i-layer was set to 225 nm (300 nm in the rigid reference), and the nc-Si:H i-layer to 2000 nm (3000 nm in the reference).

5.1.2. Initial simulation results

Using the parameters transferred from the rigid tandem, the flexible device (blue curves in Fig. 5.1) yields $J_{\mathrm{sc}} = 10.14\ \mathrm{mA\,cm^{-2}}$, $V_{\mathrm{oc}} = 1.37\ \mathrm{V}$, $\mathrm{FF} = 75.7\,\%$, and $\eta = 10.5\,\%$. Here, “uncalibrated” refers to the direct transfer of layer parameters from the rigid reference without any modification.

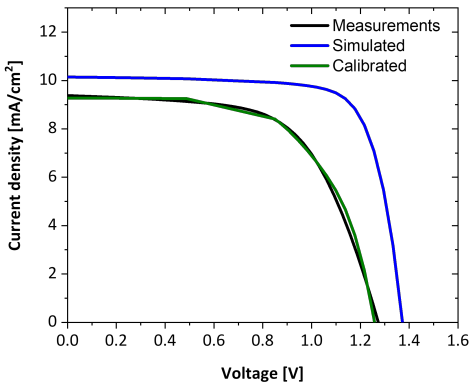

(a) Current density–voltage (J–V) characteristics: uncalibrated (blue), calibrated (green), experimental (black).

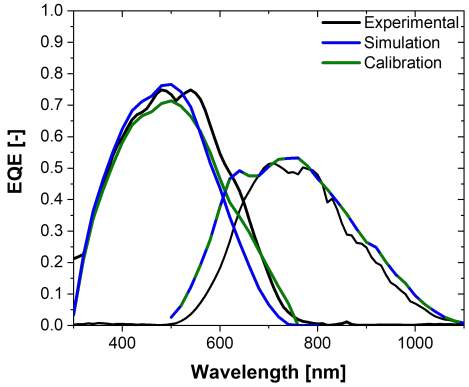

(b) External quantum efficiency (EQE): uncalibrated (blue), calibrated (green), experimental (black).

Figure 5.1: Flexible a-Si:H/nc-Si:H tandem: simulated vs. experimental performance. The uncalibrated case assumes low defect densities; the calibrated case increases dangling-bond densities to reproduce experimental recombination losses.

5.1.3. Calibration to experiment

To benchmark against a device fabricated within PVMD (2020), the model was calibrated by increasing dangling-bond defect densities in the a-Si:H to match measured recombination. The calibrated device (green) reproduces the stronger recombination-related losses near open circuit observed in experiment (black), with the performance characteristics shown in Table 5.1.

Table 5.1: Performance comparison between experimental measurement and final simulation (Change 6)

Metric	Experimental	Calibrated
V_{oc} [V]	1.27	1.28
$J_{\mathrm{sc,EQE}}$ [mA/cm^2]	9.40	9.27
Fill Factor [%]	61.60	62.97
Efficiency η_{EQE} [%]	7.60	7.49

5.1.4. Takeaways

The flexible a-Si:H/nc-Si:H tandem demonstrates clear advantages in weight and mechanical flexibility, compatible with roll-to-roll fabrication. However, its photovoltaic performance remains limited by increased recombination in the flexible stack. In the uncalibrated simulation, the device reaches just above 10 % efficiency; calibration to experimental defect densities reduces the efficiency to 7.6 %. These results highlight an intrinsic efficiency ceiling for flexible thin-film silicon tandems and motivate the exploration of perovskite absorbers as a path to higher-performance flexible devices.

As a next step, a single-junction perovskite device is introduced to benchmark different HTL choices prior to assessing hybrid and all-perovskite tandems.

5.2. Investigating HTLs for the SJ PVK

The results of the previous section demonstrate that flexible a-Si:H/nc-Si:H tandems, while manufacturable, are limited to efficiencies around 10%. Metal-halide perovskites (ABX_3) have emerged as a promising absorber materials for next-generation thin-film solar cells. They combine high absorption coefficients with long carrier diffusion lengths, and their bandgap can be tuned by compositional engineering. Importantly, perovskites can be deposited at low temperatures from solution, making them compatible with polymer foils and roll-to-roll fabrication [27]. Before going into the simulation of a SJ PVK solar cell in Section 5.3, this section discusses different HTLs which will be compared, showing their banddiagrams and the advantages and limitations of each.

5.2.1. Banddiagrams for offsets

In this section different HTL options are discussed, namely PEDOT:PSS, PTAA, NiO_x, 2PACz as SAMs and nc-SiO_x. They are all modeled with the parameters discussed in Section 3.1.3. With these models a poisson coupled simulation was done to obtain banddiagrams in equilibrium. Each of these the banddiagram can be seen in Figure 5.2.

PTAA exhibits a nearly ideal valence-band alignment with the perovskite (VBO = 0.03 eV), ensuring efficient hole extraction without significant barrier formation. This is due to its ideal valence band maximum (VBM) of 5.10 eV, which aligns good with the VBM of 5.13 eV of the narrow bandgap perovskits. Its wide bandgap leads to a large conduction-band offset (CBO ≈ 2.00 eV), which effectively blocks electron back-injection into the HTL. This combination of low VBO and high CBO makes PTAA highly selective for holes, minimizing recombination losses at the perovskite/HTL interface.

PEDOT:PSS, also shows almost perfect energetic alignment with the perovskite, featuring negligible offsets for both the valence band (VBO ≈ 0.03 eV), again due to the VBM being placed at 5.10 eV. But here however, due to the lower bandgap of 1.60 eV, a modest conduction-band offset (CBO ≈ 0.40 eV) is present. This results in efficient hole transfer and only moderate electron blocking. The smaller CBO can permit some electron leakage under forward bias, which may contribute to interfacial recombination and limit open-circuit voltage in high-performance devices.

NiO_x, with its deep valence band and wide bandgap (VBM = 5.26 eV, E_g = 3.80 eV), introduces a modest valence band offset (VBO = +0.13 eV) and a pronounced conduction band offset (CBO = 2.44 eV) with the perovskite. The large CBO effectively blocks electrons, confirming NiO_x as a robust electron-blocking layer. The small positive VBO, however, creates a slight barrier for hole transport, which can lead to mild hole accumulation at the interface. Under illumination, tunneling and thermionic emission can still enable efficient extraction, while the accumulated charge may help reduce interfacial recombination. NiO_x thus offers good selectivity and thermal stability, though its interfacial resistance remains sensitive to surface termination and stoichiometry.

The self-assembled monolayer (SAM) 2PACz again exhibits nearly ideal alignment (VBO = 0.03 eV, CBO = 2.20 eV), confirming its strong selectivity for holes. The molecular dipole associated with 2PACz helps align the perovskite Fermi level, effectively reducing nonradiative recombination at the contact. However, because the SAM is only a few nanometers thick, the large conduction-band spike can allow tunneling of electrons across the interface, partially bypassing the intended blocking function. This means that while SAMs provide excellent energetic alignment and low defect density, their extremely thin nature demands careful control of the interfacial dipole and band offset to avoid undesired electron leakage.

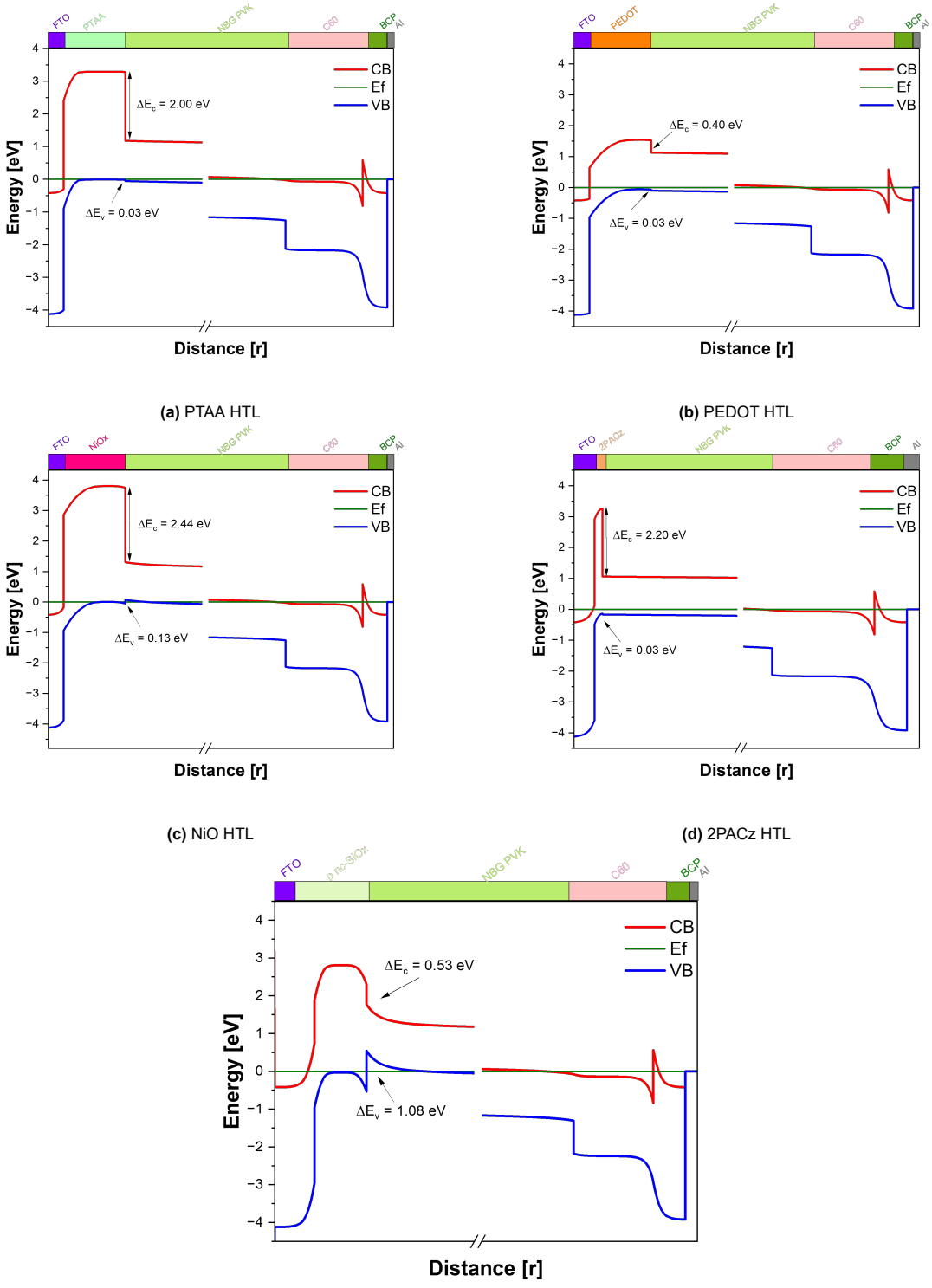

Figure 5.2: Band alignment (CB/VB), Fermi levels, and band offsets ($\Delta E_c/\Delta E_v$) at the perovskite/HTL interface for different HTLs.

In contrast, nc-SiO$_x$(p) displays a different band alignment, with a large valence-band offset (VBO = 1.08 eV) and a moderate conduction-band offset (CBO ≈ 0.53 eV). The high VBO introduces a significant barrier for hole transport under equilibrium conditions. However, this barrier induces strong

upward band bending and hole accumulation on the perovskite side of the interface, generating an intense local electric field. Under illumination and forward bias, this field supports thermally assisted and field-enhanced tunneling of holes through the valence-band spike. Additionally, localized states within the nc-SiO_x interfacial region can assist via trap-mediated tunneling, providing a parallel charge-transfer pathway. Thus, even though the static energy alignment appears unfavorable, the dynamic (operational) conditions favor selective hole extraction through a tunneling mechanism. As a result, nc-SiO_x(p) behaves as a field-assisted tunneling HTL, combining excellent electron blocking with high optical transparency and chemical robustness. Its performance depends critically on interface doping, defect-mediated transport, and the local electric field profile. When properly engineered, it can achieve selective extraction comparable to organic HTLs while offering superior thermal and environmental stability.

It should be noted that the offsets of all banddiagrams discussed above are based on literature-reported values for each material. Since these parameters can vary across studies, alternative but literature-consistent selections would yield different absolute offset magnitudes.

5.2.2. Advantages and limitations of the HTLs

The comparative advantages and limitations of PEDOT:PSS, PTAA, NiO_x, SAMs and nc-SiOx are summarized in Table 5.2. Organic HTLs such as PEDOT:PSS and PTAA are attractive due to their solution processability and good band alignment, but their limited thermal stability, dopant migration, and, in the case of PEDOT:PSS, hygroscopic and acidic properties remain critical drawbacks. As noted in [6], organic HTLs generally show high resistance when their thickness increases, which negatively impacts device performance, and stability concerns make inorganic alternatives increasingly favorable. In contrast, NiO_x combines a wide bandgap, chemical robustness, and tunability through doping, although its interfaces are often more recombinative than those of polymer HTLs. More recently, SAMs have emerged as an ultrathin interfacial alternative, offering dipole-induced band alignment and surface passivation while avoiding parasitic absorption. Their advantages are balanced by sensitivity to deposition conditions and relatively low intrinsic conductivity.

Table 5.2: Reported advantages and limitations of commonly used organic, inorganic, and SAM-based HTLs in perovskite solar cells.

HTL	Advantages	Limitations
PEDOT:PSS (organic)	• Solution-processable and compatible with scalable, low-temperature fabrication [71] • Favorable initial valence-band alignment with NBG perovskite absorbers	• Hygroscopic and acidic, leading to ITO corrosion and perovskite degradation [39] • Narrow optical bandgap ($\sim$1.6–1.7 eV) introduces parasitic absorption, reducing J_{sc} [6] • Electrical conductivity strongly dependent on formulation and post-treatment
PTAA (organic)	• Wide bandgap ($\sim$3.0 eV) and high optical transparency • Chemically stable and compatible with low-temperature processing • Favorable band alignment with a small valence-band offset	• Hydrophobic surface causes poor wettability of perovskite precursor solutions, leading to nonuniform film formation and interfacial defects [75, 21] • Requires LiTFSI/tBP dopants to achieve sufficient conductivity • Dopant migration into the perovskite layer accelerates long-term degradation [39]

Table 5.2: (continued)

HTL	Advantages	Limitations
NiO_x (inorganic)	• Wide bandgap (3.6–3.8 eV), optically transparent • High thermal, chemical, and moisture stability [39] • Deep valence band (-5.2 to -5.4 eV) aligns well with perovskite • Doping (Li, Mg, Cu, Cs, Co) enhances conductivity and band alignment	• Interfaces often defect-rich, leading to higher recombination • Pristine NiO has relatively low intrinsic conductivity • Sputtering or solvent-based deposition can damage the perovskite layer
nc-SiO_x(p)	• Tunable oxygen content allows control over bandgap (2.0–3.2 eV), work function, and electrical properties • Achieves favorable valence-band alignment with perovskite ($\sim$–5.1 eV) depending on oxygen content and doping • Highly transparent in the visible range due to its wide optical gap • Compatible with low-temperature PECVD, enabling monolithic integration in silicon-based tandem devices • Mechanically robust and chemically stable, suitable for multilayer and tandem architectures	• Low intrinsic hole conductivity compared to NiO_x or doped polymeric HTLs; heavy p-doping often required • Interface states or oxygen-rich regions can induce recombination if not properly passivated • High refractive index ($n \sim 2.0$–2.2) may cause optical interference or reflection losses if not optimized • Fabrication typically occurs in separate PECVD and perovskite process lines, raising cross-contamination and interface integration challenges
SAMs (ultrathin interlayers)	• Ultrathin ($\sim$1–2 nm), minimizing parasitic absorption losses • Dipole-induced work function tuning enables optimized energy-level alignment with the perovskite absorber [72] • Strong anchoring to the TCO surface reduces interfacial defects and non-radiative recombination • Hydrophobic surface chemistry promotes uniform, high-quality perovskite crystallization • Solution-processable and compatible with scalable, low-temperature deposition methods	• Limited intrinsic conductivity; charge transport occurs primarily through tunneling across the monolayer • Performance strongly dependent on TCO surface cleanliness and chemical termination • Processing-sensitive; incomplete coverage or molecular disorder can cause energy misalignment • Some SAM molecules require complex synthesis routes and controlled deposition environments • Long-term operational stability at module scale remains under investigation

For the purposes of this work, NiO_x is therefore selected as the HTL for subsequent simulations, however in Section 5.3 and 5.5 it is compared to other HTLs. NiO_x naturally blocks electrons very effectively because of its wide bandgap and deep VBM, but its imperfect energy alignment with the perovskite can slow down hole extraction. To fix that, researchers engineer the interface (e.g., through dipole layers, doping, or surface treatments) to optimize the energy-level alignment and improve hole transport. Nonetheless, NiO_x offers superior thermal and chemical stability compared to organic counterparts, making it a strong candidate for reliable flexible perovskite devices. Furthermore, the use of

an inorganic HTL aligns with the long-term objective of developing stable tandem architectures, where interfacial and environmental robustness are critical.

5.3. Single-Junction Perovskite Device with PTAA vs NiO_x HTL

A single-junction perovskite solar cell with a narrow-bandgap absorber ($E_g \approx 1.23$ eV) of 900 nm was simulated using identical layer stacks and optical constants, varying only the HTL between PTAA and NiO_x. The parameters of the HTL, PVK, and ETL are given in Table C.4 in Appendix C.2. Both HTLs were p-doped to $N_A = 2 \times 10^{19}$ cm^{-3}, and the electron transport side consisted of a C_{60}/BCP bilayer. Bulk SRH lifetimes and interface recombination parameters were consistent with the values summarized in Table 3.4 in Section 3.3.3.

5.3.1. Electrical performance

Both HTLs exhibit nearly identical performance, with NiO_x showing a slightly higher short-circuit current and efficiency (22.6% vs. 22.3%). The simulated EQE spectra are almost indistinguishable across the visible and near-infrared range (≈420–1000 nm), confirming that both HTLs enable similar optical absorption and carrier collection in the perovskite layer. The small EQE reduction observed for PTAA below 400 nm is attributed to increased interfacial recombination near the front contact, but this contributes negligibly to the integrated current. As both layers were modeled with the same DOS and doping, their equilibrium carrier densities within the HTL are nominally identical. Under illumination, however, carrier transport is dominated by tunneling across the HTL/AZO interface, where the effective barrier height and tunneling probability depend primarily on carrier concentration rather than on bulk mobility. NiO_x maintains a higher effective carrier concentration due to its deeper valence band and larger dielectric permittivity, which narrow the depletion region and enhance tunneling-assisted hole transport toward the AZO contact. As a result, NiOx achieves slightly improved extraction despite a larger interfacial offset. A small optical advantage (JSC, opt = 32.6 vs. 32.0 mA cm^{-2}; see Table D.3 in Appendix D) further contributes to its marginally higher current and efficiency, while both devices maintain high fill factors (=81 %) indicative of efficient overall transport.

Table 5.3: Simulated electrical parameters of the single-junction perovskite solar cell using PTAA and NiO_x as HTLs.

HTL	J_{SC} (mA cm^{-2})	V_{OC} (V)	V_{mpp} (V)	FF (%)	η (%)
NiO_x	32.60	0.854	0.733	81.29	22.64
PTAA	32.24	0.852	0.733	81.09	22.28

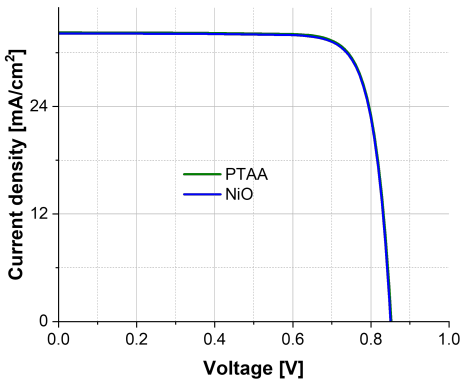

(a) Current density–voltage (J–V) characteristics: showing the higher fill factor and V_{mpp} for NiO_x.

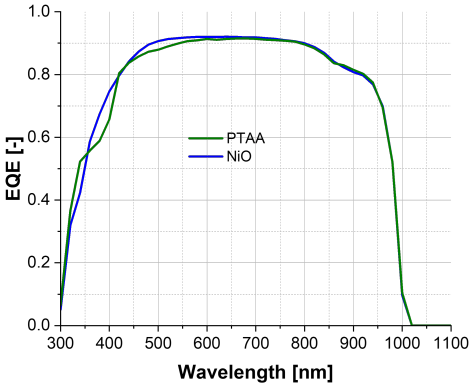

(b) Simulated EQE spectra showing similar spectral responses for both HTLs.

Figure 5.3: Electrical performance comparison of the single-junction perovskite device using NiO_x and PTAA as HTLs.

5.3.2. Thickness-dependent performance of NiO_x HTL

To evaluate the impact of absorber thickness, a parametric thickness sweep was performed for the SJ PVK with a NiOx HTL. The results, shown in Fig. 5.4, reveal the characteristic trade-off between optical absorption and recombination losses. Increasing the perovskite thickness enhances light absorption, resulting in a rise in short-circuit current density J_{sc}. However, both the open-circuit voltage V_{oc} and the FF decrease with thickness due to increased bulk recombination and longer carrier transport paths. Consequently, the overall efficiency peaks at a thickness of approximately 500–600 nm, where optical and recombination losses are optimally balanced from surface recombination and bulk recomnhination.

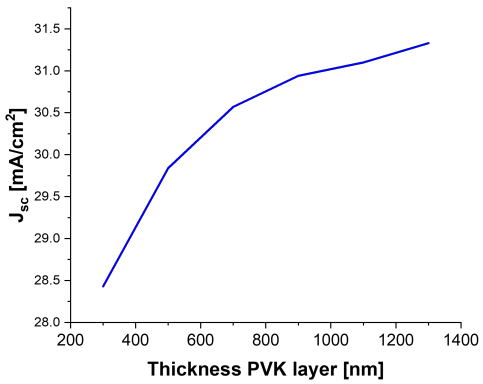

(a) Current density–voltage (J–V) characteristics: Increase in J_{sc} with absorber thickness due to enhanced absorption.

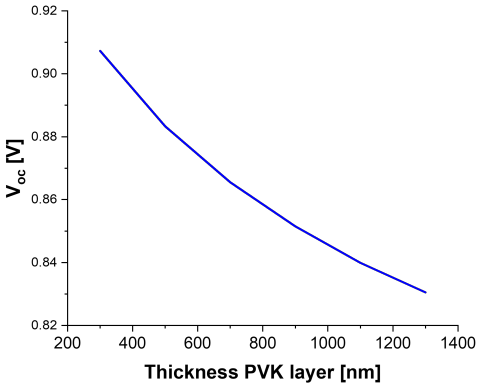

(b) Decrease in V_{oc} with thickness due to stronger bulk recombination.

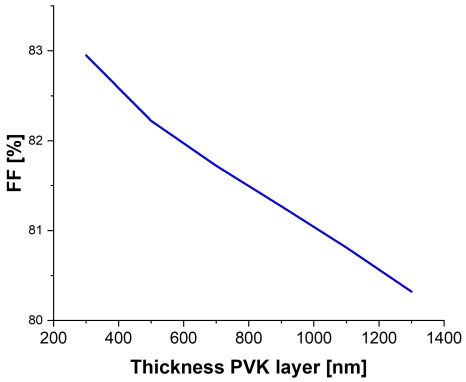

(c) Reduced fill factor (FF) with increasing thickness, reflecting transport and recombination losses.

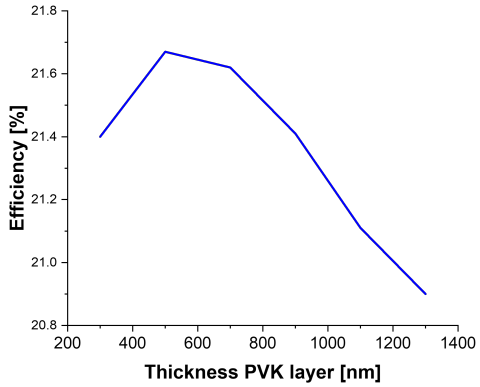

(d) Efficiency (η) peaks around 500–600 nm, balancing absorption and recombination.

Figure 5.4: Thickness-dependent trends of key performance parameters for the single-junction perovskite device with NiO_x HTL.

5.3.3. Influence of encapsulant layer

The optical encapsulant was subsequently included to assess its effect on light harvesting and current generation. The comparison of the J–V and EQE curves, shown in Fig. 5.5, indicates that the inclusion of the encapsulant enhances the short-circuit current density J_{sc} due to improved optical coupling and reduced front reflection. This improvement translates into a higher overall power conversion efficiency of approximately 22.5%.

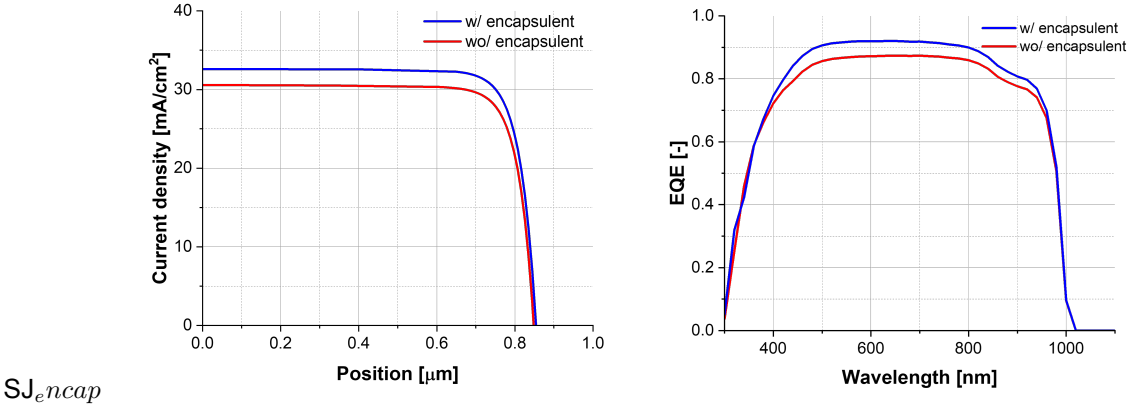

SJ_encap

(a) Current density–voltage (J–V) characteristics

(b) Simulated EQE characteristics.

Figure 5.5: Comparison of the simulated J–V characteristics and EQE curve with and without the encapsulant layer. The inclusion of the encapsulant increases J_{sc} and overall efficiency.

5.3.4. Summary and implications

The single-junction perovskite devices employing NiO_x and PTAA as hole transport layers exhibit nearly identical performance, achieving efficiencies of 22.6% and 22.3%, respectively. This confirms that both HTLs provide highly effective carrier selectivity and transport within the perovskite architecture. Given their comparable electrical behavior, the superior thermal and chemical stability of NiO_x offers a decisive advantage over organic HTLs such as PTAA, particularly for long-term operation and integration on flexible or tandem platforms. These results highlight the potential of inorganic NiO_x-based interfaces for realizing robust, high-efficiency perovskite front cells in future flexible and hybrid tandem architectures, providing a stable and scalable route beyond the performance limitations of all-silicon thin-film devices.

5.4. a-Si:H/Perovskite Tandem with NiO_x HTL

To extend the single-junction perovskite baseline, a two-terminal a-Si:H/perovskite tandem solar cell was simulated, employing NiO_x as the HTL in the perovskite subcell. In this configuration, the nc-Si:H bottom cell of the conventional a-Si:H/nc-Si:H tandem was replaced by a narrow-bandgap ($E_{\mathrm{g}} = 1.23$ eV) perovskite absorber, while the a-Si:H top cell was maintained. The perovskite subcell included the same electron transport stack as the single-junction configuration, consisting of a C_{60} ETL and a thin BCP buffer layer. The two subcells were connected through a thin ITO layer functioning as a TRJ between the n-type a-Si:H layer and the p-type NiO_x layer. The values used an a schematic of the device structure are shown in Appendix C in Section C.3.

The a-Si:H top subcell serves a functional purpose as a chemically stable encapsulant and moisture barrier for the underlying perovskite. Its dense amorphous network provides mechanical protection and environmental stability, reducing degradation caused by oxygen or water in the PVK absorber.

5.4.1. Electrical performance

The simulated tandem device achieved a short-circuit current density of $J_{\mathrm{sc}} = 12.53$ mA cm^{-2}, an open-circuit voltage of $V_{\mathrm{oc}} = 1.617$ V. With a fill factor of 77.88%, the resulting power conversion efficiency was 15.79%. The J–V and EQE characteristics of the tandem device are shown in Fig. 5.6. A slight dip in the perovskite EQE arises from optical interference between the high-index a-Si:H and the perovskite subcell, which locally reduces the optical field within the absorber.

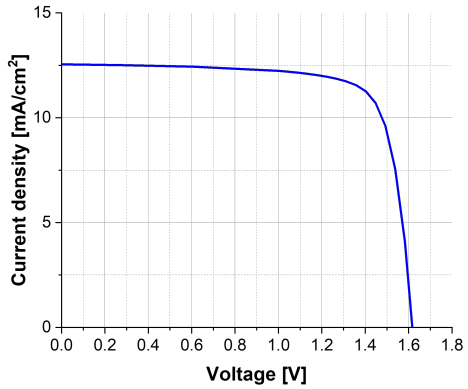

(a) Current density–voltage (J–V) characteristics.

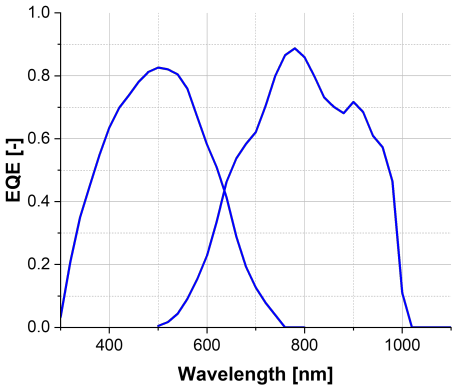

(b) External quantum efficiency (EQE).

Figure 5.6: Electrical performance of the simulated a-Si:H/perovskite tandem solar cell using NiO_x as the hole transport layer.

Although the efficiency of this hybrid tandem remains below that of state-of-the-art single-junction perovskite solar cells, it represents a clear improvement over the conventional a-Si:H/nc-Si:H tandem baseline. More importantly, the inclusion of the a-Si:H top cell enhances device stability by acting as a robust, moisture-resistant barrier for the perovskite subcell. This configuration therefore provides a viable route toward more durable hybrid tandems, particularly in scenarios where perovskite stability challenges have not yet been fully resolved.

5.4.2. Influence of the encapsulant

The optical encapsulant was again evaluated to quantify its influence on device performance. Figure 5.11 compares the simulated J–V curves with and without the encapsulant layer. As in the single-junction case, the inclusion of the encapsulant enhances light coupling into the device stack, resulting in a noticeable increase in short-circuit current and a corresponding rise in efficiency. A slight increase in V_{OC} is also observed, which is likely related to the higher overall photogeneration and a potential shift of the generation profile deeper into the absorber, effects that can, in principle, lessen the influence of interfacial recombination.

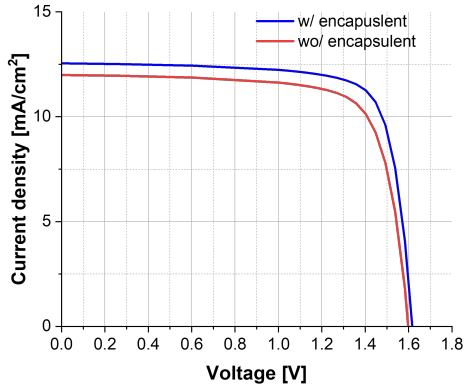

(a) Current density–voltage (J–V) characteristics.

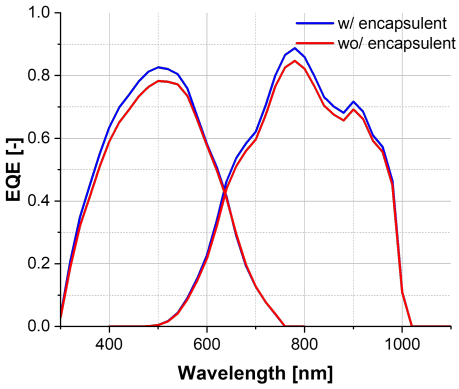

(b) External quantum efficiency (EQE).

Figure 5.7: Comparison of simulated J–V and EQE characteristics of the a-Si:H/perovskite tandem with and without the encapsulant layer. Inclusion of the encapsulant increases J_{sc} and overall efficiency.

5.4.3. Summary and implications

The simulated a-Si:H/perovskite tandem reaches 15.9% efficiency, surpassing the a-Si:H/nc-Si:H tandem due to the superior electronic quality of the perovskite bottom cell. Compared to nc-Si:H, the

perovskite exhibits longer carrier diffusion lengths, lower defect density, and higher mobility, which reduce recombination losses and enable higher V_{oc} and fill factor. Its bandgap of 1.23 eV also provides good current matching with the 1.65 eV a-Si:H top cell, minimizing optical mismatch and maximizing photocurrent utilization. In addition, the perovskite's high absorption coefficient allows for thinner absorbers, lowering series resistance and improving charge extraction.

The a-Si:H top layer further enhances stability by acting as an intrinsic encapsulant that protects the perovskite from oxygen and moisture. Altogether, the hybrid a-Si:H/perovskite tandem combines high performance, improved durability, and compatibility with flexible or low-temperature substrates, offering a practical step between silicon-based and all-perovskite tandem architectures.

5.5. All-Perovskite (PVK/PVK) Tandem Device

This section investigates an all-perovskite two-terminal tandem solar cell, where the wide-bandgap (WBG) top subcell employs a perovskite absorber with $E_{\mathrm{g}} = 1.67$ eV and the narrow-bandgap (NBG) bottom subcell uses a perovskite with $E_{\mathrm{g}} = 1.23$ eV. Three configurations are considered: (i) both subcells with inorganic HTLs, (ii) both subcells with organic HTLs, and (iii) both subcells with nc-SiO$_x$(p) as the HTL. All non-HTL layers, optical constants, and electrical parameters are kept identical across the three cases unless explicitly stated. The absorber thicknesses are fixed at $d_{\mathrm{WBG}} = 280$ nm and $d_{\mathrm{NBG}} = 900$ nm to preserve the optical current-matching condition established for the inorganic baseline. The complete layer sequences for the inorganic and organic configuration are provided in Appendix C.

5.5.1. Inorganic HTLs: NiO$_x$/NiO$_x$

In the reference configuration, both subcells employ NiO$_x$ as the HTL due to its chemical and thermal stability and favorable valence-band alignment with perovskite absorbers. For the topcell on the electron transport side, the top cell uses C$_{60}$ without an additional BCP buffer, while the subcells are interconnected by a thin ITO recombination layer that acts as an ideal TRJ. The FTO front contact is n-doped to 3.8×10^{20} cm^{-3}, a setting that is maintained for subsequent simulations.

Under these conditions, the tandem achieves $J_{\mathrm{SC}} = 16.21$ mA cm^{-2}, $V_{\mathrm{OC}} = 2.18$ V, $\mathrm{FF} = 82.64\%$, and a power conversion efficiency of $\eta = 29.13\%$. The corresponding J–V and EQE characteristics are shown in Fig. 5.8.

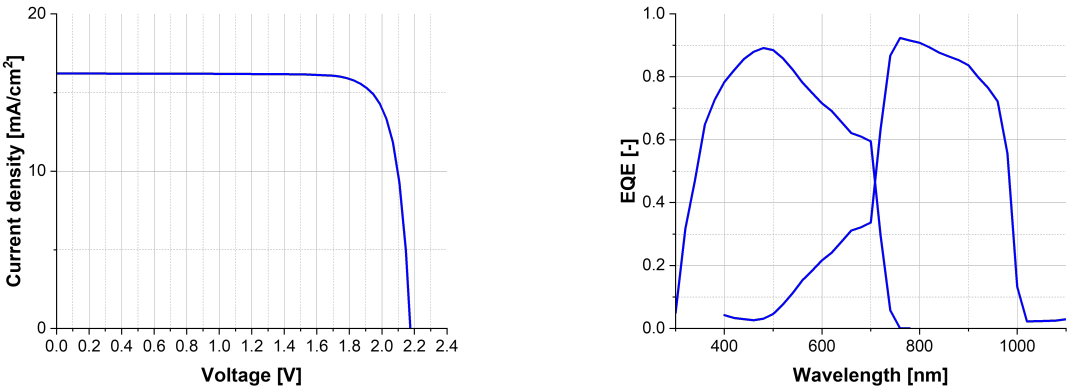

(a) Current density–voltage (J–V) characteristics.

(b) External quantum efficiency (EQE).

Figure 5.8: Electrical performance of the perovskite/perovskite tandem solar cell using NiO$_x$ as hole transport layers in both subcells.

5.5.2. Organic HTLs: PTAA/PEDOT:PSS

To isolate the influence of the HTL material, the NiO$_x$ layers were replaced by PTAA in the WBG top subcell and PEDOT:PSS in the NBG bottom subcell. Material parameters were taken from Table 3.3 in Section 3.1.3, and both HTLs were p-doped to $N_{\mathrm{A}} = 2 \times 10^{19}$ cm^{-3} for consistency with the inorganic baseline. All other layers and absorber thicknesses were kept fixed at 280/900 nm.

With PTAA/PEDOT:PSS as HTLs the tandem achieved $J_{\mathrm{SC}} = 15.71$ mA cm^{-2}, $V_{\mathrm{OC}} = 2.18$ V, $\mathrm{FF} = 77.44\%$, and a power conversion efficiency of $\eta = 26.47\%$. The simulated J–V and EQE curves are shown in Fig. 5.10.

The top-cell EQE displays a small dip near 350 nm, attributed to optical interference effects in the front stack. Because PTAA has a lower refractive index than NiO_x, the interference fringes shift slightly, modifying the local optical field distribution and reducing collection efficiency in this spectral region.

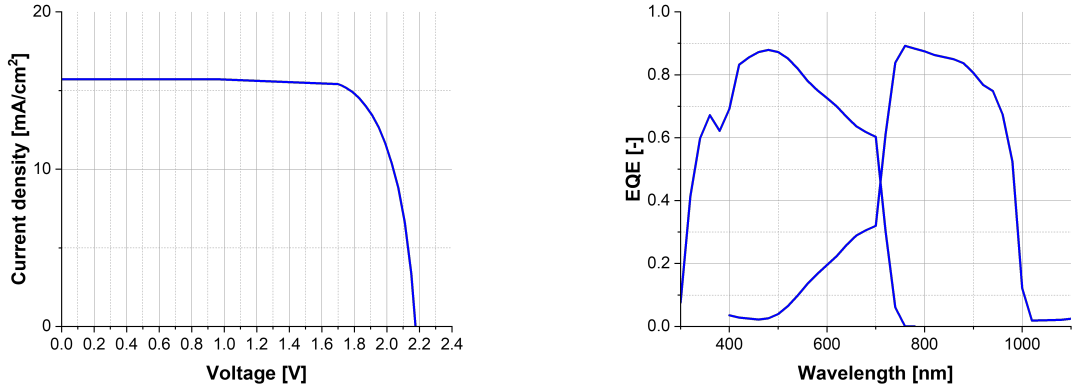

(a) Current density–voltage (J–V) characteristics

(b) External quantum efficiency (EQE).

Figure 5.9: Electrical performance of the perovskite/perovskite tandem solar cell using PTAA (top cell) and PEDOT:PSS (bottom cell) as hole transport layers.

5.5.3. nc-SiO_x HTLs

In this configuration, both subcells employ nanocrystalline silicon oxide (nc-SiO_x(p)) as the hole transport layer. The material was selected for its wide bandgap, tunable work function, and established compatibility with silicon-based tandem fabrication.

The nc-SiO_x parameters were adopted from the calibrated a-Si:H/nc-Si:H tandem model described in Section 4.4, using the same doping and defect parameters as the nc-SiOx:H(p) and window layer listed in Table 4.8. Note that the SJ a-Si:H HTL thickness of 13 nm (10 nm p(++) and 3 nm p(+) window layer) was used, instead of the 23 nm HTL which was used in the a-Si:H/nc-Si:H tandem. All other optical and electronic parameters were kept consistent with the NiO_x/NiO_x baseline.

Under these conditions, the perovskite/perovskite tandem using nc-SiO_x(p) layers achieved $J_{\mathrm{SC}} = 15.76$ mA cm^{-2}, $V_{\mathrm{OC}} = 2.16$ V, a fill factor of $\mathrm{FF} = 85.42\%$, and a power conversion efficiency of $\eta = 29.09\%$. The simulated J–V and EQE characteristics are shown in Fig. 5.10. The high fill factor and open-circuit voltage demonstrate efficient hole extraction and minimal interface recombination, confirming that nc-SiO_x(p) provides a suitable energetic alignment with the perovskite valence band.

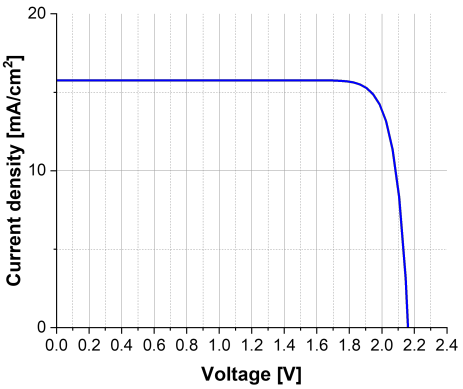

(a) Current density–voltage (J–V) characteristics.

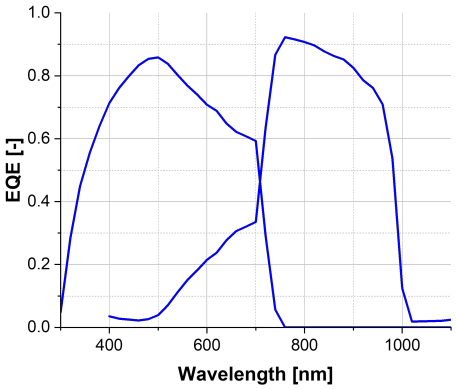

(b) External quantum efficiency (EQE).

Figure 5.10: Electrical performance of the perovskite/perovskite tandem solar cell using nc-SiO_x(p) as hole transport layers in both subcells.

5.5.4. Performance comparison

The performance differences in Table 5.4 can be explained by the interfacial transport characteristics of the respective HTLs. In these tandems, tunneling is primarily active at the front contact/HTL interface, where the local barrier width and tunneling probability are strongly influenced by the carrier concentration and doping within the HTL. Although nc-SiO_x(p) exhibits low conductivity, its high DOS and effective doping yield a larger equilibrium hole density near the contact. This narrows the depletion region and enhances tunneling-assisted charge transfer to the transparent electrode, resulting in performance comparable to the NiO_x/NiO_x configuration despite the lower intrinsic mobility.

In contrast, the organic PTAA/PEDOT:PSS stack shows a reduced fill factor and short-circuit current, which can be attributed to its lower carrier density. The reduced hole concentration broadens the tunneling barrier and diminishes field-assisted transport, while the lower mobility in PTAA increases series resistance. Furthermore, its stronger optical absorption in the visible range introduces additional parasitic losses, slightly reducing the short-circuit current, as shown in Figure D.5 in Appendix D. Consequently, the organic tandem achieves a lower overall efficiency, whereas both NiO_x- and nc-SiO_x-based tandems maintain high fill factors and open-circuit voltages, consistent with efficient tunneling-mediated charge extraction and low interfacial recombination.

Table 5.4: Performance of all-perovskite tandems with different HTL combinations. Absorber thicknesses fixed at 280/900 nm; HTL p-doping fixed at 2×10^{19} cm^{-3}.

HTL configuration (HTL_{ToC}/HTL_{BoC})	J_{SC} (mA cm^{-2})	V_{OC} (V)	FF (%)	η (%)
NiO_x/NiO_x	16.21	2.18	82.64	29.13
PTAA/PEDOT:PSS	15.71	2.18	77.44	26.47
nc-SiO_x(p)/nc-SiO_x(p)	15.76	2.16	85.42	29.09

5.5.5. Effect of the encapsulant

To assess the optical contribution of the encapsulant, the NiO_x/NiO_x all-perovskite tandem was re-simulated with and without the encapsulant layer included in the front optical stack. As shown in Fig. 5.11, the presence of the encapsulant leads to a clear enhancement in short-circuit current density and EQE response across both subcells.

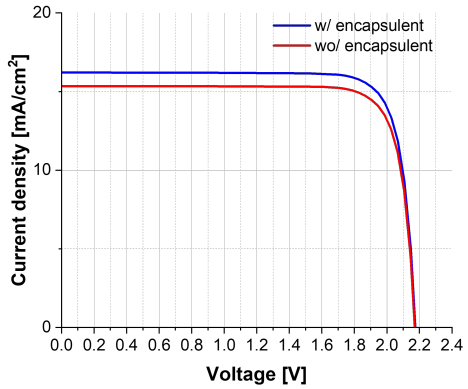

(a) Current density–voltage (J–V) characteristics.

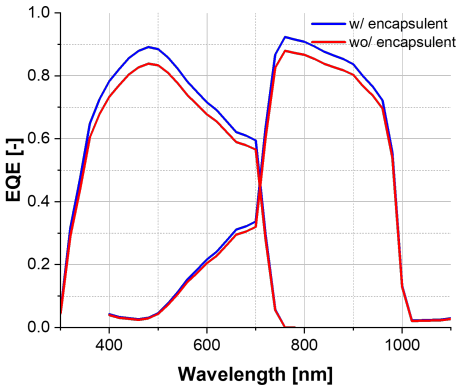

(b) External quantum efficiency (EQE).

Figure 5.11: Comparison of simulated J–V and EQE characteristics of the perovskite/perovskite tandem with NiOx HTL, with and without the encapsulant layer. Inclusion of the encapsulant increases J_{sc} and overall efficiency.

The J–V curve (Figure 5.11a) shows that including the encapsulant increases J_{SC} by approximately 1 mA cm^{-2}, while V_{OC} and FF remain essentially unchanged. This improvement originates from optical effects rather than electrical changes: as seen in the EQE spectra (Figure 5.11b), the encapsulant reduces front-surface reflection and enhances photon coupling into the device, particularly in the 400–800 nm range corresponding to the absorption region of the WBG top cell. The gain is maintained across the near-infrared range as well, contributing to a higher integrated photocurrent and an overall efficiency increase of about 1.6% relative.

6

Fill Factor Compensation Study and Design Rules

In monolithic tandem solar cells, the subcells are connected in series, which forces the total short-circuit current to be limited by the subcell that generates the lowest photocurrent. This current-matching constraint makes the tandem output highly sensitive to optical balance between the absorbers. Conventionally, optimum performance is expected when the two subcells deliver equal photocurrents. However, experimental and modelling studies have shown that the point of maximum efficiency often deviates from strict current matching [9, 8].

photocurrents of the two subcells are not matched, the current-surplus subcell must operate at a larger forward bias to dissipate its excess carriers. This adjustment alters the J–V curve of the tandem and can lead to an apparent increase in the effective fill factor, partly compensating for the current loss. The result is that the efficiency maximum may be reached under slightly mismatched conditions, rather than at perfect current balance. This phenomenon is referred to as fill factor compensation.

The extent and direction of the compensation depend on the recombination mechanisms in the absorbers and at the interfaces. In devices based on a-Si:H and nc-Si:H, bulk trap-assisted recombination is dominant, making the tandem particularly sensitive to carrier accumulation under mismatch. In perovskite-based tandems, bulk recombination is weaker and transport is more efficient, so the role of interface recombination becomes more pronounced. These differences mean that the location of the efficiency maximum relative to current match varies depending on the material system and its dominant recombination pathways.

To clarify the practical implications of fill factor compensation in tandem solar cells, this chapter examines how the effect manifests under varying current mismatch conditions. Two complementary approaches are used to isolate the optical and electrical contributions to the phenomenon. First, Section 6.1 investigates the influence of absorber thickness by sweeping the thicknesses of both subcells and analyzing the resulting trends in J_{SC}, V_{OC}, FF, and efficiency. Second, Section 6.2 introduces controlled current mismatch using the optical generation scaling method of Bao et al. [8], which decouples electrical mismatch effects from purely optical changes. Together, these methods reveal how the magnitude and direction of FF compensation depend on material-specific recombination pathways and carrier transport dynamics.

Section 6.3 provides a conceptual visualization of FF behavior under different matching regimes, highlighting the voltage-sharing dynamics that underpin the compensation effect. This is followed by five targeted case studies in Section 6.4, each examining a specific physical or optical design lever—such as absorber thickness, bandgap tuning, contact design, intermediate reflectors, or light-induced degradation—that governs the onset and strength of FF compensation. Based on the insights from these case studies, Section 6.5 formulates a set of practical design rules for optimizing stabilized performance in a-Si:H/nc-Si:H tandems, where the top cell becomes current-limiting after degradation.

Finally, Section 6.6 compares these findings to the behavior of all-perovskite tandem architectures, underscoring how the relevance of FF compensation depends on the symmetry of recombination losses and transport characteristics across the subcells.

6.1. Thickness-Dependent Performance

The optical–electrical performance of the tandem device was first investigated by sweeping the absorber thicknesses of both the a-Si:H top cell and the nc-Si:H bottom cell. For this sweep the model described in Section 4.4.3 was used, before calibration. This is thus a rigid configuration. The contour plots in Figure 6.1 summarize the dependence of J_{SC}, V_{OC}, FF, and η on the subcell thicknesses. The white line marks the optical current-matching condition. Below this line, the bottom cell limits the tandem current, while above it the top cell becomes current-limiting.

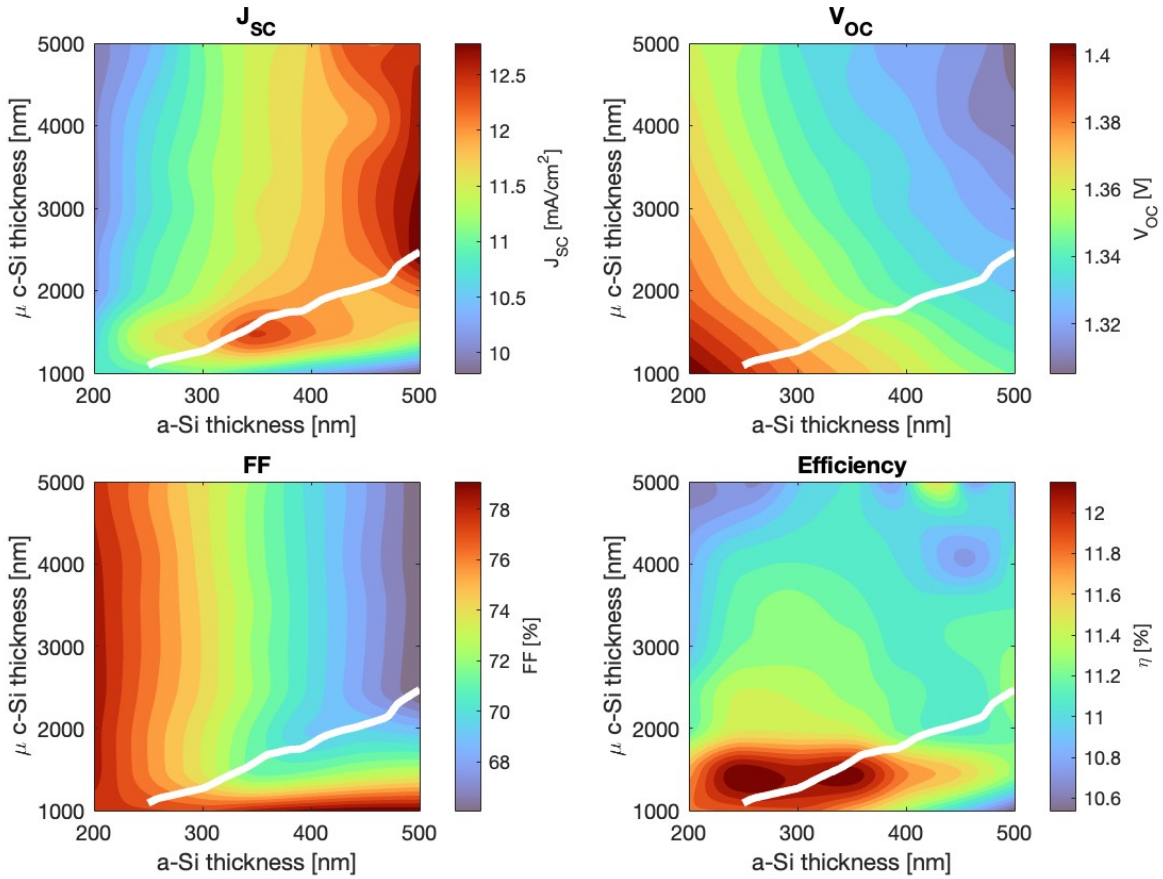

Figure 6.1: Simulated dependence of J_{SC}, V_{OC}, FF, and efficiency on the a-Si:H (top-cell) and nc-Si:H (bottom-cell) absorber thicknesses. The white line marks optical current matching.

The four plots of Figure 6.1 show distinct thickness-dependent trends. The short-circuit current J_{SC} increases with top-cell thickness, since thicker a-Si:H absorbers capture more of the visible spectrum. However, the tandem current is ultimately limited by the weaker subcell. The highest short-circuit currents appear in the upper-right corner of the thickness space, where both the nc-Si:H bottom cell exceeds about 2000 nm and the a-Si:H top cell exceeds about 450 nm. In this regime, each subcell absorbs nearly the full portion of the spectrum allocated to it: the thick nc-Si:H layer captures most of the near-infrared light, while the thick a-Si:H layer absorbs the visible light.

However, this does not directly lead to higher performance, as thicker top cells suffer from increased recombination and weaker internal fields. In contrast, the open-circuit voltage V_{OC} exhibits only minor variations with thickness. It is highest when both absorbers are thin, due to stronger quasi-Fermi level splitting under illumination and reduced recombination, but otherwise remains nearly constant across the full design space. The efficiency contour shows that maximum η is obtained for relatively thin

absorbers in both subcells. In this regime, J_{SC} is moderate, but the strong fields and short collection lengths enable higher FF and reduced recombination losses. Thus, the efficiency maximum does not coincide with maximum J_{SC} or strict current matching, but with an optimum balance between absorption, carrier transport, and recombination dynamics.

The FF shows the pronounced dependence on the absorbers thickness. In the top-cell-limited regime, FF is particularly sensitive to the a-Si:H thickness. For thin absorbers (below about 300 nm), the depletion region could span the entire intrinsic layer. In this case, the electric field extends across the full width, such that carrier collection is drift-dominated rather than diffusion-limited. As a result, photogenerated carriers are efficiently swept toward the contacts, reducing the likelihood of recombination via tail states or mid-gap dangling bonds, and leading to higher FF values.

For thicker absorbers, the depletion region no longer covers the full layer. A quasi-neutral region forms, and carriers generated there must diffuse toward the junction before being collected. In a-Si:H, carrier mobilities are intrinsically low ($\mu_e \sim 1$–10 cm^2/Vs, $\mu_h \sim 0.1$–1 cm^2/Vs) [58], such that the diffusion length

$$L = \sqrt{D\tau} = \sqrt{\frac{\mu k T}{q}\tau}, \tag{6.1}$$

is often comparable to or smaller than the absorber thickness. Here D is the diffusivity, μ the mobility, τ the carrier lifetime, k the Boltzmann constant, T the temperature, and q the elementary charge. As a result, carriers generated outside the depletion region are prone to recombination before being collected, which increases space-charge buildup and distorts the internal electric field, ultimately reducing the FF.

The evolution of the internal field and recombination with thickness is illustrated in Figure 6.2. Figure 6.2a shows that thin absorbers (200 nm) maintain a strong, nearly uniform electric field across the full layer, corresponding to effective full depletion and drift-dominated transport. In thicker absorbers (400 nm), the average field level decreases and large parts of the bulk experience weak fields (about 10^4–10^5 V/cm), where transport is diffusion-limited. Figure 6.2b shows the corresponding gap-state recombination rates. In thin absorbers, recombination is suppressed because carriers are rapidly swept out by the strong field. In contrast, thicker absorbers exhibit enhanced and more distributed recombination, consistent with diffusion-driven transport and the low mobility of a-Si:H.

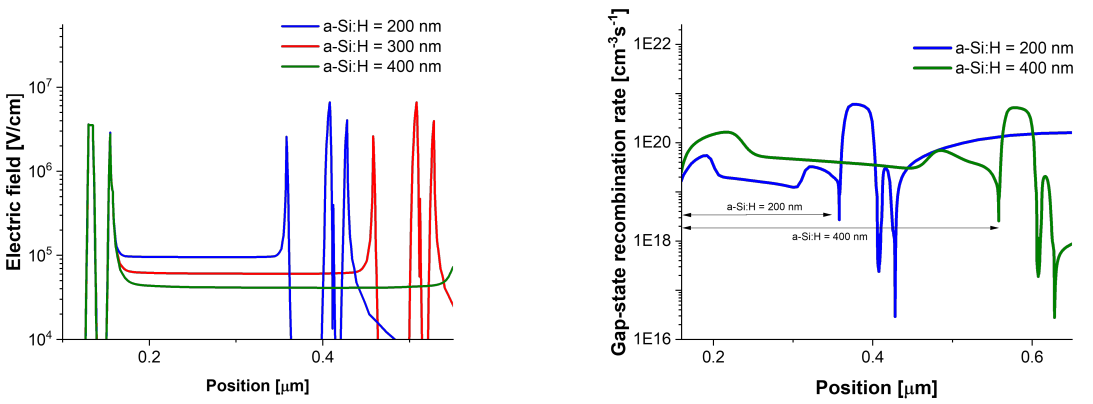

(a) Electric field distribution

(b) Gap-state recombination rate

Figure 6.2: Simulated (a) electric field and (b) gap-state recombination in the a-Si:H top absorber for thicknesses of 200 nm and 400 nm. Thinner absorbers maintain a stronger, more uniform field and lower recombination, while thicker ones suffer from field weakening and enhanced defect-mediated losses, consistent with the model of Stückelberger *et al.* [65].

The underlying physics of diffusion can be understood in terms of Brownian motion: charge carriers undergo random thermal motion driven by lattice vibrations, analogous to the random walk of particles suspended in a fluid. This behavior is formalized by the Einstein relation,

$$D = \mu \frac{kT}{q}, \tag{6.2}$$

which links the diffusion coefficient D to the carrier mobility μ. In low-mobility materials such as a-Si:H, this Brownian motion is slow, increasing the probability of recombination before carriers reach the junction. Higher mobility enhances the directed component of transport relative to this random motion, allowing carriers to traverse the absorber more efficiently and supporting a higher fill factor.

Doping also plays a decisive role. Increasing the doping in the p- and n-type contact layers enhances the built-in potential and the depletion width W,

$$W \approx \sqrt{\frac{2\epsilon(V_{\mathrm{bi}} - V)}{qN_{\mathrm{eff}}}}, \tag{6.3}$$

where ϵ is the dielectric permittivity, V_{bi} the built-in voltage, V the applied bias, and N_{eff} the effective doping concentration. A larger depletion width improves carrier collection in thin devices. However, excessive doping introduces ionized impurity scattering and increases the density of defect-related recombination centers, which can counteract the benefits and lower FF. In thicker absorbers, where a quasi-neutral region is present, these defects further hinder carrier diffusion, increasing recombination before collection. This amplifies losses in the quasi-neutral region and contributes to reduced fill factor.

6.2. Controlled Current Mismatch

The thickness sweeps in Section 6.1 showed that the tandem efficiency does not necessarily reach its maximum under perfectly matched photocurrents, but rather under slightly imbalanced conditions. However, varying the absorber thickness affects both optical absorption and electrical transport simultaneously, making it difficult to isolate the pure influence of current mismatch on the FF. To decouple these effects, the optical generation scaling method proposed by Bao et al. [8] was adopted.

The two subcells of the a-Si:H/nc-Si:H tandem were first tuned to optical current matching by adjusting the absorber thicknesses to 450 nm for the a-Si:H top cell and 2000 nm for the nc-Si:H bottom cell. Starting from this matched baseline, controlled mismatches were introduced by scaling the optical generation rates of the individual subcells, $G_{\mathrm{a\text{-}Si:H}}$ for the top cell and $G_{\mathrm{nc\text{-}Si:H}}$ for the bottom cell, according to

$$G_{a\text{-Si:H}} = (1 + \Delta)\, G^{AM1.5}_{a\text{-Si:H}}, \qquad G_{nc\text{-Si:H}} = (1 - \Delta)\, G^{AM1.5}_{nc\text{-Si:H}}. \tag{6.4}$$

Here, Δ is a dimensionless scaling factor representing the degree of intentional current mismatch. A value of $\Delta = 0$ corresponds to perfect current matching, $\Delta > 0$ denotes bottom-cell limitation (the top cell generates surplus current), and $\Delta < 0$ indicates top-cell limitation.

The Δ parameter is dimensionless and does not represent an absolute current density. Instead, it expresses the fractional deviation from the current-matched condition. For instance, if the matched tandem (450 nm / 2000 nm) delivers $J_{\mathrm{match}} = 12.5$ mA,cm^{-2}, a mismatch of $\Delta = 0.1$ corresponds to a bottom-cell limitation of $0.1 \times 12.5 = 1.25$ mA,cm^{-2}.

Figure 6.3 schematically illustrates how mismatch drives carrier accumulation. When $\Delta > 0$, the top cell generates surplus carriers and electrons accumulate near its n-layer. Conversely, for $\Delta < 0$, the bottom cell is current-surplus and holes accumulate. In both cases, these excess carriers modify the J–V curves of the individual subcells and shift the tandem FF, forming the physical basis of the compensation effect.

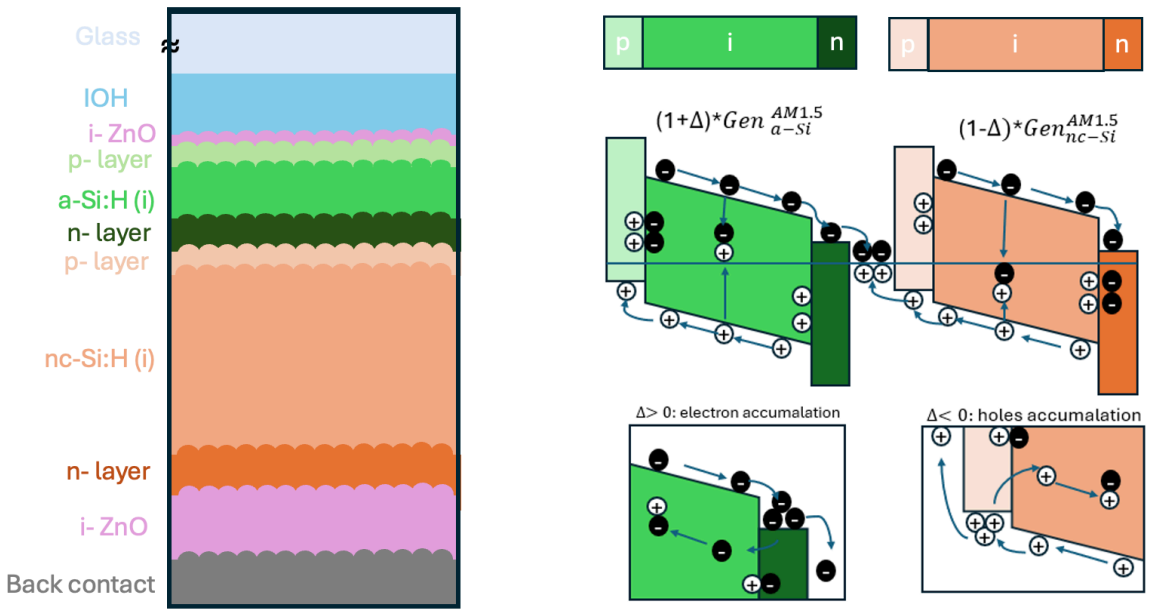

Figure 6.3: Schematic illustration of carrier accumulation under controlled current mismatch. Electron accumulation dominates when the bottom cell limits the current, while hole accumulation dominates when the top cell limits it. These excess carriers alter the J–V curves of the individual subcells and drive the FF compensation effect.

6.2.1. Trends in J_{SC}, V_{OC}, FF, and η

The simulated performance trends are summarized in Figure 6.4. The short-circuit current J_{SC} reaches its maximum at $\Delta = 0$, corresponding to perfect current balance, and decreases almost symmetrically under top- or bottom-limiting conditions. In contrast, the open-circuit voltage V_{OC} remains nearly constant across the full range of Δ, as it is governed by quasi-Fermi level splitting rather than current balance.

As illustrated in Figure 6.4, the fill factor exhibits a pronounced non-monotonic dependence. It reaches a minimum at $\Delta = 0$ and recovers under both top- and bottom-limiting conditions. This FF compensation arises because the current-surplus subcell must operate at a larger forward bias to dissipate its excess carriers, thereby reshaping its J–V curve and increasing the overall tandem FF [8]. Consequently, the power conversion efficiency peaks at slightly positive Δ values corresponding to mild bottom-cell limitation.

6.2.2. Comparison with Perovskite Tandems

For comparison, Figure 6.5 shows the same Δ-sweep applied to the all-perovskite tandem. The full two-terminal model with inorganic NiO_x HTLs (defined in Section 5.5.1) was used. Several important differences emerge compared to the a-Si:H/nc-Si:H reference.

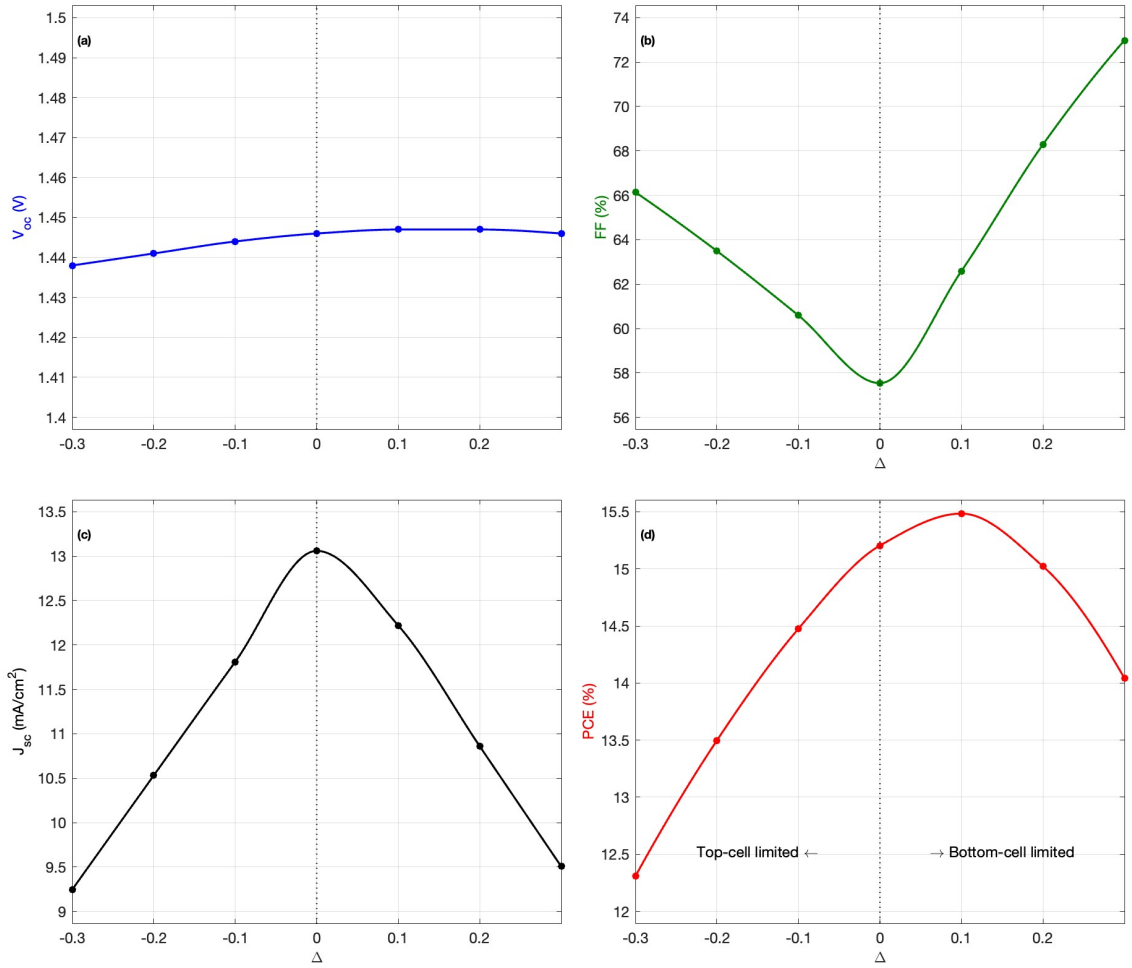

Figure 6.4: Simulated effect of controlled current mismatch on tandem performance. (a) V_{OC}, (b) fill factor, (c) short-circuit current density, and (d) efficiency. The FF is lowest at exact current match and recovers under both top- and bottom-limiting conditions, resulting in a maximum efficiency at slightly positive Δ (bottom-cell limitation).

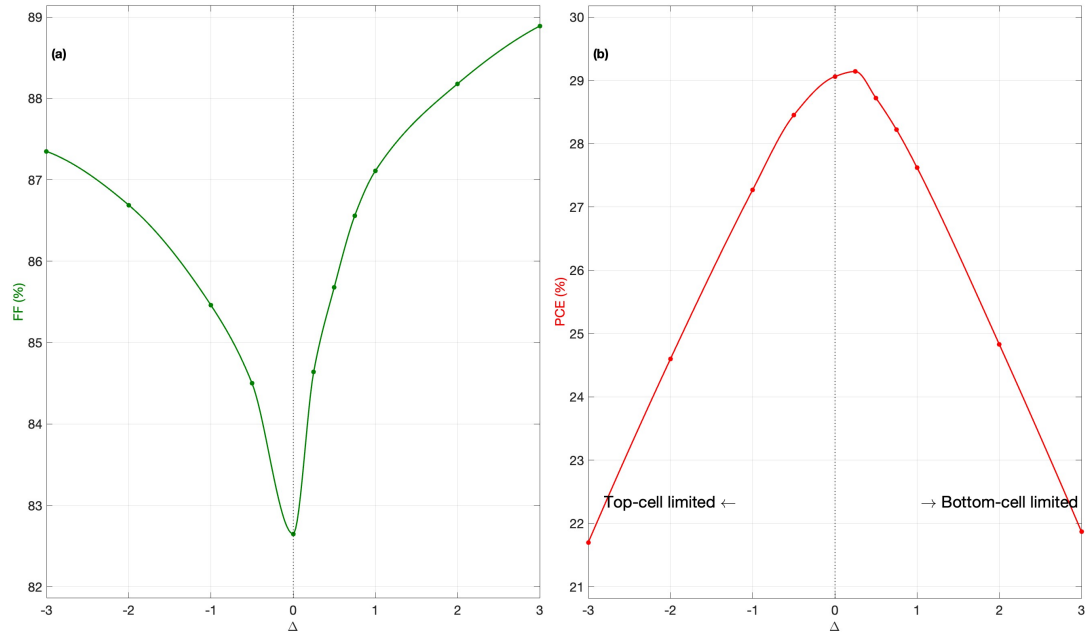

Figure 6.5: Simulated effect of controlled current mismatch on an all-perovskite tandem. (a) V_{OC}, (b) fill factor, (c) short-circuit current density, and (d) efficiency as a function of Δ.

The trends in J_{SC} and V_{OC} are comparable to those of the silicon-based tandem: the short-circuit current peaks at $\Delta = 0$ and decreases symmetrically with mismatch, while V_{OC} remains nearly constant, confirming that it is again governed primarily by quasi-Fermi level splitting rather than current balance.

In contrast, the fill factor exhibits only a mild compensation effect, reaching a minimum of approximately 83% at perfect current match and increasing modestly to about 88–89% under both top- and bottom-limited conditions. This weaker dependence arises because both perovskite subcells possess similar transport and recombination properties. Recombination is dominated by well-passivated interfaces with low defect densities, resulting in minimal asymmetry between the subcells. Consequently, carrier accumulation and field redistribution under current mismatch are less pronounced than in disordered silicon absorbers.

As a result, the PCE curve in Figure 6.5 peaks very close to $\Delta = 0$, with only a slight shift toward bottom-cell limitation. This near-symmetric optimum reflects the balanced electronic quality of both perovskite absorbers, where recombination and transport losses are comparable across the junctions. A slight shift of the PCE maximum toward bottom-cell limitation remains, indicating a minor but still present fill factor compensation effect, which is much weaker than in silicon-based tandems.

6.3. Visualisation of FF behavious under different current matching conditions

The FF of a two-terminal tandem solar cell exhibits a non-monotonic trend as the top-cell photocurrent density $J_{\mathrm{ph,top}}$ is varied, while the bottom cell parameters are held constant. This behavior arises from how the tandem system allocates internal voltage between the two subcells in order to maintain current continuity under series connection. This is visualized in Figure 6.6. Note that this is not a real device simulation. The recombination current (J_{rec}) is kept constant, and the top-cell photocurrent densities (J_{ph}) are chosen illustratively to highlight the underlying mechanism.

At low $J_{\mathrm{ph,top}}$ (15 mA/cm^2), the tandem operates in a top-limited regime. Here, the top cell generates less current than the bottom cell and dictates the total current of the tandem. The bottom cell is forced to operate below its own MMP, typically at a higher voltage. Conversely, the top cell remains close to its optimal operating point. As a result, the overall voltage distribution favors efficient operation of the dominant (limiting) subcell, and the tandem FF remains relatively high.

As $J_{\mathrm{ph,top}}$ increases and approaches the bottom-cell photocurrent ($J_{\mathrm{ph,bot}}$), the system enters the current-matching regime. In this configuration, both subcells are required to deliver the same current, and the total tandem voltage must be divided such that neither subcell operates at its ideal bias. This mutual compromise causes both cells to operate under suboptimal conditions, increasing recombination losses and reducing power output per voltage. Consequently, the fill factor reaches a local minimum, even though the current is maximized. This illustrates that the point of maximum current is not necessarily the point of maximum fill factor or efficiency.

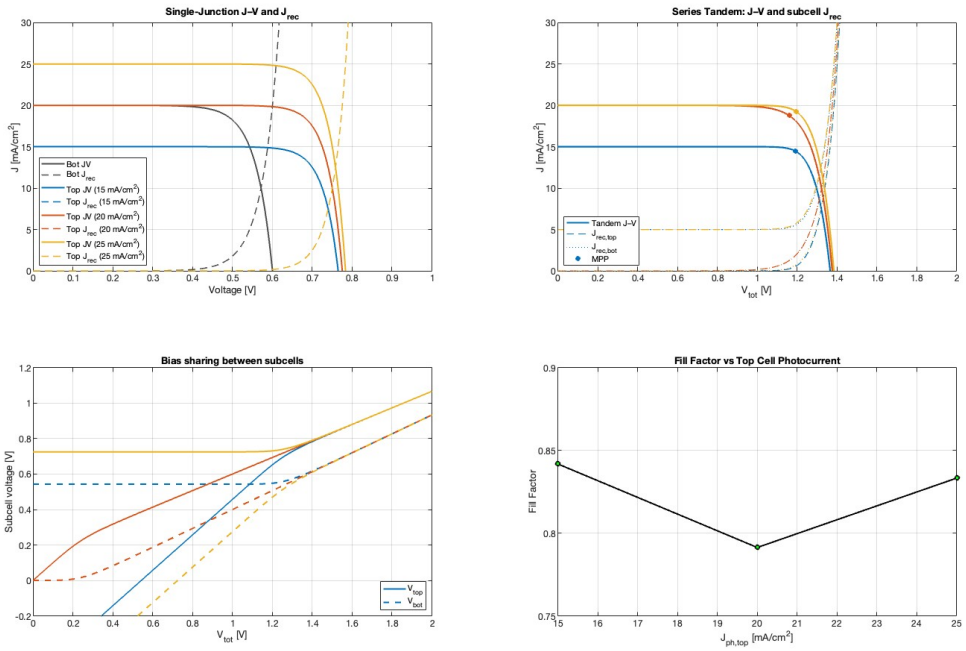

Figure 6.6: Tandem behavior under varying top-cell photocurrent $J_{\mathrm{ph,top}}$. When the top cell is current-limiting (15 mA/cm^2), the fill factor (FF) is relatively high. As the top and bottom currents become matched (20 mA/cm^2), FF dips due to both cells operating at suboptimal voltages. At bottom-limiting (25 mA/cm^2), FF recovers partially as the top cell returns to favorable operating conditions. This non-monotonic FF trend illustrates the impact of internal voltage sharing in two-terminal tandems.

At higher $J_{\mathrm{ph,top}}$ values, the system transitions to a bottom-limited regime. Here, the bottom cell generates less photocurrent and therefore dictates the tandem current. It operates close to its own MMP, as it defines the series-limited current. The top cell, on the other hand, produces excess photocurrent and must adjust its operating voltage downward to match the lower current of the bottom cell. This reduces its internal recombination losses and partially restores the tandem FF. Although the top cell operates below its individual MPP, the bottom cell remains in a favorable bias regime, and the overall tandem voltage distribution becomes more balanced. Consequently, the FF recovers compared to the current-matched condition, where both subcells are simultaneously driven away from their optimal operating points.

6.4. Targeted Case Studies on FF Compensation Mechanisms

To systematically explore the mechanisms behind the effect of FF in tandem solar cells, five targeted case studies were performed. Each study isolates a different aspect of device design that influences current mismatch, recombination dynamics, or internal electric fields, all of which affect the strength and onset of FF recovery.

While additional strategies such as p-layer bandgap grading, back-contact engineering, or advanced interface passivation could also modulate FF behavior, the present work limits its scope to five core design levers:

1. C1: Absorber thickness variation – Investigating how the thicknesses of the a-Si:H and nc-Si:H layers affect depletion width, recombination, and electric field strength, and how these in turn shape the FF trend.
2. C2: Bandgap tuning – Modifying the bandgap of the absorbers to steer the photocurrent mismatch and study how this spectral redistribution influences FF and efficiency under controlled imbalance.
3. C3: Front contact design – Optimizing the TCO and antireflection coating (ARC) layers to improve optical coupling and spectral sharing between subcells, thereby tuning mismatch and FF

indirectly.

4. C4: Intermediate reflector integration – Using dielectric reflectors at the tunnel recombination junction to induce spectral steering and mild bottom limitation, activating the FF compensation mechanism.
5. C5: Light-induced degradation (LID) – Studying how defect formation in a-Si:H and nc-Si:H alters the FF compensation landscape and shifts the optimal thickness regime in stabilized devices.

Together, these case studies build a coherent picture of how FF compensation can be modulated through targeted optical and electrical design. Which will lead to practical design guidance in the device-level strategies proposed in Section 6.5.

C1: Absorber Thickness Engineering

The baseline tandem, which was calibrated in Section 4.4, with 300 nm a-Si:H and 3000 nm nc-Si:H was strongly top-limited ($\Delta J_{\mathrm{SC}} < 0$), resulting in moderate FF and efficiency. This is also visible in Figure 6.1 of Section 6.1, in which the efficiency and FF show low values at the given thickness. To remove this imbalance, the nc-Si:H bottom-cell thickness was fixed at 1500 nm, and the a-Si:H top-cell thickness was varied from 200 nm to 400 nm.

Table 6.1: Simulated tandem performance for varied a-Si:H top-cell thickness on a 1500 nm nc-Si:H bottom cell. $\Delta_{\mathrm{opt}} = J^{\mathrm{bot}}_{\mathrm{SC,opt}} - J^{\mathrm{top}}_{\mathrm{SC,opt}}$ (positive = bottom-limited, negative = top-limited). J_{SC} is the simulated tandem current.

a-Si:H [nm]	$J^{\mathrm{top}}_{\mathrm{SC,opt}}$	$J^{\mathrm{bot}}_{\mathrm{SC,opt}}$	Δ_{opt}	J_{SC}	V_{OC} [V]	FF [%]	η [%]
200	10.4	13.7	-3.3	10.7	1.398	78.77	11.76
250	11.1	12.9	-1.8	11.6	1.385	76.45	12.25
300	11.6	12.5	-0.9	11.9	1.375	74.12	12.13
350	12.2	12.1	–0.1	12.5	1.366	71.64	12.22
400	12.5	11.8	+0.7	12.4	1.355	70.72	11.85

Table 6.1 shows the simulated tandem performance as a function of a-Si:H top-cell thickness, paired with a 1500 nm nc-Si:H bottom cell. As the a-Si:H layer becomes thicker, the optical current in the top cell increases while the bottom-cell current decreases, gradually shifting the tandem from a strongly top-limited regime (e.g. 200 nm) toward current matching and eventually bottom-limited operation (e.g. 400 nm).

Despite this shift, the does not show the FF compensation effect as discussed in Section 6.2, but shows the behaviour shown in Section 6.1. FF decreases steadily with increasing a-Si:H thickness, regardless of whether the device is top- or bottom-limited. This indicates that mismatch compensation does not play a strong role here; rather, FF appears to be governed more by the electrical quality of the a-Si:H absorber itself.

As explained in Section 6.1, the observed FF trend can be explained by the physics of the a-Si:H junction. For thinner top cells (e.g. 200–250 nm), the depletion region spans a large portion—or even the full thickness—of the intrinsic layer. This enhances carrier collection, thus leading to less recombination, which translates into higher FF. As the top cell becomes thicker, a smaller fraction of the absorber is within the depletion region, leading to increased recombination losses and reduced FF.

Efficiency peaks around 250–300 nm, where the top cell is still thin enough to maintain strong electric fields and low recombination, while generating sufficient photocurrent. Beyond this point, although the top-cell thickness continues to increase, the additional optical absorption yields diminishing returns: the photocurrent begins to saturate and J_{SC} plateaus. Meanwhile, the fill factor steadily degrades due to reduced electric field strength and increased recombination in the thicker intrinsic layer. As a result, the efficiency no longer benefits from the added thickness, and instead begins to decline, marking the onset of the recombination-limited regime.

Figure 6.7 compares the evolution of fill factor and efficiency as a function of controlled current mismatch (Δ) for two optically matched tandems: a thin, field-dominated 350/1500 nm configuration and a thicker 425/3000 nm device. The thinner tandem shows a clearly pronounced FF compensation response:

FF reaches a minimum at exact current match ($\Delta = 0$) and recovers strongly under mild bottom-cell limitation ($\Delta > 0$).

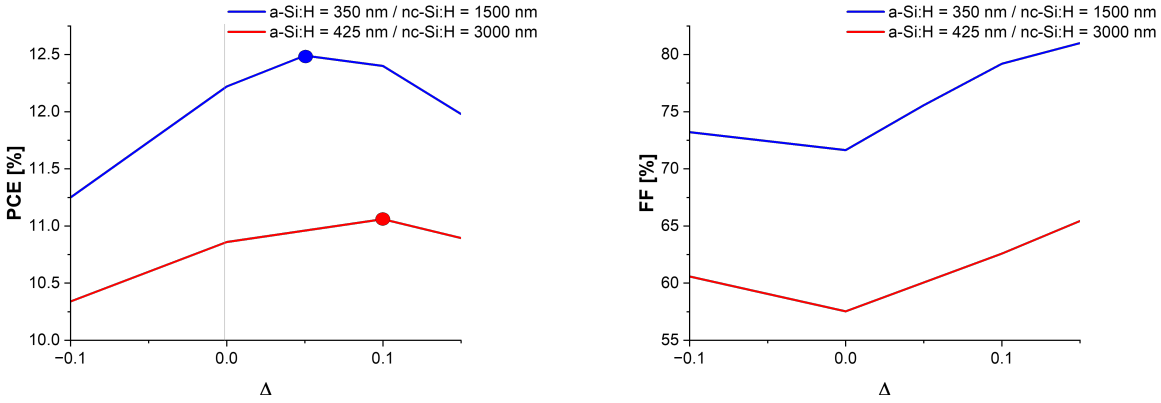

(a) Efficiency behaviour under current mismatch.

(b) Fill-factor behaviour under current mismatch.

Figure 6.7: Comparison of fill factor and efficiency behaviour as a function of current mismatch (Δ) for two optically matched tandems. The thinner, field-dominated 350/1500 nm device exhibits a strong FF compensation response and an efficiency peak near mild bottom limitation, while the thicker 425/2000 nm tandem shows suppressed recovery due to weaker electric-field-assisted transport.

This recovery reflects a redistribution of internal bias that allows the top cell to operate closer to its individual maximum power point once it is no longer current-limiting. The corresponding PCE peak is not only sharper but also reaches a higher absolute value (≈12.4%) compared to the thicker tandem (≈10.9%). This enhanced PCE originates from two coupled effects.

First, in the thin a-Si:H top cell, the electric field extends across nearly the entire intrinsic layer, enabling field-assisted carrier extraction and reducing recombination through tail states. Under mild mismatch, this strong field allows the surplus bias from the bottom cell to be effectively transferred to the top junction, maximizing the FF compensation effect.

Second, because the top and bottom absorbers are both relatively thin, the tandem experiences lower series resistance and reduced recombination losses, so improvements in FF directly translate into higher overall efficiency. In contrast, the thicker 425/2000 nm tandem exhibits both a lower PCE baseline and a flatter compensation response. The weaker electric field in the thicker a-Si:H absorber causes a larger portion of the intrinsic layer to be quasi-neutral, forcing carriers to rely on slow diffusion rather than drift.

As a result, additional voltage redistribution under mismatch cannot substantially improve charge extraction, and the FF recovery remains more modest. Consequently, both the magnitude and sharpness of the PCE peak are suppressed. Overall, the comparison highlights that strong field-assisted transport in thinner devices not only enhances the absolute efficiency but also amplifies the FF compensation effect. Thicker tandems, where drift fields weaken and recombination dominates, lose this self-correcting behavior and display flatter, recombination-limited performance profiles.

While the simulated bottom-cell thicknesses (1500–3000 nm) fall within the range of commonly implemented values in nc-Si:H technology, the top-cell thicknesses (350–425 nm) are somewhat above those typically used in high-efficiency devices. In practice, thinner a-Si:H layers (150–250 nm) are preferred to minimize recombination and light-induced degradation. However, the explored parameter space remains experimentally feasible and helps illustrate the impact of thickness on field strength, recombination, and FF compensation dynamics under controlled mismatch conditions.

C2: Bandgap Engineering Towards Controlled Mismatch

The effect of a-Si:H bandgap tuning was examined for 250 nm, 300 nm and 350 nm top-cell thicknesses, with the nc-Si:H bottom cell fixed at 1500 nm. Only the bandgap was modified (1.65–1.61 eV-1.57 eV), while all trap and transport parameters were kept constant. The results are summarized in Table 6.2.

Table 6.2: Simulated performance under a-Si:H bandgap variation for three top-cell thicknesses. $\Delta_{\mathrm{opt}} = J_{\mathrm{SC,opt}}^{\mathrm{bot}} - J_{\mathrm{SC,opt}}^{\mathrm{top}}$ (positive = bottom-limited, negative = top-limited). J_{SC} is determined by the limiting subcell.

a-Si:H [nm]	E_g [eV]	$J_{\mathrm{SC,opt}}^{\mathrm{top}}$	$J_{\mathrm{SC,opt}}^{\mathrm{bot}}$	Δ_{opt} [mA cm^{-2}]	J_{SC} [mA cm^{-2}]	V_{OC} [V]	FF [%]	η [%]
250	1.65	11.1	12.9	-1.8	11.6	1.385	76.45	12.25
	1.61	11.7	12.6	-0.9	12.1	1.347	75.40	12.32
	1.57	12.5	11.9	+0.5	12.5	1.309	75.04	12.27
300	1.65	11.6	12.5	-0.9	11.91	1.375	74.12	12.13
	1.61	12.3	12.1	+0.2	12.5	1.336	72.90	12.18
	1.57	13.1	11.4	+1.7	11.98	1.298	76.99	11.97
350	1.65	12.2	12.1	+0.1	12.5	1.366	71.64	12.22
	1.61	12.9	11.7	+1.2	12.3	1.328	74.76	12.18
	1.57	13.1	11.1	+2.0	11.6	1.290	78.43	11.74

The observed behavior under bandgap tuning can be understood in terms of the diode equation and the interplay between recombination and carrier extraction. Lowering the a-Si:H bandgap increases the absorption edge, thereby enhancing optical generation in the top cell. However, it also reduces the built-in potential and increases the intrinsic carrier concentration, which raises the saturation current density J_0. As shown in Equation (2.4), the open-circuit voltage V_{OC} depends logarithmically on the ratio J_{ph}/J_0. Therefore, an increase in J_0 leads to a reduction in V_{OC}, partially offsetting the gain in J_{SC}.

The fill-factor behavior aligns with expectations from the fill-factor compensation regime: near current matching ($\Delta_{\mathrm{opt}} \approx 0$), both subcells are forced to operate at a shared current level, which is offset from the optimal bias point of each. This bias misalignment increases recombination and reduces carrier extraction efficiency, leading to a drop in both voltage and FF. As mismatch increases, either in the top- or bottom-limited direction, one subcell approaches its individual MPP, resulting in a partial recovery of the tandem fill factor.

For the 250 nm device, all three bandgaps (1.65, 1.61, 1.57 eV) result in a top-limited tandem configuration. Here, reducing the bandgap reduces the mismatch (i.e., approaches current matching), which increases bias misalignment and thus leads to a decreasing FF. For the 300 nm device, the transition from top- to bottom-limited occurs across the scanned E_g range, with current matching reached near $E_g = 1.61$ eV. Accordingly, this case shows the characteristic FF dip near match, with recovery on either side. For the 350 nm structure, all configurations are bottom-limited, and decreasing the top-cell bandgap simply increases mismatch further. As a result, FF rises monotonically as E_g decreases, due to the top cell operating closer to its MPP. It should be noted, however, that the fill-factor compensation effect cannot be fully captured for all thicknesses within this sweep.

Efficiency exhibits a trade-off with the top-cell bandgap. For the 250 nm and 300 nm top cells, the highest efficiency occurs at the intermediate bandgap ($E_g = 1.61$ eV), where the modest gain in J_{SC} more than compensates for the slight reductions in V_{OC} and FF. At higher bandgap (1.65 eV), the photocurrent is limited despite a higher V_{OC}, while at lower bandgap (1.57 eV), the increase in current no longer offsets the stronger voltage loss. As a result, the product $J_{\mathrm{SC}}V_{\mathrm{OC}}$FF—and thus the efficiency—is maximized at the middle bandgap, confirming that optimal performance arises from a balance between optical gain and electrical loss.

In contrast, the 350 nm device shows a monotonic decline in efficiency as E_g decreases. Here, lowering the bandgap drives the tandem further into bottom-cell limitation ($\Delta_{\mathrm{opt}} > 0$), reducing the tandem current while V_{OC} simultaneously decreases due to increased recombination and higher J_0. Although FF improves slightly at lower E_g, this recovery is insufficient to compensate for the combined current and voltage losses, resulting in a net decrease in overall efficiency.

To explore this further, the effect of bottom-cell bandgap tuning was also examined using the 350 nm/1500 nm tandem configuration. The results can be seen in Table 6.3. Increasing $E_{g,\mathrm{bot}}$ by +0.15 eV slightly reduces the bottom-cell photocurrent, making the device more bottom-limited than before. However, the

increased bandgap also significantly suppresses the bottom-cell saturation current $J_{0,\mathrm{bot}}$, reducing recombination losses and resulting in a substantial gain in V_{OC} (96 mV). This also enables a modest FF increase, driven by both reduced recombination and a more favorable voltage biasing of the top cell.

Although the exact current matching point is not reached within the assessed parameter space, the additional mismatch strengthens the conditions for fill-factor compensation. Together, these effects result in a net efficiency gain of nearly 1 %, despite the small current penalty. This confirms that a moderate shift further into bottom-limited operation can be beneficial, provided the resulting recombination reduction outweighs the loss in photocurrent.

Table 6.3: Effect of increasing the nc-Si:H bottom-cell bandgap by +0.15 eV, relative to the 350/1500 nm baseline without ARC. Δ_{opt} is the optical current mismatch (positive = bottom-limited). Values in parentheses are changes with respect to the baseline.

Configuration	$J_{\mathrm{SC,opt}}^{\mathrm{top}}$	$J_{\mathrm{SC,opt}}^{\mathrm{bot}}$	Δ_{opt}	J_{SC} [mA cm^{-2}]	V_{OC} [V]	FF [%]	η [%]
Baseline	12.2	12.1	+0.1	12.49	1.366	71.64	12.22
$E_{g,\mathrm{bot}}$ +0.15 eV	12.1	11.8	+0.3	12.32 (-0.17)	1.462 (+0.096)	72.97 (+1.33)	13.14 (+0.92)

The effect of bandgap engineering differs across the three top-cell thicknesses due to their initial mismatch regimes. For the 250 nm device, all bandgaps fall in the top-limited regime. Here, lowering the bandgap reduces the mismatch, pushing the tandem closer to current match, this increases bias misalignment and leads to a decline in fill factor. The 300 nm device spans the transition from top-limited to bottom-limited, with $E_g = 1.61$ eV yielding near-current match and thus a characteristic FF dip. On either side of this point, FF improves as one subcell approaches its optimal bias. For the 350 nm case, the tandem is bottom-limited for all bandgaps. Reducing E_g further increases mismatch and enables the top cell to operate closer to its MPP, improving FF despite increased recombination. This demonstrates that FF compensation depends not only on absolute bandgap but on the mismatch context in which it is applied.

C3: Optical Optimization via TCO and ARC Stack

To improve optical coupling and fine-tune the current balance of the tandem, the front TCO stack was optimized by varying the IOH layer thickness and introducing a two-layer ARC. Simulations were performed for 250/1500 nm, 350/1500 nm and 400/1500 nm a-Si:H/nc-Si:H tandems under constant electrical parameters. The IOH thickness was varied between 70, 130, and 150 nm, and an MgF_2/SiN_x ARC was later added above the 130 nm configuration. The results are summarized in Table 6.4.

Table 6.4: Simulated tandem performance for different IOH thicknesses and ARC configurations. Δ_{opt} is the optical current mismatch (positive = bottom-limited). $J_{\mathrm{SC,opt}}^{\mathrm{top/bot}}$ are the optical subcell currents.

a-Si	Configuration	Δ_{opt} [mA cm^{-2}]	$J_{\mathrm{SC,opt}}^{\mathrm{top}}$	$J_{\mathrm{SC,opt}}^{\mathrm{bot}}$	J_{SC} [mA cm^{-2}]	V_{OC} [V]	FF [%]	η [%]
250 nm	IOH = 70 nm	-2.5	11.5	14.0	11.82	1.389	76.83	12.61
	IOH = 130 nm	-1.8	11.1	12.9	11.56	1.385	76.45	12.25
	IOH = 150 nm	-1.6	11.1	12.7	11.39	1.384	76.36	12.04
	IOH = 130 + ARC	-1.5	11.3	12.9	11.70	1.386	76.29	12.37
350 nm	IOH = 70 nm	-0.5	12.6	13.1	12.82	1.369	72.11	12.66
	IOH = 130 nm	+0.1	12.2	12.1	12.49	1.366	71.64	12.22
	IOH = 150 nm	+0.2	12.1	11.9	12.32	1.364	71.57	12.02
	IOH = 130 nm + ARC	+0.3	12.3	12.0	12.61	1.366	71.61	12.34
400 nm	IOH = 70 nm	+0.3	13.0	12.7	13.21	1.359	69.77	12.53
	IOH = 130 nm	+0.7	12.5	11.8	12.37	1.355	70.72	11.85
	IOH = 150 nm	+0.9	12.5	11.6	12.13	1.354	71.85	11.80
	IOH = 130 nm + ARC	+1.1	12.7	11.6	12.20	1.355	72.72	11.95

The behavior of the FF across the different top-cell (a-Si:H) thicknesses aligns well with the expected compensation trend shown in Figure 6.4 in Section 6.2. Specifically, FF reaches a minimum near zero

optical current mismatch ($\Delta_{\mathrm{opt}} \approx 0$) and increases as the device becomes either top- or bottom-limited. This confirms that FF is strongly influenced by current mismatch and benefits from compensation effects as predicted in controlled studies.

The combined influence of optical mismatch and efficiency is summarized illustratively in Figure 6.8. The thinner IOH configuration enhances total absorption and improves PCE, even though it drives the tandem further away from perfect current matching. The thicker IOH yields better optical balance but lower overall generation, resulting in reduced efficiency.

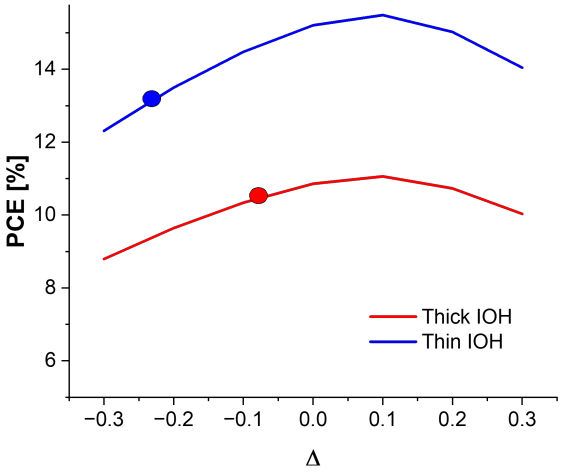

Figure 6.8: Simulated efficiency (PCE) as a function of optical current mismatch (Δ_{opt}) for tandem cells with thin and thick IOH layers. The thinner IOH increases total optical generation, leading to higher overall efficiency despite larger mismatch. The thicker IOH provides improved current balance but reduced PCE due to lower optical transmission.

For the 250 nm top cell, all IOH configurations are clearly top-limited. As expected, FF increases with increasing mismatch. For the 350 nm top cell, the device transitions from top-limited to bottom-limited across the different IOH configurations, with FF showing a shallow minimum close to $\Delta_{\mathrm{opt}} = 0$. For the 400 nm top cell, all configurations are bottom-limited, and FF again rises with increasing mismatch.

Although FF behavior is dominated by mismatch compensation, the efficiency trend is governed primarily by optical generation. Across all top-cell thicknesses, the thinnest IOH (70 nm) configuration provides the highest total photocurrent in both subcells. While this thinner TCO increases the mismatch (i.e., drives the tandem further from current balance), the overall generated current is higher. Consequently, the maximum efficiency is achieved not at perfect current matching but under conditions of mild mismatch where optical absorption is strongest. This highlights that maximizing generation in the limiting subcell can yield superior tandem efficiency, even when optical currents are not precisely balanced.

Although varying the IOH thickness modified the optical interference pattern and slightly adjusted the current balance between the subcells, the effect was not ideal. Thinner IOH layers enhanced overall photon absorption but increased current mismatch, while thicker layers reduced total absorption despite slightly improving balance. This indicates that IOH thickness alone cannot simultaneously optimize transparency and optical matching; combined optimization with the antireflection coating and front interface design is necessary for ideal optical coupling.

C4: Intermediate Reflector for Optical Mismatch Control

In monolithic tandem solar cells, an intermediate reflector (IR) layer (using materials like SiO_x, ZnO:Al, or µc-SiO_x:H) is strategically placed at the TRJ to modify the optical field distribution within the stack [37]. An intermediate reflector functions to redistribute and confine light within the device, thereby promoting more effective utilization of the incident spectrum.

Importantly, this spectral steering does not increase the total current of the tandem device. Instead, it shifts the current-limiting subcell. Specifically, the IR enhances the top-cell optical current density ($J_{\mathrm{SC,top}}$) by around 0.5–1.0 mA cm^{-2} and reduces $J_{\mathrm{SC,bot}}$ by a similar amount, keeping the total J_{SC} nearly unchanged [76, 61]. However, this shift can move the tandem from a top-limited configuration into a slightly bottom-limited regime—precisely the condition where FF compensation becomes active and beneficial.

The physical mechanism behind FF compensation lies in the way the total voltage is distributed between the two subcells. When the tandem is top-limited, the top cell is forced to operate at a higher voltage than its own MPP, leading to increased recombination, as already explained in Section 6.3. Shifting toward mild bottom limitation allows the top cell to operate closer to its optimal voltage, reducing recombination losses and improving alignment of the individual J–V characteristics. The result is an increase in both $V_{\mathrm{mpp}}/V_{\mathrm{OC}}$ and $J_{\mathrm{mpp}}/J_{\mathrm{SC}}$, leading to a higher FF, even if the overall current remains the same.

The optical gains provided by the IR should not compromise electrical performance; located at the TRJ, it must remain sufficiently transparent to enable carrier tunneling. Continuous or overly thick dielectric layers can impede charge transport, introduce series resistance, and lead to s-shaped J–V curves. To avoid this, IRs are often realized using patterned structures such as porous SiO_2 nanoparticle layers, which allow vertical current flow through localized openings while still providing strong optical interference effects [37].

Niesen et al. (Figure 6.9) showed that adding a SiO_2 nanoparticle IR increases the top-cell current and slightly reduces the bottom-cell current, shifting the tandem from top- to bottom-limited operation, with minimal change in total J_{SC}. The thin IR aligns with the FF compensation point, giving the highest efficiency. In contrast, a thicker IR introduces excessive mismatch, reducing efficiency slightly despite a further FF increase.

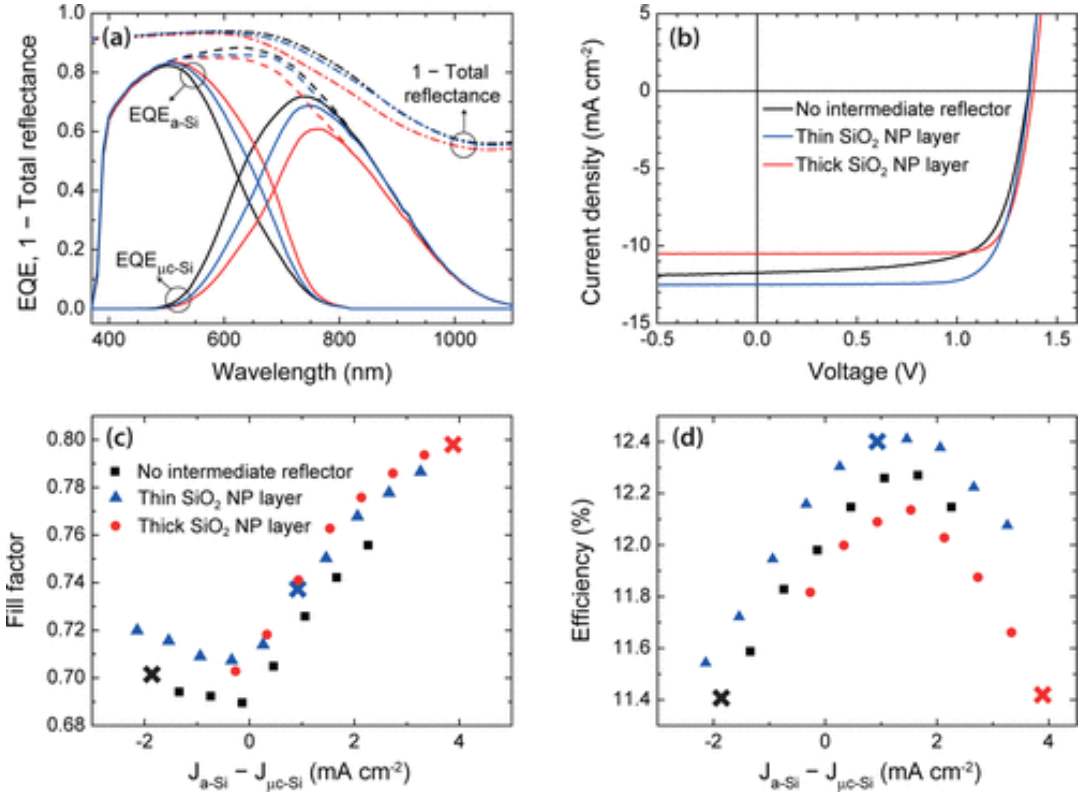

Figure 6.9: Effect of an intermediate reflector (IR) on optical and electrical performance of a-Si:H/nc-Si:H tandem solar cells. A SiO_2 nanoparticle IR increases top-cell current while reducing bottom-cell current, improving FF and efficiency. Adapted from [37].

In summary, an intermediate reflector is not merely an optical design element, it is a critical tool for

managing the electrical operating point of tandem devices. By optically tuning the current mismatch toward mild bottom limitation, the IR enables the top cell to operate under more favorable biasing conditions, activating the FF compensation effect and increasing efficiency. For optimal results, the IR must be thin, optically effective, and electrically non-blocking, preserving quasi-Fermi level continuity while reshaping the internal light field.

C5: FF Compensation in Stabilized Tandems

This section extends the FF compensation framework from the as-deposited device state (i.e., before light soaking) to the stabilized regime, addressing two key questions: (i) how the position of the efficiency maximum $\eta(\Delta)$ shifts after light-induced degradation (LID), and (ii) which absorber thickness combinations yield optimal performance post-degradation. As before, $\Delta > 0$ denotes bottom-limited operation and $\Delta < 0$ top-limited, using the convention from Section 6.2, where $\Delta J_{\mathrm{SC}} \equiv J_{\mathrm{SC,top}} - J_{\mathrm{SC,bot}}$.

LID was modeled by increasing the dangling bond density in the a-Si:H layer from 8×10^{15} to 4×10^{16} cm^{-3}, consistent with typical Staebler–Wronski degradation observed after ∼1000 hours of one-sun AM1.5 illumination at 50 °C [58]. Figure 6.10 shows how subcell degradation affects the shape and location of the $\eta(\Delta)$ peak. Three cases are shown: (i) the as-deposited state, (ii) degradation applied only to the a-Si:H top cell, and (iii) degradation applied to the nc-Si:H bottom cell.

Top-cell degradation shifts the efficiency peak toward the bottom-limited regime ($\Delta > 0$), indicating that the current-matched condition leads to stronger recombination losses in the top junction. In contrast, bottom-cell degradation shifts the optimum toward top-limited conditions ($\Delta < 0$), as the bottom junction becomes the dominant recombination bottleneck. All three simulations use a 425 nm a-Si:H / 2.0 µm nc-Si:H stack to isolate the electrical effects of degradation from optical mismatch.

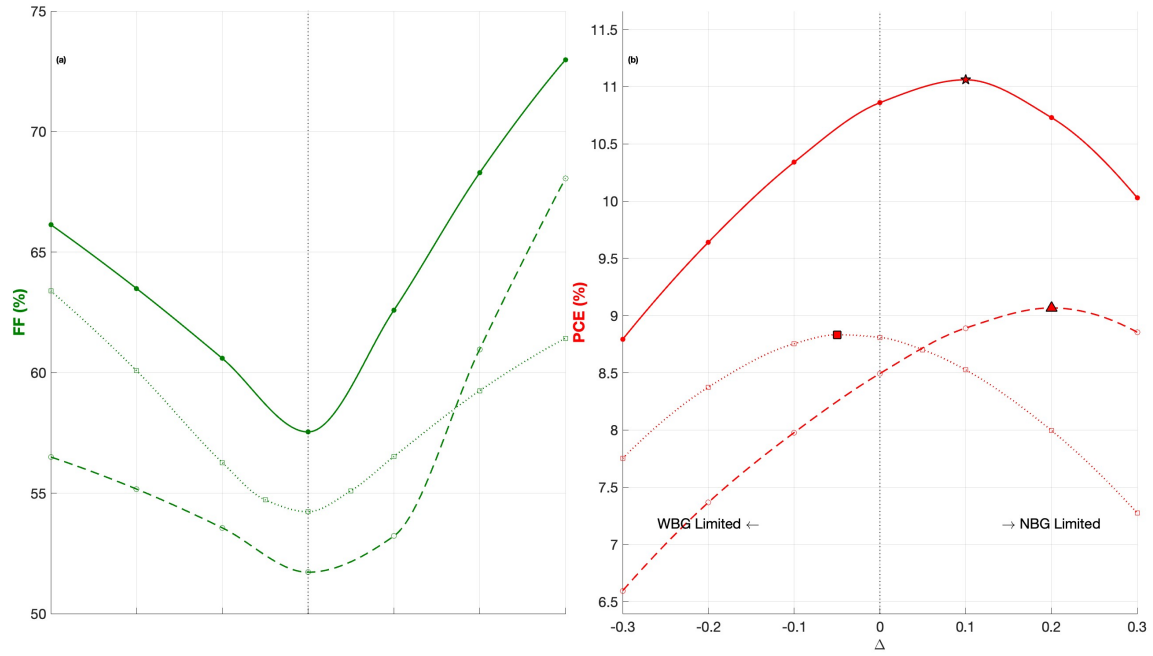

Figure 6.10: Effect of subcell degradation on $\eta(\Delta)$. Top-cell degradation shifts the efficiency peak toward the bottom-limited regime ($\Delta > 0$), whereas increased bottom-cell defect density shifts it toward top limitation ($\Delta < 0$).

To identify optimal absorber configurations after LID, a full thickness sweep was performed under degraded conditions. Figure 6.11 maps J_{SC}, V_{OC}, FF, and efficiency as functions of a-Si:H and nc-Si:H thickness. Degradation was applied to the top cell only, as a-Si:H is the layer most strongly affected by light soaking.

Three major trends emerge from the stabilization analysis: J_{SC} rises monotonically with absorber thickness in both subcells, but thicker devices suffer from enhanced recombination and weaker electric fields, leading to lower stabilized η. The highest J_{SC} values ($d_{a\text{-Si}} > 280$ nm, $d_{nc\text{-Si}} > 1.5$ µm) corre-

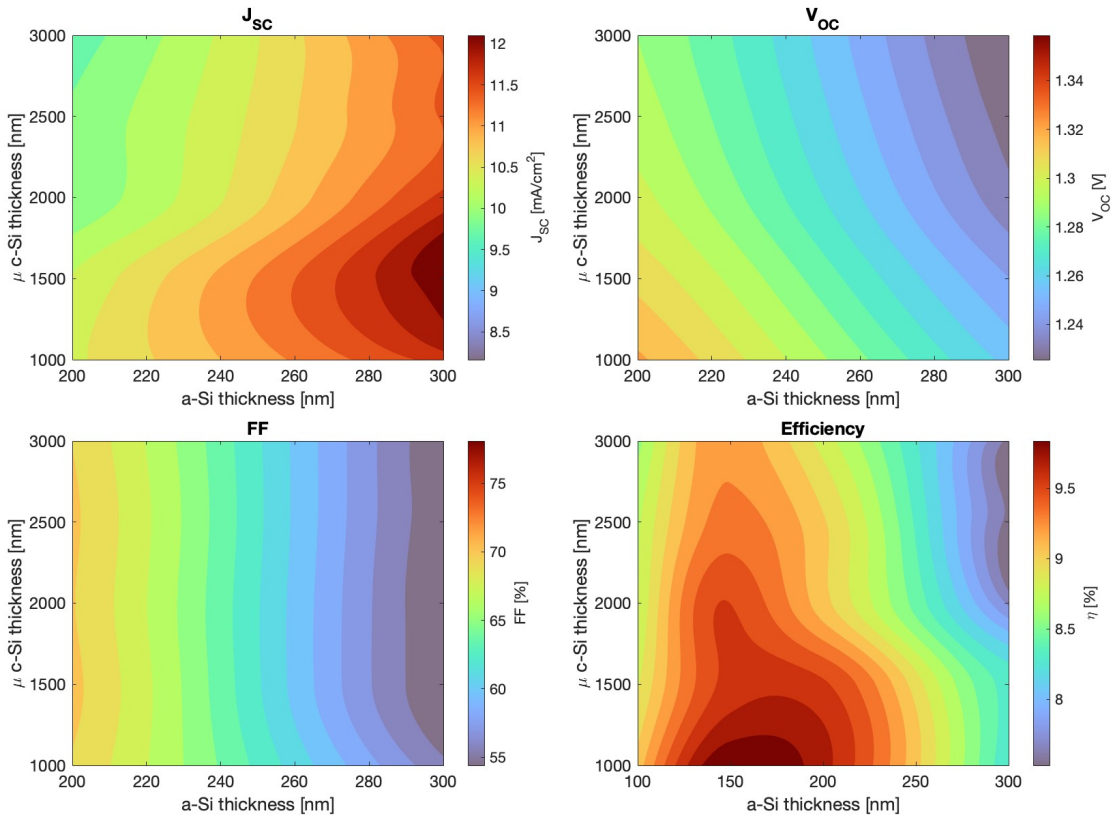

Figure 6.11: Post-LID thickness sweep showing stabilized efficiency as a function of a-Si:H and nc-Si:H absorber thicknesses. The highest efficiency is achieved for thin a-Si:H (150–200 nm) and moderate nc-Si:H (1.0–1.5 µm), balancing absorption and recombination losses.

spond to the low FF and and poor stability. The V_{OC} declines slightly with increasing layer thickness due to higher bulk defect density and carrier recombination, consistent with a reduction in the effective quasi-Fermi level splitting. And lastly, the FF shows the strongest dependence on a-Si:H thickness. Thin top cells (150–200 nm) remain nearly fully depleted even after LID and maintain efficient carrier collection, while thicker absorbers transition to diffusion-limited transport, resulting in a pronounced FF drop. Consequently, the η peak shifts toward thinner top cells.

The highest stabilized efficiencies are therefore obtained for top absorbers in the 150–200 nm range and bottom absorbers around 1000–1500 nm. This configuration preserves sufficient photocurrent while minimizing recombination and maintaining an electric field strong enough to support the compensation mechanism post-LID.

These findings are consistent with experimental observations. Early a-Si:H/nc-Si:H tandems typically employed 200–300 nm a-Si:H and 1–2 µm nc-Si:H absorbers [58], whereas more recent stabilized designs favor thinner a-Si:H layers ($\sim$150 nm) combined with nc-Si:H absorbers in the 1.0–1.5 µm range [9]. The simulated optimum thickness regime thus reproduces the experimentally established trade-off between stability, absorption, and FF compensation.

6.5. Design Rules for Stabilized a-Si:H/nc-Si:H Tandems

The following design rules summarize key strategies for optimizing the performance of a-Si:H/nc-Si:H tandem solar cells in the stabilized state, where the a-Si:H top junction becomes strongly current-limiting due to LID. In this regime, the FF compensation effect does not occur naturally and must be intentionally activated by shifting the tandem toward mild bottom limitation. The goal is to achieve peak PCE by leveraging structural, optical, and electronic design. For each rule, the case study connected to it is noted in the title.

Rule 1: Use Thin Absorbers to Preserve Field-Driven Transport (C1, C5)

Maintaining thin absorber layers is crucial to preserve strong internal electric fields and minimize recombination, particularly in the degraded a-Si:H top cell. Ensuring drift-dominated carrier transport is a prerequisite for achieving high FFs and enabling the compensation effect. In practice, the a-Si:H top cell should remain thin, typically between 150 and 200 nm, to ensure full depletion and suppress recombination losses, which is especially important after LID. The nc-Si:H bottom cell should also avoid thicknesses beyond 1.5–1.8 µm. Values in the 1.0–1.5 µm range maintain efficient collection while shifting the tandem slightly toward bottom limitation. In devices not subjected to LID, thicker top cells (up to 250–300 nm) can still operate in a field-dominated regime. However, preserving the electric field becomes increasingly critical after degradation.

Rule 2: Apply Bandgap Engineering to Shift Toward Bottom Limitation (C2, C5)

Bandgap tuning provides a powerful lever to rebalance current generation between the two subcells and move the tandem from strong top limitation into the FF compensation regime. Narrowing the a-Si:H bandgap (e.g., from 1.65 to 1.57–1.60 eV) increases red absorption in the top subcell, boosting its short-circuit current density J_{SC} and partially compensating for photocurrent losses caused by light-induced defect formation. However, this comes at the cost of a reduced built-in voltage, which increases recombination and lowers the open-circuit voltage V_{OC} due to an increase in the saturation current density J_0.

Conversely, slightly increasing the bandgap of the nc-Si:H bottom cell (by about +0.10–0.15 eV) reduces its J_{SC} marginally but significantly suppresses recombination, leading to an increase in V_{OC}. These complementary shifts help bring the tandem into mild bottom limitation—an operating point where the top cell moves closer to its individual maximum power point and FF compensation becomes active. In devices already close to current matching, however, such bandgap adjustments may degrade performance, and purely optical tuning is often more appropriate to avoid unnecessary voltage penalties or current imbalance.

Rule 3: Use Optical Design to Raise Current—Especially in the Top Cell (C3)

Effective light management is essential for maximizing current generation in tandem solar cells, particularly once the top cell has degraded. Optical strategies such as ARC, front surface texturing, and TCOs can increase the photogenerated current J_{SC} in both subcells, but are especially impactful for the a-Si:H top cell, where photocurrent recovery is critical after degradation.

Broadband ARCs, such as TiO_2/SiN_x multilayers, reduce front reflection losses across the solar spectrum and improve light incoupling. Moderate front surface texture further enhances absorption without disrupting the internal electric field. Additionally, high-transparency TCOs (e.g., IOH or ITO) with low parasitic absorption ensure minimal optical losses while maintaining good electrical contact. Paired with wide-bandgap or graded p-layers (e.g., a-SiC:H/a-SiO_x:H), these structures support strong band bending and suppress recombination at the front interface.

Together, these optical improvements raise the top-cell current and can gently shift the tandem from a top-limited configuration toward mild bottom limitation. This transition brings the top cell closer to its maximum power point, activates the FF compensation effect, and enables a moderate efficiency gain—without requiring changes to the electronic structure.

Rule 4: Use Intermediate Reflectors to Fine-Tune Spectral Sharing (C4)

IRs provide a passive yet powerful method to redistribute light within tandem solar cells, enabling precise control over current mismatch without modifying the electronic structure. Positioned at the TRJ, these layers (typically made of low-refractive-index materials like SiO_2 or ZnO nanostructures) create constructive interference that enhances light absorption in the top cell while slightly reducing the bottom-cell photocurrent.

This spectral shift does not significantly alter the total tandem J_{SC}, but it changes which subcell limits the current. In stabilized tandems, where the top cell is typically current-limiting due to degradation, this shift toward mild bottom limitation is advantageous. It allows the top cell to operate closer to its optimal bias, reducing recombination and enabling fill-factor compensation. As a result, both FF and

overall efficiency can improve, even if the generated current remains unchanged.

To preserve electrical performance, the IR must remain transparent to carrier transport. Continuous dielectric layers can introduce series resistance or block tunneling, which degrades performance. Instead, porous or nanostructured IRs (e.g., SiO_2 nanoparticle layers) allow vertical charge flow while preserving the optical benefits. These structures are especially valuable in the post-LID regime, where few other tuning strategies remain effective.

Rule 5: Ensure an Ohmic, Transparent TRJ

The TRJ plays a critical role in tandem devices by connecting the two subcells both electrically and optically. To enable efficient carrier recombination and preserve overall performance, the TRJ must be electrically ohmic and optically transparent. Electrically, this requires heavily doped p^+/n^+ layers (typically $> 10^{19}$ cm^{-3}) to support band-to-band tunneling and eliminate barriers to vertical current flow. If the TRJ is too resistive or thick, it can introduce recombination bottlenecks or lead to S-shaped J–V curves, severely reducing FF and efficiency.

Optically, the TRJ must minimize parasitic absorption. This can be achieved using thin, wide-bandgap layers or carefully selected TCO spacers that preserve light transmission across the junction. Importantly, the TRJ must also support smooth bias distribution between the subcells. Fill-factor compensation relies on the ability of the tandem to redistribute voltage dynamically in response to current mismatch. If the TRJ impedes this redistribution, either by introducing resistance or blocking tunneling, the compensation effect is suppressed, regardless of other optimizations. A properly designed TRJ is therefore essential not only for baseline performance but also for unlocking the self-correcting behavior that underpins FF recovery in current-mismatched tandems.

Summary

These rules provide a design framework for accessing the FF compensation regime and maximizing stabilized efficiency in a-Si:H/nc-Si:H tandems. Because light-induced degradation drives the top cell toward strong current limitation, the entire structure must be engineered to shift the tandem into mild bottom-limited operation. Once in this regime, FF recovers and overall power output improves.

Thin absorber layers and a well-functioning tunnel recombination junction are the most fundamental requirements for achieving high efficiencies in stabilized a-Si:H/nc-Si:H tandems. A thin a-Si:H top cell ensures strong electric fields and low recombination, while the TRJ must allow efficient carrier recombination without introducing electrical or optical barriers.

The other strategies—bandgap tuning, optical front-end design, and intermediate reflectors—become important depending on the degree of current mismatch after light-induced degradation. If the tandem remains strongly top-limited, bandgap engineering is the most effective way to restore balance. If mismatch is already moderate, optical tools such as anti reflection coatings or intermediate reflectors can fine-tune spectral sharing to reach the compensation regime with minimal electrical trade-offs.

6.6. Comparison of Design Rules: a-Si:H/nc-Si:H vs. Perovskite Tandems

While the design rules developed in this work focus on a-Si:H/nc-Si:H tandem cells, especially in the stabilized (post-LID) state, they do not universally translate to all tandem architectures. In particular, perovskite tandems differ in several key aspects that alter the relevance and direction of FF compensation and current mismatch engineering.

Perovskite–perovskite tandems exhibit more symmetric material quality: both subcells typically have high carrier lifetimes, strong built-in fields, and low bulk recombination. As shown in Figure 6.5 in Section 6.2.2, FF compensation still occurs under mismatch, but the effect is more modest, and the efficiency maximum remains near current match. This is because neither subcell suffers from strong recombination losses at match, unlike in a-Si:H/nc-Si:H tandems, where the a-Si:H top cell becomes increasingly defective and limiting after light-induced degradation.

As a result, the design strategy diverges:

- For a-Si:H/nc-Si:H tandems, especially post-LID, the top cell is inherently limiting. Design rules

are tailored to shift the tandem into mild bottom limitation, where FF compensation emerges and peak efficiency occurs. This requires thinning the top absorber, widening the bottom gap, and using optics selectively to rebalance currents without weakening the top-cell field.

- For perovskite–perovskite tandems, both subcells typically operate close to their maximum power point near current match. However, the absolute efficiency maximum may still occur under slight current mismatch—often in the bottom-limited regime—due to mild FF compensation effects. Here, design rules emphasize precise current balancing and optical optimization, as compensation plays a more limited role compared to silicon-based tandems.

In summary, FF compensation is a useful design lever in both tandem types, but its role and strength differ. In silicon-based tandems, it compensates for intrinsic material weaknesses; in perovskite tandems, it offers marginal improvements around an already optimal current match. Therefore, mismatch engineering and thickness/bandgap optimization must be tailored to the recombination characteristics and degradation behavior of each tandem system.

7

Conclusion

This work presented a comprehensive numerical investigation of thin-film silicon and hybrid tandem solar cells using physics-based TCAD modeling, optical simulations, and parametric analysis. The study progressed from the calibration of a single-junction a-Si:H/nc-Si:H model to the exploration of flexible perovskite–silicon hybrid architectures, ending in a detailed FF compensation analysis establishing design rules for stabilized tandem operation.

Model calibration and validation

In Chapter 3, an opto-electrical simulation framework for the a-Si:H/nc-Si:H tandem solar cell was established and calibrated against experimentally reported device data. The modeling approach employed two independently validated single-junction models: an a-Si:H p-i-n top cell and an nc-Si:H p-i-n bottom cell. Each subcell incorporated exponential and Gaussian trap distributions to represent tail and deep defect states, accurately capturing recombination and carrier transport behavior. Spectrally resolved optical generation profiles were imported from GENPRO4, enabling wavelength-dependent photon absorption to be consistently coupled with the electrical simulation in Sentaurus TCAD.

Electrical calibration was performed first at the single-junction level, iteratively adjusting parameters such as Urbach energy, defect density, and carrier mobilities to reproduce measured V_{OC}, J_{SC}, and fill factor values. The resulting models closely matched experimental J–V characteristics for both subcells, confirming the validity of the optical–electrical coupling and defect parametrization. The two subcells were then integrated into a monolithic tandem configuration, connected via a tunnel recombination junction. Band-to-band tunneling was implemented through non-local tunneling. This approach ensured current continuity and realistic potential alignment between the subcells. The final calibrated tandem reproduced the experimental a-Si:H/nc-Si:H tandem reference with good agreement, yielding $V_{\mathrm{OC}} = 1.34$ V, $J_{\mathrm{SC}} = 11.69$ mA cm^{-2}, $\mathrm{FF} = 58.46\%$, and $\eta = 9.17\%$, closely matching the measured values of $V_{\mathrm{OC}} = 1.35$ V, $J_{\mathrm{SC}} = 11.65$ mA cm^{-2}, $\mathrm{FF} = 58.22\%$, and $\eta = 9.16\%$. This agreement validates the physical consistency of the model and confirms its ability to reproduce key device trends, providing a robust baseline for subsequent flexible and hybrid tandem investigations.

Transition to flexible and hybrid architectures

The first extension of the model described in Chapter 3 involved adapting the validated a-Si:H/nc-Si:H tandem to a flexible substrate representative of roll-to-roll compatible thin-film modules. The flexible device preserved the same calibrated layer stack and interface sequence as the rigid Asahi reference but was reinterpreted for a mechanically compliant configuration. Such architectures are well suited for lightweight and scalable fabrication; however, the simulations revealed that their achievable efficiency remains limited to around 10%, primarily due to defect-assisted recombination in the disordered amorphous top cell and weak near-infrared absorption in the nc-Si:H bottom cell.

These intrinsic limitations of silicon-based thin films confirm the need for alternative absorber materials that combine strong optical absorption with superior electronic quality. Perovskite materials address

these limitations by offering high absorption coefficients, long carrier diffusion lengths, and tunable bandgaps suitable for multi-junction integration. In this work, single-junction perovskite simulations were performed using a range of hole-transport layers (HTLs) to analyze band alignment and interfacial selectivity. Both organic (e.g., PEDOT:PSS, PTAA) and inorganic (e.g., NiO_x, nc-SiO_x) HTLs were examined for their influence on energy band offsets, carrier extraction, and long-term stability. Among these, PTAA and NiO_x configurations achieved comparable power conversion efficiencies around 22%, confirming that both organic and inorganic HTLs can support high-performance single-junction operation when properly aligned with the perovskite absorber. However, NiO_x offers superior thermal and chemical stability compared to organic HTLs, making it a strong candidate for reliable and flexible perovskite devices. Furthermore, the use of inorganic HTLs such as NiO_x or nc-SiO_x aligns with the long-term objective of developing stable tandem architectures where interfacial and environmental robustness are critical.

Extending the framework to a hybrid a-Si:H/perovskite tandem yielded efficiencies near 16%, already surpassing the calibrated a-Si:H/nc-Si:H reference while maintaining mechanical and chemical protection through the amorphous-silicon top layer. This hybrid configuration thus represents a promising transitional solution if perovskite stability challenges remain unresolved, as the a-Si:H layer provides inherent environmental shielding. In contrast, once material and interface stability in perovskite absorbers is achieved, fully perovskite–perovskite (PVK/PVK) tandems become the preferred route. The simulated PVK/PVK device reached efficiencies around 29%, confirming that fully inorganic or nc-SiO_x(p)-based contacts can deliver high performance without compromising optical or electrical selectivity.

FF compensation and design rules

In Chapter 6 the phenomenon of fill factor compensation in monolithic tandem solar cells through both numerical experiments and targeted parametric studies was systematically investigated. Using the validated a-Si:H/nc-Si:H framework, the analysis revealed that the efficiency maximum of a tandem device does not necessarily coincide with the point of perfect current matching, but rather with a condition of mild current imbalance—typically in the bottom-limited regime. This offset arises because the current-surplus subcell operates at a higher forward bias, redistributing internal voltage in a way that enhances the overall fill factor and partially compensates for the current loss.

In a-Si:H/nc-Si:H tandems, thin, field-dominated a-Si:H absorbers (150–250 nm) exhibit higher FF due to stronger internal electric fields and more efficient carrier collection. Controlled bandgap tuning—through slight narrowing of the a-Si:H top cell or widening of the nc-Si:H bottom cell—can shift operation toward mild bottom limitation, activating a small but beneficial FF compensation regime. Optical adjustments, such as TCO or ARC optimization, further refine current balance without degrading transport.

After light-induced degradation, the optimal configuration shifts toward thinner top cells, maintaining strong fields and enabling partial FF recovery. In contrast, perovskite tandems show only weak compensation effects because both subcells exhibit comparable recombination and transport properties.

Overall, the FF compensation analysis highlights the interplay between optical balance, field distribution, and recombination dynamics in determining tandem stability. The derived design rules—thin, high-field absorbers, controlled bandgap asymmetry, optimized optical coupling, and transparent recombination junctions—provide a general framework for achieving efficient and self-stabilizing operation in silicon-based tandems.

Outlook

The validated simulation framework developed in this work provides a solid foundation for future investigations into advanced thin-film and hybrid tandem solar cells. Several promising research directions can be identified to further extend the physical understanding and practical relevance of the present results.

A next step is to extend the present two-junction a-Si:H/nc-Si:H and perovskite–perovskite designs toward triple-junction configurations such as a-Si:H/PVK/PVK. In such architectures, the wide-bandgap a-Si:H top cell would again serve a dual purpose: acting as a stable UV-absorbing and encapsulating layer that protects the underlying perovskite stack from moisture and photo-oxidation, while contribut-

ing to spectral utilization in the blue region. The combination of this protective silicon layer with two high-quality perovskite absorbers—each capable of delivering large open-circuit voltages—promises power conversion efficiencies exceeding shown in this study for the hybrid stack. Achieving this will require refined spectral coupling and an accurate description of multiple tunnel recombination junctions to maintain current continuity and optimize the overall voltage build-up across the triple-junction device.

Further refinement of the perovskite model is also called for. The present simulations employ simplified representations of recombination via only surface recombination velocities and carrier lifetimes. Incorporating detailed defect-state distributions, ion migration, and interfacial dipole formation would enable a more realistic description of hysteresis, degradation, and long-term stability. Such improvements would allow the framework to predict not only accurate initial efficiency but also performance evolution under operational stress.

Experimental validation of the simulated nc-SiO_x(p) contact layers represents another key opportunity. Their predicted combination of high transparency, selective hole extraction, and chemical robustness makes them strong candidates for stable perovskite-based tandems. Investigating their deposition, doping, and interface chemistry in real perovskite devices could confirm their suitability as inorganic HTLs in both hybrid and all-perovskite configurations.

Future work should aim to establish quantitative design rules that link the strength of fill factor compensation to fundamental material and interface parameters. By systematically varying quantities such as defect density, carrier lifetime, and interface recombination velocity in simulation, it would be possible to derive predictive scaling relations connecting recombination dynamics with the position and magnitude of the efficiency peak under current mismatch. Such an approach would allow the compensation effect to be described not only qualitatively but quantitatively, clarifying how it evolves across different material systems—from defect-dominated a-Si:H/nc-Si:H tandems to high-quality perovskite architectures. These insights would ultimately enable device-specific optimization, where the degree of intentional mismatch and the operating point are tailored according to the dominant recombination mechanisms in each subcell.

Together, these directions outline a clear roadmap from the present calibrated framework toward predictive, experimentally validated models of next-generation multi-junction solar cells. Through continued refinement of material physics, interface modeling, and tandem architecture design, the simulation approach developed in this work can play a central role in guiding the realization of flexible, high-efficiency photovoltaic technologies.

References

[1] Aimi Abass. “Light absorption enhancement and electronic properties of thin-film solar cells”. PhD Thesis. KU Leuven, 2014. url: https://www.researchgate.net/publication/292349306.

[2] Mohammad Ishaq Alkhatab. “Material Studies for Flexible 3rd Generation Solar Cells”. Figure adapted from thesis. Ph.D. thesis. Université de Lille, 2020. url: https://www.researchgate.net/publication/359611658_Material_studies_for_flexible_3rd_generation_solar_cells.

[3] Guilherme Almeida et al. “Perovskite–Silicon Tandem Solar Cells: Pathways to Commercialization”. In: *Nature Energy* 8.5 (2023), pp. 434–447. doi: 10.1038/s41560-023-01254-9.

[4] P. W. Anderson. “Absence of Diffusion in Certain Random Lattices”. In: *Physical Review* 109.5 (1958), pp. 1492–1505. doi: 10.1103/PhysRev.109.1492.

[5] K. M. Anoop and T. N. Ahipa. “Recent advancements in the hole transporting layers of perovskite solar cells”. In: *Solar Energy* 263 (2023), p. 111937. issn: 0038-092X. doi: 10.1016/j.solener.2023.111937.

[6] J. Arayro, R. Mezher, and H. Sabbah. “Comparative Simulation Study of the Performance of Conventional and Inverted Hybrid Tin-Based Perovskite Solar Cells”. In: *Coatings* 13.7 (2023), p. 1258. doi: 10.3390/coatings13071258.

[7] Pradeep Bajpai, R. P. Yadav, and Shilpi Yadav. “Electronic properties of amorphous silicon and effect of hydrogenation: A review”. In: *Journal of Materials Science: Materials in Electronics* 32 (2021), pp. 13766–13784. doi: 10.1007/s10854-021-05614-1.

[8] Yining Bao et al. “Insights into efficiency deviation from current-mismatch for tandem photovoltaics”. In: *Nano Energy* 120 (2024), p. 109165. doi: 10.1016/j.nanoen.2023.109165.

[9] M. Bonnet-Eymard et al. “Optimized short-circuit current mismatch in multi-junction solar cells”. In: *Solar Energy Materials and Solar Cells* 117 (2013), pp. 120–125. doi: 10.1016/j.solmat.2013.05.046.

[10] A. F. Bouhdjar et al. “Performance Study of the Micromorph Silicon Tandem Solar Cell Using Silvaco TCAD Simulator”. In: *Transactions on Electrical and Electronic Materials* 20.6 (2019), pp. 494–512. doi: 10.1007/s42341-019-00136-4.

[11] A. F. Bouhdjar et al. “Performance Study of the Micromorph Silicon Tandem Solar Cell Using Silvaco TCAD Simulator”. en. In: *Transactions on Electrical and Electronic Materials* 20.6 (Dec. 2019), pp. 494–512. issn: 1229-7607, 2092-7592. doi: 10.1007/s42341-019-00136-4. url: http://link.springer.com/10.1007/s42341-019-00136-4 (visited on 03/07/2025).

[12] R. W. Collins, A. S. Ferlauto, and C. R. Wronski. “Evolution of Microstructure and Optical Properties in Amorphous and Microcrystalline Silicon Thin Films”. In: *Solar Energy Materials and Solar Cells* 78.1-4 (2003), pp. 143–180. doi: 10.1016/S0927-0248(02)00348-4.

[13] Kaining Ding et al. “Characterization and simulation of a-Si:H/µc-Si:H tandem solar cells”. In: *Solar Energy Materials and Solar Cells* 95.12 (2011), pp. 3318–3327. doi: 10.1016/j.solmat.2011.07.023.

[14] D. Fischer et al. “The ”Micromorph” Solar Cell: Extending a-Si:H Technology Towards Thin Film Crystalline Silicon”. In: *Solar Energy Materials and Solar Cells* 41–42 (1996). Institut de Microtechnique, Université de Neuchâtel and Siemens Solar, pp. 425–436. doi: 10.1016/0927-0248(95)00166-2.

[15] C. Frisk et al. “Optimizing Ga-profiles for highly efficient Cu(In,Ga)Se2 thin film solar cells in simple and complex defect models”. In: *Journal of Physics D: Applied Physics* 47.48 (2014), p. 485104. doi: 10.1088/0022-3727/47/48/485104.

[16] H. P. Garg and J. Prakash. *Solar Energy: Fundamentals and Applications*. 1st. Accessed: 2025-02-26. New Delhi, India: Tata McGraw-Hill Education, 2000. isbn: 9780074516107.

[17] R. Ghannam and Y. Abdulraheem. “Electrophysical interpretation of the degradation of the fill factor in solar cells based on thermionic emission theory”. In: *Materials Science in Semiconductor Processing* 79 (2018), pp. 83–89. doi: 10.1016/j.mssp.2018.01.011. url: https://doi.org/10.1016/j.mssp.2018.01.011.

[18] Martin A. Green. *I-V Curve of a Solar Cell*. https://www.pveducation.org/pvcdrom/solar-cell-operation/iv-curve. Accessed: August 5, 2025. 2023. url: https://www.pveducation.org/pvcdrom/solar-cell-operation/iv-curve.

[19] David J. Griffiths. *Introduction to Electrodynamics*. 4th. Pearson, 2013. isbn: 978-0321856562.

[20] Zhanglin Guo et al. “The high open-circuit voltage of perovskite solar cells: a review”. In: *Energy & Environmental Science* 15.8 (2022), pp. 2902–2923. doi: 10.1039/D2EE00663D. url: https://doi.org/10.1039/D2EE00663D.

[21] Z. He et al. “Overcoming the wetting issues of PTAA in inverted perovskite solar cells by cinnamyl alcohol modification”. In: *Solar Energy Materials Solar Cells* xxx (2025), pp. xxx–xxx. doi: 10.1016/j.solmat.2025.xxx.

[22] Mei-Kei Ieong et al. “Comparison of Raised and Schottky Source/Drain MOSFETs Using a Novel Tunneling Contact Model”. In: *1998 International Electron Devices Meeting. Technical Digest (Cat. No.98CH36217)*. IEEE, 1998, pp. 733–736. doi: 10.1109/IEDM.1998.746461.

[23] Ajay K. Jena, Arvind Kulkarni, and Tsutomu Miyasaka. “Halide Perovskite Photovoltaics: Background, Status, and Future Prospects”. In: *Chemical Reviews* 119.5 (2019), pp. 3036–3103. doi: 10.1021/acs.chemrev.8b00539.

[24] W. M. M. Kessels et al. “Remote plasma deposition of hydrogenated amorphous silicon: a kinetic model of dangling bond coverage”. In: *Journal of Vacuum Science Technology A* 18.2 (2000), pp. 613–626. doi: 10.1116/1.582228.

[25] Takashi Koida, Michio Kondo, and Hiroaki Okamoto. “Structural and electrical properties of hydrogen-doped In_2O_3 films fabricated by solid-phase crystallization”. In: *Japanese Journal of Applied Physics* 47.11R (2008), pp. 8124–8127. doi: 10.1143/JJAP.47.8124.

[26] Bhushan P. Kore, Mahboubeh Jamshidi, and James M. Gardner. “The impact of moisture on the stability and degradation of perovskites in solar cells”. In: *Materials Advances* 5 (2024), pp. 2200–2217. doi: 10.1039/D3MA00828B. url: https://doi.org/10.1039/D3MA00828B.

[27] Dimitar I. Kutsarov et al. “Progress in Flexible Perovskite Solar Cells: Paving the Way for Scalable Manufacturing”. In: *Advanced Materials Technologies* 8.20 (2023), p. 2300410. doi: 10.1002/admt.202300410. url: https://doi.org/10.1002/admt.202300410.

[28] Xiaoyue Li et al. “Review and perspective of materials for flexible solar cells”. In: *Materials Reports: Energy* 1.1 (2021). Open Access, p. 100001. doi: 10.1016/j.matre.2020.09.001. url: https://doi.org/10.1016/j.matre.2020.09.001.

[29] Gianluca Limodio et al. “Modulated surface texturing of temporary Al foils substrates for high-efficiency thin-film, flexible solar cells”. In: *Solar Energy Materials and Solar Cells* 180 (2018), pp. 82–90. doi: 10.1016/j.solmat.2017.06.020.

[30] Yong Liu, Jin Zhang, and Xinyu Chen. “Efficient Interface Passivation of NiOx/Perovskite for Improved Carrier Dynamics”. In: *Small* 21.10 (2025), e202405953. doi: 10.1002/smll.202405953.

[31] David C. Look. “Recent advances in ZnO materials and devices”. In: *Materials Science and Engineering: B* 80.1-3 (2001), pp. 383–387. doi: 10.1016/S0921-5107(00)00604-8.

[32] P. Markoš. “Absence of diffusion in certain random lattices: Numerical evidence”. In: *arXiv:cond-mat/0807.2531* (2008). Accessed July 2025. url: https://www.researchgate.net/publication/1742098.

[33] J.M. Martínez-Duart, R.J. Martín-Palma, and F. Agulló-Rueda. “Survey of Solid State Physics”. In: *Nanotechnology for Microelectronics and Optoelectronics*. European Materials Research Society Series. Elsevier, 2006, pp. 21–53. doi: 10.1016/B978-008044553-3/50005-9. url: https://doi.org/10.1016/B978-008044553-3/50005-9.

[34] Inès Massiot. “Design and fabrication of nanostructures for light-trapping in ultra-thin solar cells”. PhD thesis. Ecole Centrale de Lyon, Oct. 2013. doi: 10.13140/RG.2.1.2731.0167. url: https://www.researchgate.net/publication/281383935.

[35] National Renewable Energy Laboratory (NREL). *Reference Air Mass 1.5 Spectra (ASTM G-173-03)*. https://www.nrel.gov/grid/solar-resource/spectra.html. Accessed: 2025-08-21. 2003.

[36] Donald A. Neamen. *Semiconductor Physics and Devices: Basic Principles*. 4th. McGraw-Hill Education, 2012. isbn: 978-0073529585.

[37] B. Niesen et al. “Self-patterned nanoparticle layers for vertical interconnects: application in tandem solar cells”. In: *Nano Letters* 14.3 (2014). Demonstrates nanoparticle-based intermediate reflectors maintaining vertical conductivity and optical reflection in micromorph tandems., pp. 1908–1913. doi: 10.1021/nl404760k.

[38] P. Otero et al. “Simulation of the temperature dependence of a-Si:H solar cell current–voltage characteristics”. In: *Proceedings of the 8th Spanish Conference on Electron Devices, CDE’2011*. Palma de Mallorca, Spain: IEEE, 2011, pp. 1–4. doi: 10.1109/SCED.2011.5744227.

[39] Helen Park. “Efficient and Stable Perovskite Solar Cells Based on Inorganic Hole Transport Materials”. In: *Nanomaterials* 12 (Dec. 2021), p. 112. doi: 10.3390/nano12010112.

[40] J. W. Peck, D. W. Hess, and D. B. Graves. “High-deposition-rate nanocrystalline and amorphous silicon thin-film production via surface-wave plasma source”. In: *Proceedings of the 44th IEEE Photovoltaic Specialists Conference (PVSC)*. 2017, pp. 1747–1752. doi: 10.1109/PVSC.2017.8366211.

[41] Wei Peng, Khaled J. Abbas, and Michael Saliba. “Reducing Nonradiative Recombination in Perovskite Solar Cells at the p-Type Contact”. In: *Science* 378.6619 (2022), pp. 331–336. doi: 10.1126/science.ade3126.

[42] Bart E. Pieters et al. “Electrical characterization and modeling of microcrystalline silicon bottom junction solar cells in tandem devices”. In: *Proceedings of the 23rd European Photovoltaic Solar Energy Conference and Exhibition (EU PVSEC)*. Valencia, Spain, 2008, pp. 2147–2150.

[43] Jef Poortmans and Vladimiro A. Smirnov. “Tandem Amorphous/Microcrystalline Silicon Solar Cells: The Micromorph Concept”. In: *Thin Film Solar Cells: Fabrication, Characterization and Applications*. Wiley, 2006. Chap. 4.3.3, pp. 159–161.

[44] P. Procel et al. “Opto-electrical modelling and roadmap for 2T monolithic Perovskite/CIGS tandem solar cells”. en. In: *Solar Energy Materials and Solar Cells* 274 (Aug. 2024), p. 112975. issn: 09270248. doi: 10.1016/j.solmat.2024.112975. url: https://linkinghub.elsevier.com/retrieve/pii/S0927024824002873 (visited on 02/17/2025).

[45] D. Qiu et al. “A Review: Application of Doped Hydrogenated Nanocrystalline Silicon Oxide in High Efficiency Solar Cell Devices”. In: *Advanced Science* 11 (2024), p. 2403728. doi: 10.1002/advs.202403728. url: https://doi.org/10.1002/advs.202403728.

[46] Omkar V. Rambadey et al. “Exploring the Interrelation between Urbach Energy and Dielectric Constant in Hf-Substituted $BaTiO_3$”. In: *ACS Omega* 6.47 (2021), pp. 32231–32238. doi: 10.1021/acsomega.1c05057. url: https://doi.org/10.1021/acsomega.1c05057.

[47] ResearchGate. *Recombination Processes in Semiconductors*. https://www.researchgate.net/figure/Recombination-Processes-in-Semiconductors-A-radiative-recombination-B-non-radiative_fig1_367078141. Accessed: 2024-05-08. 2023.

[48] S. Saha et al. “Effect of field dependent mobility on the analytical modeling of emitter saturation current of a silicon solar cell”. In: *2011 IEEE International Conference on Computer Applications and Industrial Electronics (ICCAIE)*. 2011, pp. 7–11. doi: 10.1109/ICCAIE.2011.6162094. url: https://doi.org/10.1109/ICCAIE.2011.6162094.

[49] Luigi Saitta and et al. “Performance improvement of p-i-n µc-Si:H solar cells with IOH/ZnO TCO bilayer front contacts”. In: *Solar Energy Materials and Solar Cells* 257 (2025), p. 112219. doi: 10.1016/j.solmat.2024.112219.

[50] Jordi Sancho-Parramon et al. “Optical spectroscopy study of nc-Si-based p–i–n solar cells”. In: *Solar Energy Materials and Solar Cells* 93.10 (2009), pp. 1768–1772. doi: 10.1016/j.solmat.2009.06.008.

[51] Jordi Sancho-Parramon et al. “Optical spectroscopy study of nc-Si-based p–i–n solar cells”. en. In: *Solar Energy Materials and Solar Cells* 93.10 (Oct. 2009), pp. 1768–1772. issn: 09270248. doi: 10.1016/j.solmat.2009.06.008. url: https://linkinghub.elsevier.com/retrieve/pii/S0927024809002219 (visited on 03/07/2025).

[52] M. C. M. van de Sanden et al. “Plasma chemistry aspects of a-Si:H deposition using an expanding thermal plasma”. In: *Journal of Applied Physics* 84.5 (1998), pp. 2426–2435. doi: 10.1063/1.368977.

[53] Sandia National Laboratories. *Single-Diode Equivalent Circuit of a Solar Cell*. Accessed: 22-Aug-2025. 2022. url: https://www.sandia.gov/app/uploads/sites/243/2022/11/Single-Diode-EC2.png.

[54] R. Santbergen. *GENPRO4: Optical Model for Multilayer Solar Cells*. Accessed from internal documentation. 2017.

[55] Md. Nazmul Islam Sarkar and Himangshu Ranjan Ghosh. “Performance Enhancement of an a-Si:H/µc-Si:H Heterojunction p-i-n Solar Cell by Tuning the Device Parameters”. In: *Dhaka University Journal of Science* 69.2 (2021), pp. 88–95. doi: 10.3329/dujs.v69i2.56488.

[56] A. Shah et al. “Microcrystalline Silicon and ‘Micromorph’ Tandem Solar Cells”. In: *Thin Solid Films* 403-404 (2002), pp. 179–187. doi: 10.1016/S0040-6090(01)01658-3.

[57] Arvind Shah. *Chapter IC-1 - Thin-Film Silicon Solar Cells1*. Accessed: 2025-02-26. Unknown Publisher, 2012.

[58] Arvind Shah. “Thin-Film Silicon Solar Cells”. en. In: *Solar Cells*. Elsevier, 2013, pp. 159–223. isbn: 978-0-12-386964-7. doi: 10.1016/B978-0-12-386964-7.00007-X. url: https://linkinghub.elsevier.com/retrieve/pii/B978012386964700007X (visited on 02/17/2025).

[59] Arvind V Shah et al. “Basic efficiency limits, recent experimental results and novel light-trapping schemes in a-Si:H, µc-Si:H and ‘micromorph tandem’ solar cells”. en. In: *Journal of Non-Crystalline Solids* 338-340 (June 2004), pp. 639–645. issn: 00223093. doi: 10.1016/j.jnoncrysol.2004.03.074. url: https://linkinghub.elsevier.com/retrieve/pii/S0022309304002297 (visited on 02/17/2025).

[60] Ashish Sharma et al. “Analytical Model of Thin-Film Silicon Solar Cell”. In: *Proceedings of the ASME 2015 International Mechanical Engineering Congress and Exposition (IMECE2015)*. Houston, Texas, USA, Nov. 2015. doi: 10.1115/IMECE2015-50793. url: https://www.researchgate.net/publication/294342954_Analytical_Model_of_Thin-Film_Silicon_Solar_Cell.

[61] X. Shen et al. “Improvement in efficiency of micromorph tandem silicon solar cells by designing proper interfaces”. In: *Optics Letters* 40.22 (2015). Shows that combining front antireflection layers with SiO_x intermediate reflectors improves current matching and optical efficiency., pp. 5180–5183. doi: 10.1364/OL.40.005180.

[62] Tatsuo Shimizu. “Staebler-Wronski Effect in Hydrogenated Amorphous Silicon and Related Alloy Films”. In: *Japanese Journal of Applied Physics* 43.6A (2004), pp. 3257–3268. doi: 10.1143/JJAP.43.3257.

[63] E. M. Spaans, O. Isabella, and M. Zeman. “Optimisation of a-Si:H/μc-Si:H Tandem Solar Cell on Flexible Al Substrates”. In: *Energy Procedia* 77 (2015), pp. 599–606. doi: 10.1016/j.egypro.2015.07.086.

[64] Robert A. Street. *Hydrogenated Amorphous Silicon*. Cambridge University Press, 1991.

[65] M. Stückelberger et al. “Impact of the electric field on the fill factor of amorphous silicon solar cells”. In: *Journal of Applied Physics* 107.12 (2010), p. 124516. doi: 10.1063/1.3437644.

[66] Synopsys Inc. *Sentaurus Device User Guide, Version K-2015.06*. Accessed as internal documentation. Synopsys. 2015.

[67] Michael Vetter et al. “Development of High Performance Industrial TCO Glass for Very Large Area a-Si:H PV Modules”. In: *Proceedings of the 26th European Photovoltaic Solar Energy Conference and Exhibition (EUPVSEC)*. 2011, pp. 2676–2679. doi: 10.4229/26thEUPVSEC2011-3AV.2.28.

[68] Jianqiang Wang et al. “Investigation of an a-Si/c-Si interface on a c-Si(P) substrate by simulation”. In: *Journal of Semiconductors* 33.3 (2012), p. 033001. doi: 10.1088/1674-4926/33/3/033001.

[69] Yue Wu, Xiao Wang, and Jianhua Zhao. “Interface Engineering with PIDTTDQ for Efficient Inverted Perovskite Solar Cells”. In: *Materials Today Energy* 30 (2023), p. 101329. doi: 10.1016/j.mtener.2023.101329.

[70] Peter Würfel. *Physics of Solar Cells: From Basic Principles to Advanced Concepts*. Wiley-VCH, 2009.

[71] Haitao Xu et al. “Hole transport layers for organic solar cells: recent progress and prospects”. In: *Journal of Materials Chemistry A* 8.6 (2020), pp. 11478–11506. doi: 10.1039/d0ta03511d. url: https://doi.org/10.1039/D0TA03511D.

[72] D. Yeo et al. “Self-Assembled Monolayer-Based Hole-Transporting Materials for Perovskite Solar Cells”. In: *Nanomaterials* 14.2 (Jan. 2024), p. 175. doi: 10.3390/nano14020175.

[73] Min Ju Yun et al. “Honeycomb-Structured 3D Concave Photovoltaic Modules Supported by 3D Mechanical Metamaterials for Enhanced Light Recapture”. In: *Advanced Materials Technologies* 8.2 (2022), p. 2201360. doi: 10.1002/admt.202201360. url: https://doi.org/10.1002/admt.202201360.

[74] D. Zhang et al. “Progress in the Synthesis and Application of Transparent Conducting Film of AZO (ZnO:Al)”. In: *Materials* 16.16 (2023), p. 5537. issn: 1996-1944. doi: 10.3390/ma16165537.

[75] W. Zhang et al. “Synergistic effects of the physical modification and interlayer engineering for high-performance perovskite solar cells with PTAA”. In: *Solar Energy Materials Solar Cells* (2024). doi: 10.1016/j.solmat.2024.xxx.

[76] X.-D. Zhang et al. “Micromorph tandem solar cells: optimization of the microcrystalline silicon bottom cell in a single chamber system”. In: *Chinese Physics B* 20.10 (2011). Optimization of nc-Si:H bottom cell and light management strategies for current matching in micromorph tandems., p. 108801. doi: 10.1088/1674-1056/20/10/108801.

A

Baseline parameters a-Si

Table A.1: Material and defect parameters for P, I, and N layers of a-Si:H solar cell

	P	**I**	**N**
Extended states			
Bandgap [eV]	2.84	1.653	2.42
N_V [cm^{-3}]	2×10^{20}	2×10^{20}	2×10^{20}
N_C [cm^{-3}]	2×10^{20}	2×10^{20}	2×10^{20}
χ [eV]	3.9	3.9	3.9
ε [-]	11.9	11.9	11.9
μ_e [cm^2/Vs]	10	10	10
μ_h [cm^2/Vs]	2	2	2
Valence band tails			
Urbach energy [eV]	0.12	0.0046	0.094
N_{Emob} [cm^{-3}/eV]	2×10^{21}	1.88×10^{21}	2×10^{21}
e/h capture cross section [cm^2]	$7 \times 10^{-16}/7 \times 10^{-16}$	$7 \times 10^{-16}/7 \times 10^{-16}$	$7 \times 10^{-16}/7 \times 10^{-16}$
Conduction band tails			
Urbach energy [eV]	0.08	0.0046	0.068
N_{Emob} [cm^{-3}/eV]	2×10^{21}	1.83×10^{21}	2×10^{21}
e/h capture cross section [cm^2]	$7 \times 10^{-16}/7 \times 10^{-16}$	$7 \times 10^{-16}/7 \times 10^{-16}$	$7 \times 10^{-16}/7 \times 10^{-16}$
Dangling bond			
Peak defect density [cm^3 eV^1]	1.31×10^{20}	1.38×10^{16}	1.31×10^{20}
Peak Width [eV]	0.21	0.13	0.21
Donor peak position [eV]	1.1	0.89	0.5
Acceptor peak position [eV]	1.2	1.09	0.6
Donor e/h capture cross section [cm^2]	$3 \times 10^{-14}/3 \times 10^{-15}$	$3 \times 10^{-14}/3 \times 10^{-15}$	$3 \times 10^{-14}/3 \times 10^{-15}$
Acceptor e/h capture cross section [cm^2]	$3 \times 10^{-15}/3 \times 10^{-14}$	$3 \times 10^{-15}/3 \times 10^{-14}$	$3 \times 10^{-15}/3 \times 10^{-14}$

B

NLM parameters

Table B.1: Summary of Nonlocal Tunneling (NLM) Models Used Across All Simulated Solar Cell Structures

Interface (RegionInterface)	Length [$\times 10^{-7}$ cm]	Permeation [$\times 10^{-7}$ cm]	Tunneling Type(s)
a-Si:H Single-Junction (SJ)			
nc-SiO_x(p) / AZO	4.0	1.0	B2BT, TAT
nc-SiO_x(p) / a-Si:H(i)	13.1	1.0	B2BT, TAT
nc-Si:H Single-Junction (SJ)			
nc-SiO_x(p) / nc-Si:H(i)	15.0	1.0	B2BT, TAT
ZnO:Al / nc-SiO_x(p)	7.0	1.0	B2BT, TAT
a-Si:H/nc-Si:H Tandem Cell			
nc-SiO_x(p) / a-Si:H(i)	30.0	5.0	B2BT, TAT
nc-Si:H(p) / nc-Si:H(i)	5.0	5.0	B2BT
ZnO:Al / nc-SiO_x(p)	7.0	10.0	B2BT, TAT
nc-Si:H(n) / nc-Si:H(p) (TRJ)	20.0	5.0	B2BT
Perovskite (PVK) Single-Junction (SJ)			
Perovskite / C_{60} (ETL)	1.0	25.0	B2BT
HTL / Perovskite	21.0	2.0	B2BT
a-Si:H/Perovskite Tandem Cell			
ZnO:Al / nc-SiO_x(p)	4.0	1.0	B2BT
nc-SiO_x(p) / a-Si:H(i)	30.0	5.0	B2BT
nc-Si:H(n) / ITO (TRJ)	10.0	10.0	B2BT
C_{60}/BCP / Perovskite	30.0	2.0	B2BT
ITO / TCO (TRJ)	10.0	10.0	B2BT
Perovskite/Perovskite (PVK/PVK) Tandem Cell (Organic and Inorganic)			
Top Perovskite / C_{60}	1.0	25.0	B2BT
HTL / Top Perovskite	26.0	5.0	B2BT
TRJ (ITO/HTL)	20.0	20.0	B2BT
C_{60}/BCP / Bottom Perovskite	30.0	2.0	B2BT
PVK/PVK Tandem with nc-SiO_x(p) HTLs			
Top Perovskite / C_{60}	1.0	25.0	B2BT
TRJ (ITO/HTL)	20.0	21.0	B2BT
nc-SiO_x(p) / AZO	4.0	1.0	B2BT, TAT
nc-SiO_x(p) / Perovskite	13.1	13.1	B2BT, TAT
C_{60}/BCP / Perovskite	30.0	2.0	B2BT

C

Device Structures

This appendix provides a comprehensive overview of the device architectures used in the optical and electrical simulations presented throughout this thesis. It includes all single-junction (SJ), tandem, and hybrid configurations implemented in Sentaurus `sdevice`, together with the corresponding layer stacks and material parameters. The models were developed to enable a consistent comparison between thin-film silicon, perovskite, and hybrid a-Si:H/PVK and PVK/PVK tandem solar cells. Each structure is defined according to its calibrated optical generation profiles from GENPRO4 and electrical transport parameters extracted from literature or prior validated simulations. The sections that follow describe, in order, (i) the a-Si:H and nc-Si:H single-junction and tandem models, (ii) the perovskite single-junction reference structures, (iii) the hybrid a-Si:H/PVK tandem, and (iv) the all-perovskite tandem configurations.

C.1. a-Si:H and nc-Si:H single-junction and a-Si:H/nc-Si:H tandem model

The single-junction amorphous (a-Si:H) and nanocrystalline (nc-Si:H) solar cell models were developed and calibrated as reference structures for the tandem configuration. Both devices employ p–i–n architectures with transparent conductive oxide (TCO) front contacts, nc-SiO_x-based window and contact layers, and Ag or ZnO back reflectors. Material, defect, and doping parameters were extracted and adapted from literature and previous calibrated models, ensuring consistency between optical generation profiles (from GENPRO4) and electrical simulations (in Sentaurus `sdevice`). Each layer includes extended states, exponential band-tail distributions, and Gaussian midgap defect states representing dangling bonds.

Table C.1 summarizes the layer-specific parameters used for the single-junction a-Si:H p–i–n device. The stack (AZO / nc-SiO_x(p) / nc-SiO_x window / a-Si:H(i) / nc-SiO_x(n) / Ag) reproduces experimental performance benchmarks through calibrated Urbach energies, trap densities, and doping levels.

Table C.2 lists the equivalent parameters for the nc-Si:H single-junction (SJ) device. The intrinsic absorber is divided into three sublayers (nc-Si1–3) with gradually increasing crystallinity, reflected by decreasing bandgap and Urbach energy values with depth. The model captures carrier transport through a mixed-phase (amorphous + crystalline) medium using effective medium parameters and defect distributions tuned to reproduce measured J–V characteristics.

Finally, Table 4.8 compiles the calibrated parameters for the p, i, and n layers in the complete a-Si:H/nc-Si:H tandem solar cell. The top (a-Si:H) and bottom (nc-Si:H) subcells share consistent interface definitions, with trap and tail-state parameters derived directly from their single-junction calibrations. This ensures a physically continuous energy band alignment across the tunnel recombination junction (TRJ) and minimizes artificial discontinuities in the optical and electrical simulations.

Table C.1: Material, defect, and doping parameters for the single-junction a-Si:H p–i–n solar cell. The optical and electrical layer stack corresponds to the Sentaurus simulation model (AZO / nc-SiO_x(p) / nc-SiO_x window / a-Si:H(i) / nc-SiO_x(n) / Ag). Extended-state and defect parameters follow the calibrated tandem baseline.

	AZO (TCO)	**p-layer**	**Window layer**	**Intrinsic absorber**	**n-layer**	**Ag (Back)**
Extended states						
Bandgap E_g [eV]	3.3	2.84	2.84	1.63	2.42	–
Electron affinity χ [eV]	4.5	3.37	3.37	4.00	3.55	–
ε_r [-]	9.0	11.9	11.9	11.9	11.9	–
N_C [cm^{-3}]	1×10^{20}	1×10^{20}	1×10^{20}	1×10^{20}	1×10^{20}	–
N_V [cm^{-3}]	1×10^{20}	1×10^{20}	1×10^{20}	1×10^{20}	1×10^{20}	–
μ_n [cm^2/Vs]	20	10	10	10	10	–
μ_p [cm^2/Vs]	10	2	2	2	2	–
Doping and composition						
Layer material	ZnO:Al	nc-SiO_x(p)	nc-SiO_x	a-Si:H(i)	nc-SiO_x(n)	Ag
Thickness [nm]	10	3	10	300	20	100
Type	n^+	p^+	p-type	intrinsic	n^+	metal
Doping conc. [cm^{-3}]	3.8×10^{20}	-1.0×10^{20}	-6.0×10^{19}	intrinsic	2.0×10^{19}	–
Valence band tails						
Urbach energy E_U [eV]	–	0.05	0.05	0.03	0.094	–
N_{Emob} [cm^{-3}/eV]	–	1×10^{21}	1×10^{21}	2×10^{20}	1×10^{21}	–
σ_e [cm^2]	–	1×10^{-16}	1×10^{-16}	1×10^{-16}	1×10^{-16}	–
σ_h [cm^2]	–	1×10^{-16}	1×10^{-16}	1×10^{-16}	1×10^{-16}	–
Conduction band tails						
Urbach energy E_U [eV]	–	0.08	0.08	0.022	0.068	–
N_{Emob} [cm^{-3}/eV]	–	1×10^{21}	1×10^{21}	2×10^{20}	1×10^{21}	–
σ_e [cm^2]	–	1×10^{-16}	1×10^{-16}	1×10^{-16}	1×10^{-16}	–
σ_h [cm^2]	–	1×10^{-16}	1×10^{-16}	1×10^{-16}	1×10^{-16}	–
Dangling bonds						
N_{DB} [cm^{-3}]	–	1.3×10^{18}	1.3×10^{18}	7.8×10^{15}	1.3×10^{18}	–
Peak width [eV]	–	0.21	0.21	0.144	0.21	–
Donor peak position [eV]	–	1.1	1.1	0.92	0.9	–
Acceptor peak position [eV]	–	1.4	1.4	1.02	1.2	–
Donor σ_e [cm^2]	–	3×10^{-14}	3×10^{-14}	3×10^{-14}	3×10^{-14}	–
Donor σ_h [cm^2]	–	3×10^{-15}	3×10^{-15}	3×10^{-15}	3×10^{-15}	–
Acceptor σ_e [cm^2]	–	3×10^{-15}	3×10^{-15}	3×10^{-15}	3×10^{-15}	–
Acceptor σ_h [cm^2]	–	3×10^{-14}	3×10^{-14}	3×10^{-14}	3×10^{-14}	–

Table C.2: Material, defect, and doping parameters for the single-junction nc-Si:H p–i–n solar cell. The structure follows the Sentaurus simulation stack IOH / ZnO:Al / nc-SiO_x(p) / nc-SiO_x window / nc-Si:H(i_1–i_3) / nc-SiO_x(n) / ZnO:Al. Layer thicknesses and dopings correspond to the calibrated single-junction configuration.

	IOH (TCO)	ZnO:Al (Front)	p-layer	Window	nc-Si1	nc-Si2	nc-Si3	n-layer
Extended states								
Bandgap E_g [eV]	3.3	3.3	2.84	2.84	1.25	1.20	1.15	2.42
Electron affinity χ [eV]	4.5	4.4	3.33	3.33	4.05	4.05	4.05	3.39
ε_r [-]	9.0	9.0	11.9	11.9	11.9	11.9	11.9	11.9
N_C [cm^{-3}]	1×10^{20}	1×10^{20}	1×10^{20}	1×10^{20}	8×10^{19}	8×10^{19}	8×10^{19}	1×10^{20}
N_V [cm^{-3}]	1×10^{20}	1×10^{20}	1×10^{20}	1×10^{20}	6×10^{19}	6×10^{19}	6×10^{19}	1×10^{20}
μ_n [cm^2/Vs]	20	20	10	10	20	25	30	10
μ_p [cm^2/Vs]	10	10	2	2	3	5	6	2
Doping and composition								
Material	IOH	ZnO:Al	nc-SiO_x(p)	nc-SiO_x	nc-Si:H(1)	nc-Si:H(2)	nc-Si:H(3)	nc-SiO_x(n)
Thickness [nm]	130	5	7	3	800	1000	1400	20
Type	n^+	n^+	p^+	p-type	intrinsic	intrinsic	intrinsic	n^+
Doping [cm^{-3}]	3.8×10^{20}	1.0×10^{15}	-1.0×10^{20}	-6.0×10^{19}	intrinsic	intrinsic	intrinsic	2.0×10^{19}
Valence band tails								
Urbach energy E_U [eV]	–	–	0.05	0.05	0.031	0.034	0.037	0.094
N_{Emob} [cm^{-3}/eV]	–	–	1×10^{21}	1×10^{21}	1×10^{19}	5×10^{19}	1×10^{20}	1×10^{21}
σ_e [cm^2]	–	–	1×10^{-16}	1×10^{-16}	1×10^{-16}	1×10^{-16}	1×10^{-16}	7×10^{-16}
σ_h [cm^2]	–	–	1×10^{-16}	1×10^{-16}	1×10^{-17}	1×10^{-17}	1×10^{-17}	7×10^{-16}
Conduction band tails								
Urbach energy E_U [eV]	–	–	0.08	0.08	0.031	0.034	0.037	0.068
N_{Emob} [cm^{-3}/eV]	–	–	1×10^{21}	1×10^{21}	1×10^{19}	5×10^{19}	1×10^{20}	1×10^{21}
σ_e [cm^2]	–	–	1×10^{-16}	1×10^{-16}	1×10^{-17}	1×10^{-17}	1×10^{-17}	7×10^{-16}
σ_h [cm^2]	–	–	1×10^{-16}	1×10^{-16}	1×10^{-16}	1×10^{-16}	1×10^{-16}	7×10^{-16}
Dangling bonds								
N_{DB} [cm^{-3}]	–	–	1.3×10^{18}	1.3×10^{18}	1.5×10^{14}	1.5×10^{14}	1.5×10^{14}	1.3×10^{18}
Peak width [eV]	–	–	0.21	0.21	0.144	0.144	0.144	0.21
Donor peak position [eV]	–	–	0.9	0.9	0.7	0.7	0.7	1.1
Acceptor peak position [eV]	–	–	1.2	1.2	0.85	0.85	0.85	1.2
Donor σ_e [cm^2]	–	–	3×10^{-14}	3×10^{-14}	3×10^{-15}	3×10^{-15}	3×10^{-15}	3×10^{-14}
Donor σ_h [cm^2]	–	–	3×10^{-15}	3×10^{-15}	3×10^{-16}	3×10^{-16}	3×10^{-16}	3×10^{-15}
Acceptor σ_e [cm^2]	–	–	3×10^{-15}	3×10^{-15}	3×10^{-16}	3×10^{-16}	3×10^{-16}	3×10^{-15}
Acceptor σ_h [cm^2]	–	–	3×10^{-14}	3×10^{-14}	3×10^{-15}	3×10^{-15}	3×10^{-15}	3×10^{-14}

Table C.3: Material, defect, and doping parameters for the P, I, and N layers of the tandem a-Si:H / nc-Si:H solar cell. The doping concentrations correspond to the calibrated tandem configuration. Where applicable, values differing from the single-junction (SJ) cells are annotated with superscripts.

	Top cell (a-Si:H)			Bottom cell (nc-Si:H)		
	P	I	N	P	I	N
Extended states						
Bandgap [eV]	2.84	1.65[(a)]	2.42	2.84	1.25[(nc)]	2.42
N_V [cm^{-3}]	1×10^{20}	1×10^{20}	1×10^{20}	1×10^{20}	6×10^{19}	1×10^{20}
N_C [cm^{-3}]	1×10^{20}	1×10^{20}	1×10^{20}	1×10^{20}	8×10^{19}	1×10^{20}
χ [eV]	3.37	4.00	3.55	3.33[(nc)]	4.05	3.39[(nc)]
ε_r [-]	11.9	11.9	11.9	11.9	11.9	11.9
μ_n [cm^2/Vs]	10	10	10	10	30	10
μ_p [cm^2/Vs]	2	2	2	2	6	2
Doping and composition						
Layer composition	nc-SiO_x(p) / a-SiO_x (20/3 nm)[‡]	a-Si:H (300 nm)	nc-Si:H (50 nm)	nc-Si:H (20 nm)[†]	nc-Si:H (3000 nm)	nc-Si:H (20 nm)
N_A or N_D [cm^{-3}]	1.0×10^{20}/1.0×10^{18}	intrinsic	8.0×10^{19}	2.0×10^{20}/(6.5×10^{19})	intrinsic	4.0×10^{19}
Valence band tails						
Urbach energy [eV]	0.05	0.03	0.094	0.05	0.036[(nc)]	0.094
N_{Emob} [cm^{-3}/eV]	1×10^{21}	2×10^{20}	1×10^{21}	1×10^{20}	4.8×10^{19}[(nc)]	1×10^{21}
Electron σ_e [cm^2]	1×10^{-16}	1×10^{-16}	1×10^{-16}	1×10^{-16}	1×10^{-16}	1×10^{-16}
Hole σ_h [cm^2]	1×10^{-16}	1×10^{-16}	1×10^{-16}	1×10^{-16}	1×10^{-17}	1×10^{-16}
Conduction band tails						
Urbach energy [eV]	0.08	0.022	0.068	0.08	0.036[(nc)]	0.068
N_{Emob} [cm^{-3}/eV]	1×10^{21}	2×10^{20}	1×10^{21}	1×10^{20}	9.6×10^{19}[(nc)]	1×10^{21}
Electron σ_e [cm^2]	1×10^{-16}	1×10^{-16}	1×10^{-16}	1×10^{-16}	1×10^{-17}	1×10^{-16}
Hole σ_h [cm^2]	1×10^{-16}	1×10^{-16}	1×10^{-16}	1×10^{-16}	1×10^{-16}	1×10^{-16}
Dangling bonds						
Defect Concentration [$cm^{-3}eV^{-1}$]	1.3×10^{18}	1.74×10^{16}[(a)]	1.3×10^{18}	1.3×10^{18}	3×10^{15}[(nc)]	1.3×10^{18}
Peak Width [eV]	0.21	0.144	0.21	0.21	0.144	0.21
Donor peak position [eV]	1.1	0.92	1.1	1.1[(nc)]	0.70	1.1
Acceptor peak position [eV]	1.2	1.02	1.2	1.4[(nc)]	0.85	1.2
Donor σ_e [cm^2]	3×10^{-14}	3×10^{-14}	1×10^{-14}[(a)]	1×10^{-14}[(nc)]	3×10^{-15}	1×10^{-14}
Donor σ_h [cm^2]	3×10^{-15}	3×10^{-15}	1×10^{-15}[(a)]	1×10^{-15}[(nc)]	3×10^{-16}	1×10^{-15}
Acceptor σ_e [cm^2]	3×10^{-15}	3×10^{-15}	1×10^{-15}[(a)]	1×10^{-15}[(nc)]	3×10^{-16}	1×10^{-15}
Acceptor σ_h [cm^2]	3×10^{-14}	3×10^{-14}	1×10^{-14}[(a)]	1×10^{-14}[(nc)]	3×10^{-15}	1×10^{-14}

(a) a-Si:H SJ: intrinsic $E_g = 1.63$ eV; DB density 7.8×10^{15} cm^{-3}.
(nc) nc-Si:H SJ: intrinsic $E_g = 1.15$ eV; $E_U = 0.036$ eV with $N_{Emob} \sim 5 \times 10^{19}$ cm^{-3}/eV; DB density 1.5×10^{14} cm^{-3}.
(†) Bottom p-layer: first 4 nm doped at 2×10^{20} cm^{-3}, remaining 16 nm at 6.5×10^{19} cm^{-3}.
(‡) Top p-layer consists of 20 nm nc-SiO_x(p) and 3 nm a-SiO_x window layer.

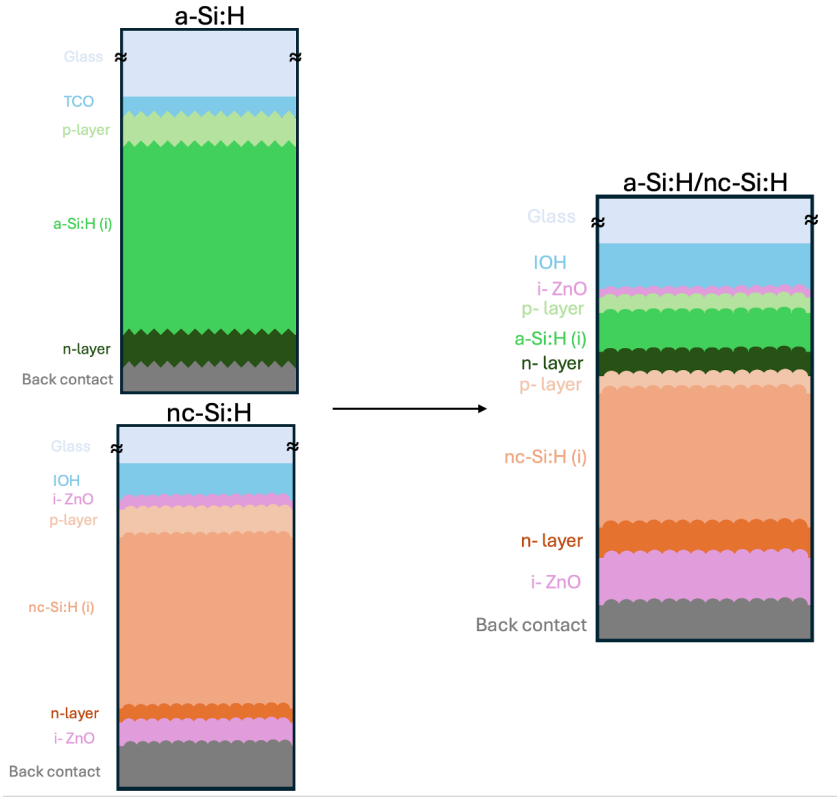

Figure C.1: Schematic representation of the simulated thin-film silicon device structures. The single-junction configurations (a-Si:H and nc-Si:H) serve as calibrated baselines for the tandem model, which combines both absorbers in a p–i–n/p–i–n stack.

C.2. Single-junction perovskite (PVK) models

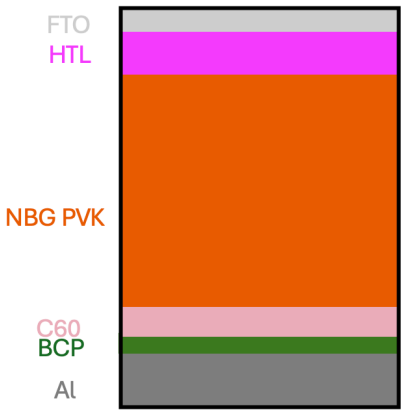

Figure C.2: Schematic structure of the simulated single-junction perovskite (SJ PVK) device. The architecture consists of an Al back contact, C_{60}/BCP electron transport stack, narrow-bandgap Sn–Pb perovskite absorber, and a hole transport layer (HTL) such as NiO_x, PEDOT:PSS, PTAA, 2PACz, or nc-SiO_x(p).

The single-junction perovskite model serves as a baseline for the hybrid and all-perovskite tandem configurations. It features a narrow-bandgap (1.23 eV) Sn–Pb perovskite absorber contacted by a C_{60}/BCP electron transport bilayer and various hole transport layers (HTLs). For the inorganic nc-SiO_x(p) HTL, the electronic and defect parameters—including exponential tail states and Gaussian dangling-bond distributions—were adopted directly from the a-Si:H single-junction (SJ) model (Table C.1). Table C.4

summarizes the key electronic and optical parameters used for all layers in the SJ PVK device stack. For all HTLs tunneling effective mass of 0.1 was taken.

Table C.4: Summary of key material parameters used for the perovskite single-junction and hybrid device stack, including electron transport layers (ETLs), hole transport layers (HTLs), and the perovskite absorber. Parameters for nc-SiO_x(p) were adopted from the a-Si:H single-junction solar cell (Table C.1).

Parameter	Perovskite (Sn–Pb)	C_{60} (ETL)	BCP (Buffer)	NiO_x (HTL)	PEDOT:PSS (HTL)	PTAA (HTL)	2PACz (SAM)	nc-SiO_x(p)
Thickness [nm]	900	25	8	20	20	20	∼2	13
Bandgap E_g [eV]	1.23	2.10	3.50	3.80	1.60	3.30	3.40	2.84
Electron affinity χ [eV]	3.90	3.90	2.50	1.46	3.50	1.80	1.70	3.37
Permittivity ε_r	20	10	10	10.7	3.0	3.0	10	11.9
Doping [cm^{-3}]	—	1.0×10^{19}	1.0×10^{2}	1.0×10^{19} (p-type)	1.0×10^{19} (p-type)	1.0×10^{19} (p-type)	1.0×10^{20} (eff.)	1.0×10^{20} (p-type)
N_C [cm^{-3}]	1.0×10^{18}	2.0×10^{18}	2.0×10^{18}	2.2×10^{18}	2.2×10^{18}	2.2×10^{18}	2.0×10^{18}	1.0×10^{20}
N_V [cm^{-3}]	1.0×10^{18}	2.0×10^{19}	1.8×10^{19}	1.8×10^{19}	1.8×10^{19}	1.8×10^{19}	2.0×10^{19}	1.0×10^{20}
μ_n [cm^2/Vs]	20	8.9×10^{-4}	1.0×10^{-3}	1.0×10^{-3}	1.8×10^{-3}	4.0×10^{-5}	1.0×10^{-3}	10
μ_p [cm^2/Vs]	10	8.9×10^{-4}	5.0×10^{-2}	1.0×10^{-3}	1.9×10^{-2}	4.0×10^{-5}	1.0×10^{-3}	2
Bulk lifetime τ [s]	1×10^{-6}[a]	—	—	1×10^{-7}	5×10^{-6}	1×10^{-5}	—	—
Surface recombination velocity (cm/s)	—	—	—	100	100	20	—	—

C.3. Flexible a-Si:H/nc-Si:H tandem and a-Si:H/PVK tandem

For the flexible a-Si:H/nc-Si:H tandem device, all electrical and optical parameters were kept identical to the rigid configuration simulated on Asahi glass (see Table 4.8). Only two modifications were applied to represent the flexible stack: (i) the dangling-bond (DB) density of the a-Si:H subcell was slightly increased from 7.8×10^{15} cm^{-3} to 1.08×10^{16} cm^{-3} to account for increased defect formation in the flexible substrate process, and (ii) the Ag back reflector was replaced by an Al contact layer.

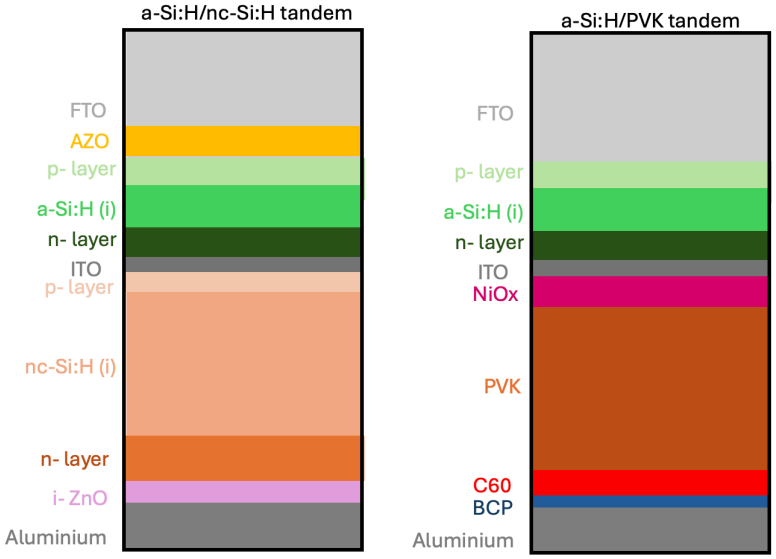

Figure C.3: Schematic front-stack configurations used in the flexible hybrid tandems. On the left the a-Si:H/ nc-Si:H tandem on a flexible substrate. On the right the a-Si:H/PVK tandem

For the a-Si:H/PVK hybrid tandem, the top subcell corresponds to the calibrated a-Si:H p–i–n junction from the a-Si:H/nc-Si:H tandem (Table 4.8), while the bottom subcell adopts the narrow-bandgap Sn–Pb perovskite configuration used in the single-junction PVK model (Table C.4). The two subcells are interconnected through a 5 nm ITO layer that serves as a tunnel recombination junction (TRJ), providing optical transparency and balanced carrier recombination. All other layer parameters—including bandgaps, doping levels, and defect distributions—were directly inherited from the respective single-junction reference devices.

Table C.5: Layer stack and material parameters for the hybrid a-Si:H / perovskite tandem solar cell. The top subcell (a-Si:H) corresponds to the top cell of the a-Si:H/nc-Si:H tandem, while the bottom subcell (perovskite) follows the NiO_x-based single-junction PVK configuration. The two subcells are connected by an ITO interlayer acting as a tunnel recombination junction (TRJ). Front and back contacts are FTO and Al, respectively.

Layer	Material	Thickness [nm]	Doping [cm^{-3}]
Front contact	FTO	5	3.8×10^{20} (n^+)
p-contact layer	nc-SiO_x(p)	20	1.0×10^{20} (p^+)
p-window	a-SiO_x	3	1.0×10^{18} (p-type)
Intrinsic absorber	a-Si:H(i)	280	intrinsic
n-contact layer	nc-SiO_x(n)	50	8.0×10^{19} (n^+)
Interlayer (TRJ)	ITO	5	5.0×10^{19} (n^+)
HTL (bottom)	NiO_x (PEDOT in code)	20	1.0×10^{19} (p^+)
Perovskite absorber	Sn–Pb perovskite	900	intrinsic
ETL	C_{60}	20	1.0×10^{19} (n^+)
Buffer	BCP	8	1.0×10^{20} (n^+)
Back contact	Al	–	–

C.4. PVK/PVK tandems

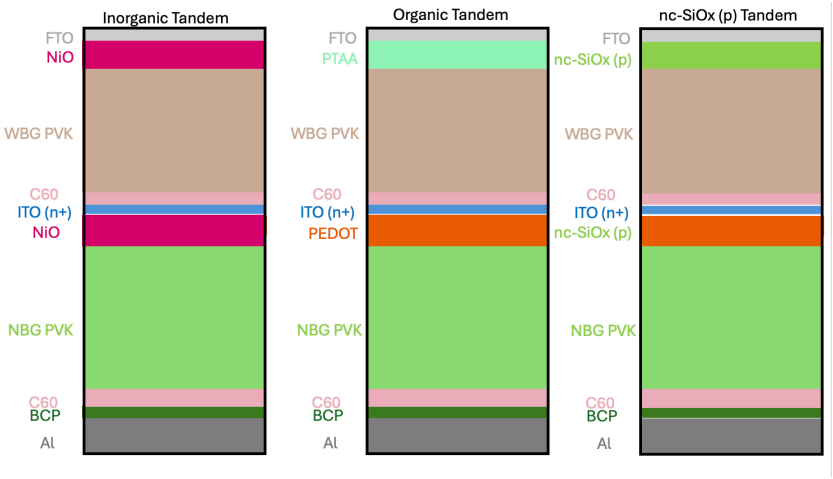

Figure C.4: Schematic front-stack configurations used in the flexible PVK/PVK tandems. From left to right: inorganic NiO-based, organic HTL (PTAA/PEDOT)-based, and nc-SiO_x(p)-based configurations. All devices are simulated on flexible substrates with Al back contacts.

The three tandem configurations shown in Figure C.4 each combine a wide-bandgap (WBG) and a narrow-bandgap (NBG) perovskite absorber. Both absorbers are 280 nm (WBG) and 900 nm (NBG) thick, respectively, and are connected by an ITO interlayer acting as a tunnel recombination junction (TRJ). The WBG perovskite parameters were adopted from [44]. These values were kept constant across all three tandems to isolate the influence of the HTLs. The values can be seen in Table C.6. For the HTLs, the inorganic configuration has a NiOx (20 nm) top HTL and a NiOx (20 nm) bottom HTL. The inorganic configuration has a PTAA (20 nm) top HTL and a PEDOT:PSS (20 nm) bottom HTL. Lastly, the nc-SiOx configuration has a nc-SiOx (p) (13 nm) top HTL and a nc-SiOx (20 nm) bottom HTL

The remaining material parameters for the NBG perovskite, C_{60}, and BCP were taken from Section C.2. For all structures, the top subcell contains a 20 nm C_{60} electron transport layer (without BCP), while the bottom subcell includes both C_{60} (20 nm) and BCP (8 nm). Each tandem uses the same ITO

Table C.6: Material parameters of the wide-bandgap (WBG) perovskite absorber used in all PVK/PVK tandem configurations. Values are based on [44] and applied consistently across all tandem types to isolate HTL-dependent effects.

Parameter	Symbol / Unit	Value
Bandgap	E_g [eV]	1.68
Electron affinity	χ [eV]	4.0
Relative permittivity	ε_r	6.5
Effective DOS (CB)	N_C [cm^{-3}]	1.0×10^{20}
Effective DOS (VB)	N_V [cm^{-3}]	1.0×10^{19}
Electron mobility	μ_n [cm^{2}V^{-1}s^{-1}]	35
Hole mobility	μ_p [cm^{2}V^{-1}s^{-1}]	35
Thickness	t [nm]	280

TRJ thickness of 5 nm to ensure balanced recombination. Front and back contacts are FTO and Al, respectively.

Table C.7: Layer stacks and thicknesses used in the three flexible PVK/PVK tandem configurations. Electrical parameters of the HTLs and transport layers are given in Section C.2. WBG and NBG perovskite absorber parameters follow [44].

Layer	Material	Inorganic Tandem	Organic Tandem	nc-SiO$_x$(p) Tandem
Front contact	FTO	5 nm	5 nm	5 nm
HTL (top)	NiO$_x$ / PTAA / nc-SiO$_x$(p)	20 nm	10 nm	13 nm (10 + 3)
WBG absorber	Perovskite (WBG, E_g = 1.68 eV)	280 nm	280 nm	280 nm
ETL (top)	C_{60}	20 nm	20 nm	20 nm
Interlayer (TRJ)	ITO	5 nm	5 nm	5 nm
HTL (bottom)	NiO$_x$ / PEDOT / nc-SiO$_x$(p)	20 nm	20 nm	20 nm
NBG absorber	Perovskite (NBG, E_g = 1.23 eV)	900 nm	900 nm	900 nm
ETL (bottom)	C_{60}	20 nm	20 nm	20 nm
Buffer	BCP	8 nm	8 nm	8 nm
Back contact	Al	–	–	–

D

Optical Absorptance Profiles of Simulated Solar Cells

This appendix presents the layer-resolved optical absorptance spectra for the main solar cell configurations simulated in GENPRO4 and used to generate the optical generation profiles for Sentaurus `sdevice`. Each plot shows the wavelength-dependent absorptance contribution of individual layers and the corresponding integrated current density under AM1.5G illumination. These results confirm proper optical power balance and highlight the spectral regions where each subcell contributes to overall photocurrent generation.

D.1. Single-junction nc-Si:H Cell

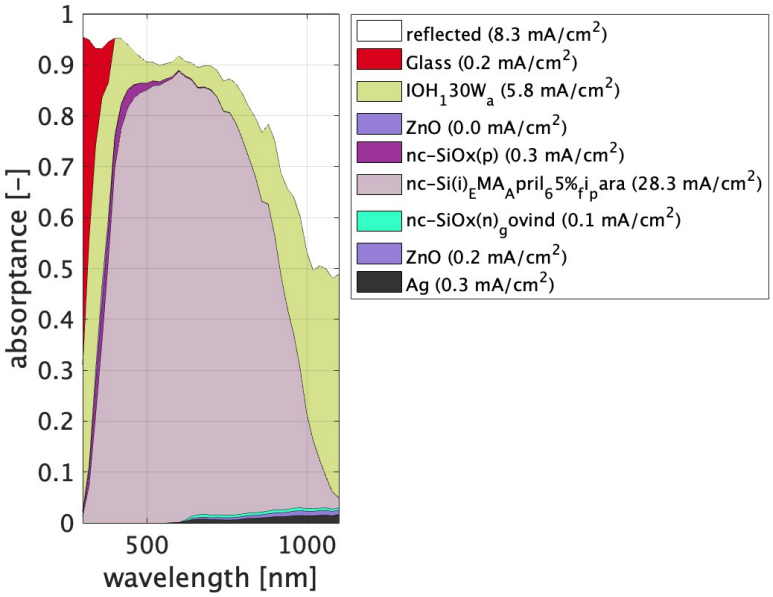

Figure D.1: Layer-resolved absorptance spectrum of the single-junction nc-Si:H solar cell simulated in GENPRO4. The spectrum shows dominant absorption in the near-infrared region corresponding to the smaller bandgap of nc-Si:H.

D.2. a-Si:H/nc-Si:H Tandem

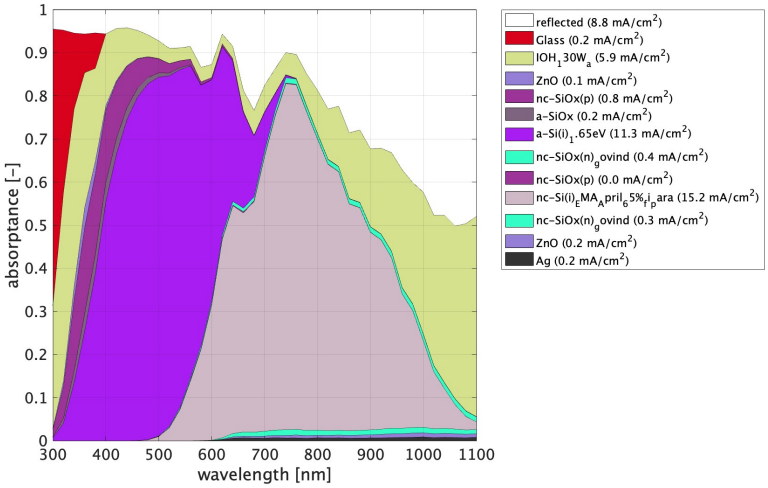

Figure D.2: Layer-resolved absorptance spectrum of the micromorph (a-Si:H/nc-Si:H) tandem solar cell. The a-Si:H top subcell absorbs mainly below 700 nm, while the nc-Si:H bottom subcell captures the near-infrared part of the spectrum, leading to effective current matching between the subcells.

D.3. SJ PVK with NiO_x and PTAA HTL

D.4. Hybrid a-Si:H/PVK Tandem

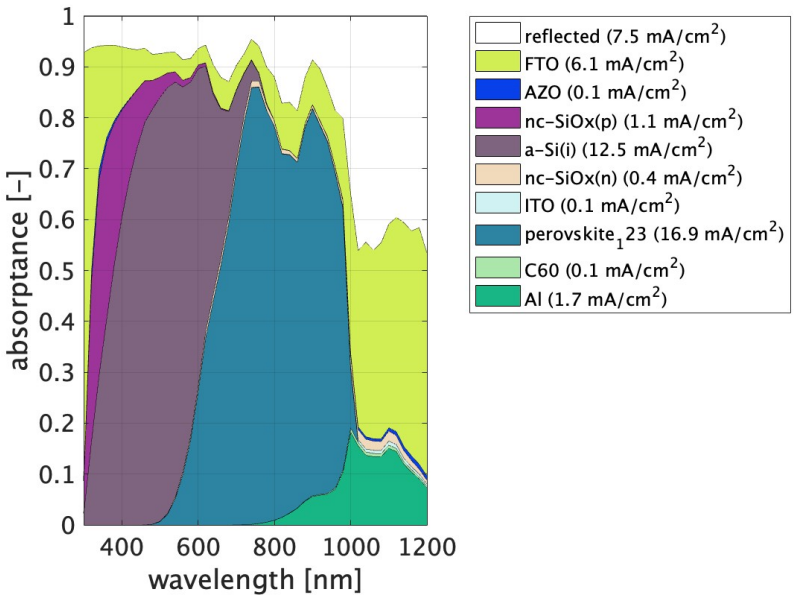

Figure D.4: Optical absorptance of the hybrid a-Si:H/PVK tandem. The top a-Si:H subcell absorbs predominantly in the visible range, while the narrow-bandgap perovskite bottom subcell contributes primarily in the near-infrared. The use of an ITO tunnel recombination junction ensures efficient optical coupling between the subcells.

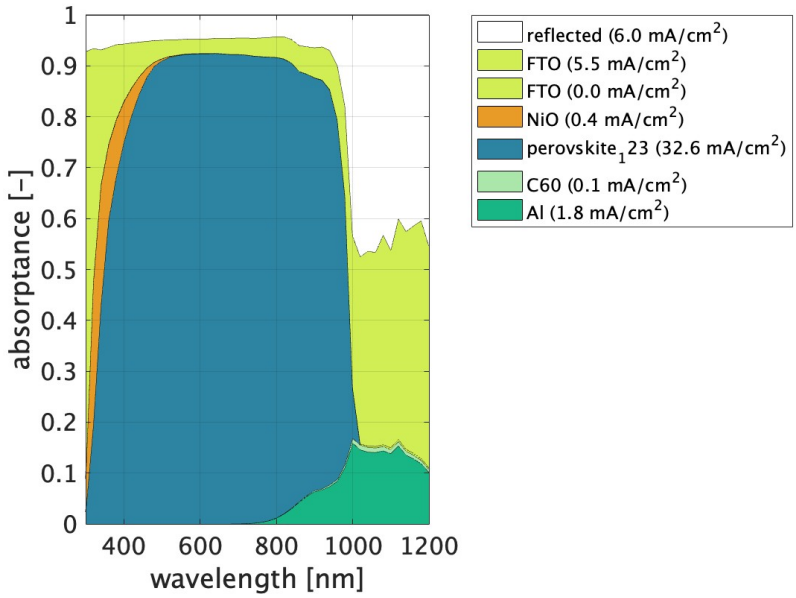

(a) Absorption profile of the single-junction perovskite cell using a NiO_x HTL. The strong absorption in the perovskite layer and minimal parasitic losses in NiO_x indicate efficient photon utilization.

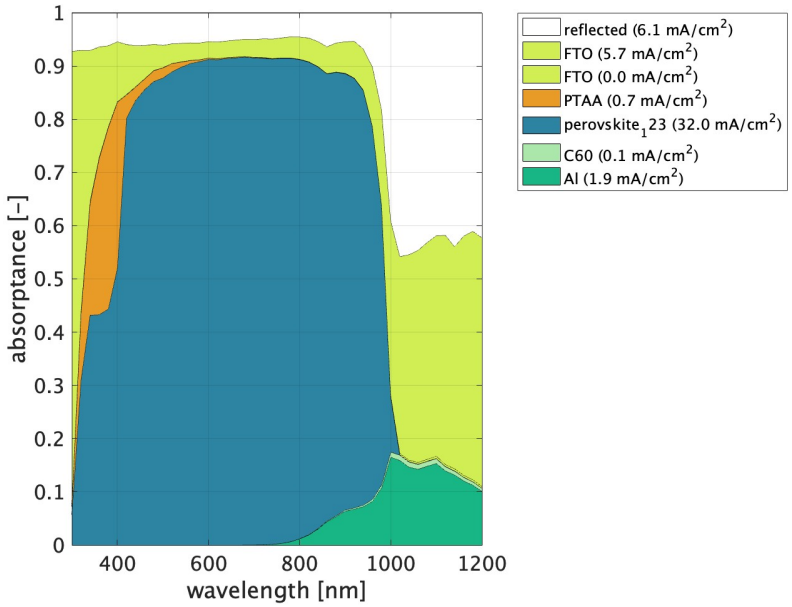

(b) Absorption profile of the single-junction perovskite cell using a PTAA HTL. Similar spectral response is observed, with slightly higher parasitic absorption at short wavelengths compared to NiO_x.

Figure D.3: Simulated absorption profiles of the single-junction perovskite solar cell using NiO_x and PTAA as hole transport layers. Both HTLs enable efficient light absorption within the perovskite absorber, with NiO_x showing marginally reduced front-side optical losses.

D.5. All-perovskite (PVK/PVK) Tandem

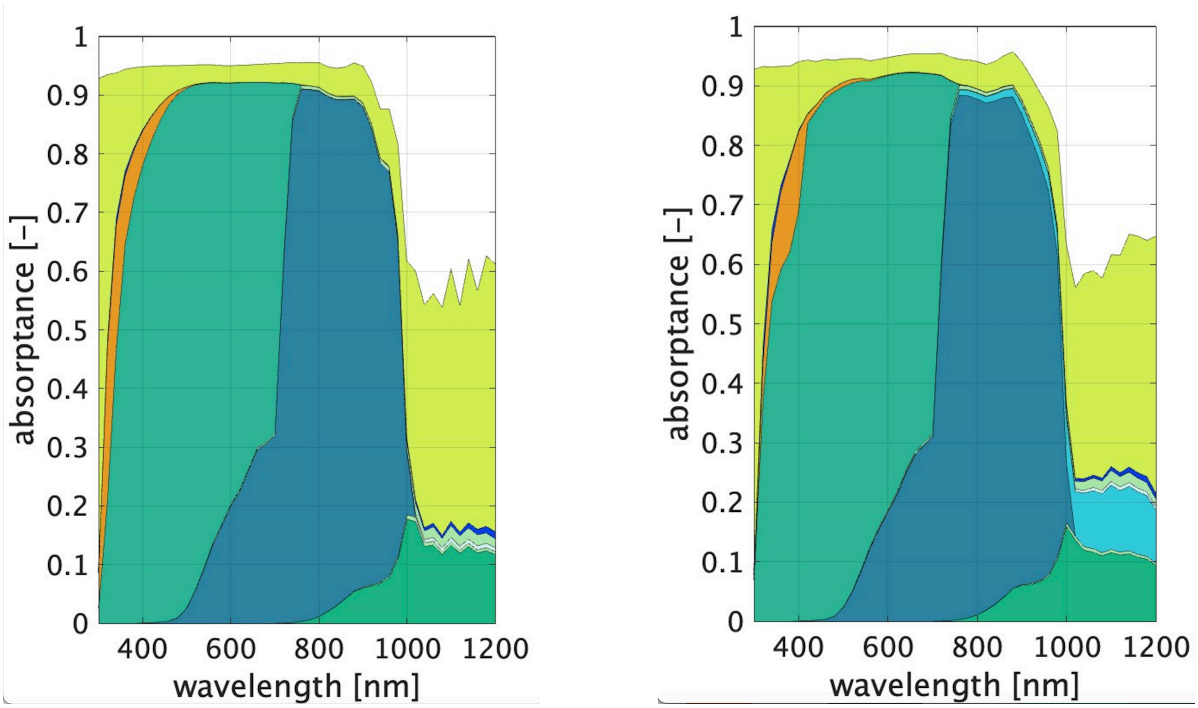

(a) NiO_x/NiO_x.

(b) PTAA/PEDOT:PSS.

Figure D.5: Layer-resolved absorptance for inorganic and organic HTL configurations. The organic tandem shows a $\sim$350 nm front-stack feature and enhanced 650–900 nm parasitics in PEDOT:PSS. The nc-SiO_x(p) profile (not shown) closely follows NiO_x/NiO_x, confirming low optical loss.

D.6. Charge Conservation in Optical Generation at 320 nm for a-Si:H Solar Cell

During the optical simulation stage, an isolated unphysical spike appeared in the optical generation profile of the a-Si:H solar cell at 320 nm. This artifact was localized in the p-layer and was not observed at other wavelengths. To remove this numerical anomaly while maintaining charge conservation, a two-step correction method was applied to the affected generation profile.

The first step was spike filtering. The profile of each layer was scanned, and any data point exceeding 110% of the average of its two adjacent values was replaced with that local average. This filtering was only performed within individual layers, as genuine spikes can occur at material interfaces.

The second step was to restore the removed area from step one to conserve the total absorbed charge. The lost area, ΔA, was redistributed uniformly across the affected layer, leading to a corrected generation rate given by:

$$G_{\text{corrected}}(z) = G_{\text{filtered}}(z) + \frac{\Delta A}{L}, \quad z \in [z_1, z_2] \tag{D.1}$$

where

$$\Delta A = \int_{z_1}^{z_2} [G_{\text{raw}}(z) - G_{\text{filtered}}(z)]\, dz$$

is the difference in integrated area and $L = z_2 - z_1$ is the width of the correction region.

Figure D.6 shows the effect of this correction. The raw generation profile (black curve) exhibits a spurious spike near the front of the absorber. After applying the filtering and area-restoration steps, the corrected profile (red curve) maintains physical smoothness and conserves the total absorbed charge.

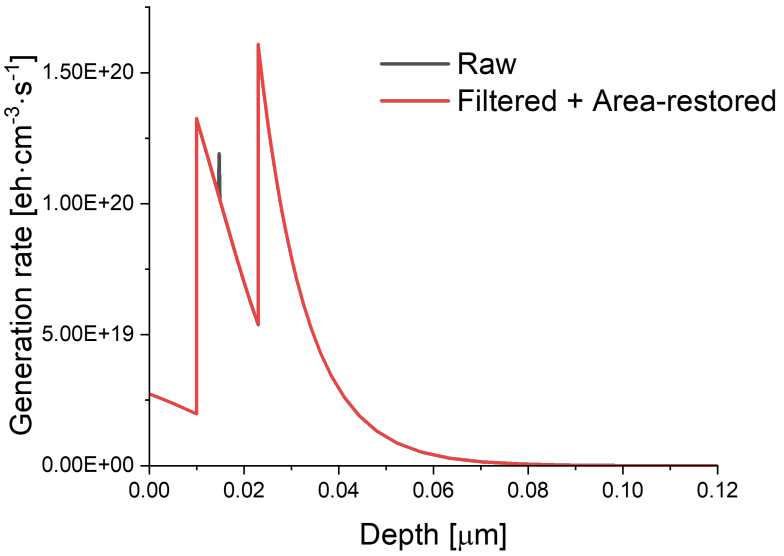

Figure D.6: Optical generation profile at 320 nm for the a-Si:H solar cell. A spurious spike in the front absorber region (black curve) is corrected through local filtering and area restoration (red curve), preserving the total integrated generation rate.